Generation and Characterisation of Non-Classical Surface Plasmons

Huck, Alexander; Lodahl, Peter; Andersen, Ulrik Lund

Publication date:
2010

Document Version
Publisher's PDF, also known as Version of record

Generation and Characterization of Non-Classical Surface-Plasmon-Polaritons

Alexander Huck

A thesis submitted for the degree
Doctor of Philosophy in Physics
Technical University of Denmark

Supervisor
Associate Professor Ulrik L. Andersen
Department of Physics
The Technical University of Denmark

January 2010

Abstract

This work focuses on the experimental characterization of electromagnetic waves propagating along the interface between an insulator and a conductive medium. Such waves are commonly known as surface plasmon polaritons (SPPs) and might, for instance, pave the way towards miniaturized integrated optical devices and enable strong non-linear optical processes at very low light levels.

Thin metal stripes support almost Gaussian shaped SPP modes propagating over distances of several millimeters. These modes were efficiently excited using optical beams propagating in free space and verified by the polarization dependence of the excitation. Simultaneous measurements of the reflection and transmission, while tuning the temperature of the sample, demonstrate standing waves on SPP modes. Optical pulses of μs durations were used to analyze the non-linear absorption coefficient of SPP modes. A strong power dependency of the absorption was found and the characteristic time constant of the underlying process was determined to be of the order of ms, which is characteristic for thermal processes.

An optical parametric amplifier (OPA) was build as a resource of quadrature squeezed vacuum states. These states were characterized by means of homodyne measurement and the density matrix

was reconstructed using a maximum likelihood algorithm. A maximum squeezing level of -1.9 ± 0.1 dB below the shot noise level was measured. Non-classical SPP modes on a thin gold stripe were generated by exciting them with quadrature squeezed vacuum states. After propagation and re-emission, the remaining quantum states were characterized using the same experimental techniques as before. It could be demonstrated that -0.7 ± 0.1 dB of squeezing survived the plasmonic excitation, propagation, and re-emission. In contrast to previous work, the experiment presented here characterizes SPP modes in an infinite dimensional Hilbert space including the coherence between photon number states. The impact of the SPP mode on the quadrature squeezed vacuum state was successfully simulated by applying a standard beam splitter model.
Recent theoretical advances motivate the excitation of quantized SPPs by means of placing single photon emitters in their near vicinity. A prominent representative of such emitters is the nitrogen-vacancy (NV) center in diamond, which emits near infrared single photons at room temperature. Single NV-centers embedded in diamond nanocrystals were placed near thin silver wires. By monitoring the photon re-emission from the wire end facets using single-photon resolving confocal microscopy, the NV-center coupling to propagating plasmonic modes could be verified. Due to the strong dispersion of the propagating SPP modes and the finite wire length the measured SPP spectrum was strongly modulated. In addition to this, second-order correlation function measurements reveal the excitation of quantized SPPs.

Dansk Resumé

Denne afhandling beskriver eksperimentelle undersøgelser af elektromagnetiske bølger, som bevæger sig på overgangen mellem et isolerende og et ledende materiale. Disse bølger bliver normalt kaldt "surface plasmon polaritons" (SPP), og deres fundamentale egenskaber kan føre til dannelsen af ekstremt høje ikke-lineariteter samt konstruktionen af nano-skopiske integrerede optiske kredsløb.

Tynde striber af metal understøtter SPP modes, der har den specielle egenskab at de kan udbredes flere millimeter langs metallets overflade. Gennem målinger af transmission og refleksion af sådanne modes for forskellige metaltemperaturer, er det blevet påvist at stående SPP bølger eksiteres. Ydermere er den ikke-linære absorptionskoefficient for SPP mode'ene blev undersøgt gennem studier af pulsudbredelser i metallet. Det blev påvist at absorbtionen var stærkt afhængig af pulseffekten og den karakteristiske tidskonstant blev fundet til at være af størrelsesordenen millisekunder, hvilket er typisk for termiske processer.

Hovedemnet i denne afhandling er at undersøge udbredelsen af kvantelys i SPP modes. To forskellige ikke-klassisk tilstande af lyset er blevet undersøgt; såkaldt squeezed lys og en en-foton tilstand.

En optisk parametrisk forstærker blev brugt som kilde til generering

af squeezed lys. Denne tilstand af lyset blev fuldt ud karakteriseret ved brug af homodyn detektion både før og efter udbredelse i metallet. Gennem disse målinger er det blevet vist at de ikke-klassiske egenskaber overlever udbredelsen i metallet.
Udover den squeezed tilstand er enkelt foton-tilstande blevet genereret. Kilden til udsendelsen af sådant lys er urenheder i meget små diamant krystaller. Urenhederne giver anledning til en diskret energistruktur, som udsender lys i bølgepakker bestående af en enkelt foton. Disse enkelt foton kilder blev placeret tæt på tynde sølvtråde, som understøtter SPP modes. Gennem vekselvirkninger mellem tråden og diamanten fokuseres fotonen ned i den udbredende SPP mode. Ved brug af konfokal mikroskopi er det blevet påvist at både den oprindelige lysbølgepakke samt den eksiteret SPP bølgepakke bestod af en enkelt foton hvilket igen demonstrerer overlevelsen af en ikke-klassisk lystilstand på overfladen af et metal.

Contents

List of Figures

List of Tables

1 Introduction

Since their first discovery by the pioneering work of Ritchie in the 1950's [1], surface plasmons are widely recognized in the field of surface science. In contrast to all-dielectric waveguides, where the wavelength sets a lower bound to the size to which light can be confined, adequately shaped metallic structures can confine light to arbitrarily small length scales. This phenomenon bears great potential in, for instance, sub-wavelength guiding [2, 3, 4, 5], efficient single molecule sensing [6, 7], enhanced non-linear effects [8, 9, 10], and the miniaturization of photonic circuits [11, 12]. In addition to this, strong interaction of quantum emitters is enabled by the small mode size of nano-plasmonic waveguides, which may have useful applications in quantum information. As such, miniaturized plasmonic structures might be a key building block for a single photon source on demand [13, 14, 15] and enable strong non-linear interactions at the level of single photons [16].

Quantum communication and information are an undeniably important area in modern physics, highlighted by its rapid expansion in recent years. Much interest has recently been devoted to the emergent field of quantum plasmonics due to its unique capabilities in the way electromagnetic radiation can be localized and manipulated at the nanoscale. In particular, integrated quantum technologies based on surface plasmons hold great promises for quantum information

processing, since it allows for scalability, miniaturization, and coherent coupling to single emitters [13, 14, 17, 15, 18]. To enable these quantum information processing technologies with high fidelity, it is of paramount importance, that the nonclassicality of the plasmonic modes is preserved in propagation. The first experiment verifying the preservation of entanglement in plasmonic nanostructures was carried out by Alterwischer et al. [19]. They demonstrated the survival of polarization entanglement after plasmonic propagation through subwavelength holes in a metal film. The preservation of energy time entanglement in a perforated metal film as well as in a thin conducting waveguide was later demonstrated by Fasel et al. [20]. These experiments have witnessed the preservation of probabilistically prepared entanglement (thus neglecting the coherence between photon number states) described in a two dimensional Hilbert space.

This thesis is divided into two parts. Part I is devoted to classical properties of SPPs and starts by a general introduction to electromagnetism of metals. After that, the SPP modes of metallic stripes and their dispersive properties are described. This description is followed by an introduction of SPP modes on nano-sized metallic cylinders with a focus on the lowest order mode, the so-called Sommerfeld mode [21]. In chapter 3 the fabrication technique of metallic stripe waveguides is presented. These stripes with width in the μm range are suitable for surface-plasmon propagation of several mm. Cylindrically shaped nano-wires were made by a polyol process. Following the description of that, the excitation of long range SPP modes on metal stripes is verified by the polarization dependence. Measurements of both the transmission and the reflection of surface plasmon modes on metal stripes are presented and modeled as well. The nonlinear absorption induced by surface-plasmon modes of laser pulses with μs duration is studied in chapter 4. By analyzing these modes in an asymmetric Sagnac interferometer, the introduced nonlinear phase shift is measured as well.

The focus of the second part of this thesis lies on the excitation of surface plasmons with quantized light fields. For these studies, an optical parametric amplifier was build used for the generation of quadrature squeezed light. By completely characterizing surface plasmon modes excited with quadrature squeezed states of light, the impact of the plasmonic propagation could be modeled with a stan-

dard beam splitter. The experimental results are explained by theoretical arguments [22]. Chapter 6 describes the coupling of a single photon emitter to the SPP mode of a cylindrically shaped nano-wire. A single nitrogen vacancy (NV) center in a diamond nano-crystal is employed as a single photon source. First, the general properties of NV-centers are introduced. This introduction is followed by an experimental study of NV-centers in a confocal microscope. Measurements of the second order correlation function witness the emission of single photons. By spin-coating nano-diamonds on top of the nano-wires, coupled NV-center plasmon systems were found by fluorescence spectroscopy. Again, a measurement of the second order correlation function proves the excitation of a single quanta surface plasmon. This chapter is closed with an outlook on future experimental activities. These activities comprise an extension of the experimental set-up as well as new structures.

Other projects

During the course of this PhD work other projects have been carried out which are not related to the field of plasmonics and thus not described in this thesis. For reference, these projects will be summarized in the following.

Quantum correlations induced by multiple scattering of nonclassical light

In this work, spatial quantum correlations of photons that are induced by multiple scattering of squeezed light have been demonstrated experimentally. The quantum correlation relates photons propagating along two different light paths through the random medium and is infinite in range. Both positive and negative spatial quantum correlations were observed by varying the quantum state of light incident to the multiple scattering medium, and the strength of the correlations is controlled by the number of photons. The experimental results of this work are in excellent agreement with theoretical proposals and verified by implementing the full quantum model of multiple scatter-

ing. The results of this work are published in

- *Observation of Spatial Quantum Correlations Induced by Multiple Scattering of Nonclassical Light.* S. Smolka, A. Huck, U. L. Andersen, A. Lagendijk, and P. Lodahl, Phys. Rev. Lett. **102**, 193901 (2009).
- *Spatial Quantum Correlations Induced by Multiple Scattering of Squeezed Light.* S. Smolka, A. Huck, U. L. Andersen, A. Lagendijk, and P. Lodahl, in preparation.

Demonstration of a quantum non-demolition sum gate

The sum gate is the canonical two-mode gate for universal quantum computation based on continuous quantum variables. It represents the natural analogue to a qubit controlled-NOT gate. In addition, the continuous variable gate describes a quantum non-demolition (QND) interaction between the quadrature components of two light modes. A QND sum gate was experimentally demonstrated by employing the scheme of R. Filip et al. [23]. This scheme is solely based on off-line squeezed states, homodyne measurements, and feedforward. The results are verified by simultaneously satisfying the criteria for QND measurements in both conjugate quadratures.

- *Demonstration of a Quantum Nondemolition Sum Gate.* Junichi Yoshikawa, Yoshichika Miwa, Alexander Huck, Ulrik L. Andersen, Peter van Loock, and Akira Furusawa, Phys. Rev. Lett. **102**, 250501 (2008).

Correlation measurement of squeezed light

A correlation measurement technique for the characterization of squeezed light is nearly free of electronic noise. With two different sources of squeezed light, it has been shown that the sign of the covariance coefficient, revealed from the time-resolved correlation data, is witnessing the presence of squeezing in the system. Furthermore, the degree of

squeezing is determined using the correlation method and compared to the standard homodyne measurement scheme. It was shown that the role of electronic detector noise is minimized using the correlation approach as opposed to homodyning, where it often becomes a crucial issue. The results are published in the following articles.

- *Electronic noise-free measurements of squeezed light.* Leonid A. Krivitsky, Ulrik L. Andersen, Ruifang Dong, Alexander Huck, Christoffer Wittmann, and Gerd Leuchs, Optics Letters **33**, 2395 (2008).
- *Correlation measurement of squeezed light.* Leonid A. Krivitsky, Ulrik L. Andersen, Ruifang Dong, Alexander Huck, Christoffer Wittmann, and Gerd Leuchs, Phys. Rev. A **79**, 033828 (2009).

Continuous-variable quantum erasure correcting code

A quantum erasure-correcting code protocol for continuous variables, which protects multi-photonic quantum information from complete erasure was implemented for the first time. The code is surprisingly simple and can therefore be realized with an optical setup of reasonable complexity [24]. It is capable of simultaneously protecting two signal states against the erasure (or loss) of one of the four information-carrying modes. The viability of this protocol was demonstrated with convincing results that fit the theoretical predictions. This work has been submitted.

- *Quantum optical coherence can survive photon losses: a continuous-variable quantum erasure correcting code* M. Lassen, M. Sabuncu, A. Huck, G. Leuchs, J. Niset, N.J. Cerf, and U.L. Andersen, submitted for publication.

Part I

Classical Properties of Surface Plasmon Polaritons

2

Modeling Surface Plasmon Polaritons

2.1 Electromagnetism of Metals

In general, the interaction of metals with electromagnetic fields can be understood in a classical framework by Maxwell's equations. The high density of free electrons in metals leads to a minute spacing of the electron energy levels compared to the thermal excitation $k_B T$ at room temperature. Due to the fact that the optical properties of metals depend strongly on the frequency of the electromagnetic field a rich variety of optical phenomena arises. Metals are highly reflective up to the visible part of the electromagnetic spectrum. Thus, in a broad frequency range electromagnetic waves are not allowed to propagate through them. Towards the visible spectrum, the field penetration into the metal increases, leading to increased dissipation of the field. At ultraviolet frequencies, metals acquire dielectric properties and allow the propagation of electromagnetic fields, albeit with varying degrees of attenuation depending on the details of the electronic band structure. For noble metals such as gold or silver, transitions between electronic bands lead to strong absorption in this regime. The dispersive properties of metals are described via a complex dielectric function $\epsilon(\omega)$, where ω is the angular frequency of the electromagnetic field, which is the basis for all classical phenomena

observed on metal structures.
Maxwell's equations of macroscopic electromagnetism are given by

$$\nabla \cdot \mathbf{D} = \rho_{\text{ext}}, \tag{2.1}$$
$$\nabla \cdot \mathbf{B} = 0, \tag{2.2}$$
$$\nabla \times \mathbf{E} = -\frac{\partial \mathbf{B}}{\partial t}, \quad \text{and} \tag{2.3}$$
$$\nabla \times \mathbf{H} = \mathbf{J}_{\text{ext}} + \frac{\partial \mathbf{D}}{\partial t}, \tag{2.4}$$

which link the dielectric displacement $\mathbf{D}$, the electric field $\mathbf{E}$, the magnetic field $\mathbf{H}$, and the magnetic induction $\mathbf{B}$ to the external charge and current densities ρ_{ext} and $\mathbf{J}_{\text{ext}}$. Here, charges and current densities are divided into an external set (ρ_{ext}, $\mathbf{J}_{\text{ext}}$) driving the system and an internal set (ρ, $\mathbf{J}$) responding to the stimuli. The total charge and current densities are given by $\rho_{\text{tot}} = \rho_{\text{ext}} + \rho$ and $\mathbf{J}_{\text{tot}} = \mathbf{J}_{\text{ext}} + \mathbf{J}$, respectively.
A link to the electric polarization $\mathbf{P}$ and magnetization $\mathbf{M}$ of the medium is given by

$$\mathbf{D} = \epsilon_0 \mathbf{E} + \mathbf{P}, \tag{2.5}$$
$$\mathbf{H} = \frac{1}{\mu_0}\mathbf{B} - \mathbf{M}. \tag{2.6}$$

ϵ_0 and μ_0 are referred to as the vacuum permittivity and the vacuum permeability, respectively, and are linked to the vacuum speed of light c via $c^2 = 1/\epsilon_0\mu_0$. If the medium is linear, isotropic, and nonmagnetic one can define the constitutive relations

$$\mathbf{D} = \epsilon_0 \epsilon \mathbf{E}, \tag{2.7}$$
$$\mathbf{B} = \mu_0 \mu \mathbf{H}, \tag{2.8}$$

where ϵ is called the dielectric constant and $\mu = 1$ is the relative permittivity of the non-magnetic medium. The internal current density $\mathbf{J}$ and the electric field $\mathbf{E}$ are linked via

$$\mathbf{J} = \sigma \mathbf{E}, \tag{2.9}$$

where σ is the conductivity of the material. It can be shown, that the dielectric function $\epsilon(\mathbf{k}, \omega)$ depends on the conductivity σ via

$$\epsilon(\mathbf{k}, \omega) = 1 + \frac{i\sigma(\mathbf{k}, \omega)}{\epsilon_0 \omega}, \tag{2.10}$$

where $\mathbf{k}$ is the wave vector of the electric field.
In case the photon energy $\hbar\omega$ is low, the dielectric function $\epsilon(\omega)$ can be explained with the model of a free electron gas. This electron gas, also called plasma sea, consists of free electrons of number density n which move against a fixed background of positive ion cores. The equation of motion for an electron of the plasma sea, that is subjected to an external electric field $\mathbf{E}$, is given by

$$m\ddot{\mathbf{x}} + m\gamma\dot{\mathbf{x}} = -e\mathbf{E}. \tag{2.11}$$

Here, $\mathbf{x}$ is the amplitude of the electron oscillation, m is the electron mass, γ is the material characteristic electron collision frequency, and e is the elementary charge. Assuming a harmonic dependence of the driving field $\mathbf{E}(t) = \mathbf{E}_0 e^{-i\omega t}$ and using the relation $\mathbf{P} = -ne\mathbf{x}$, one can find that

$$\mathbf{P} = -\frac{ne^2}{m\left(\omega^2 + i\gamma\omega\right)}\mathbf{E}. \tag{2.12}$$

Inserting this result into Eqn. (2.5) and using Eqn. (2.7), the dielectric function of the free electron gas can be identified as

$$\epsilon(\omega) = 1 - \frac{\omega_p^2}{\omega^2 + i\gamma\omega}, \tag{2.13}$$

where the plasma frequency $\omega_\mathrm{p}^2 = \frac{ne^2}{\epsilon_0 m}$ has been defined. This is the result describing the dielectric function of the free electron gas, which is generally referred to as the Drude model. The measured dielectric function of gold and silver (taken from Ref. [25]) are shown in Fig. 2.1. These metals were used throughout this thesis. It can be seen, that the Drude model (shown as red line in Fig. 2.1) describes well the dielectric behavior over a wide range of photon energies. The parameters for ω_p and γ, which were used for the model, are summarized in Table 2.1. The breakdown of the Drude model occurs in the imaginary part of ϵ due to interband transitions of the electrons taking place in the metal. The break down energy of 2 eV for gold and 3.8 eV for silver correspond to vacuum wavelength of 620 nm and 326 nm, respectively. This is important to note since for illumination of nanometer sized noble metal particles with light at shorter wavelength than the before mentioned electron-hole pairs are generated, which might lose some of their energy via various different scattering mechanism and recombine radiatively at longer wavelength [27, 28].

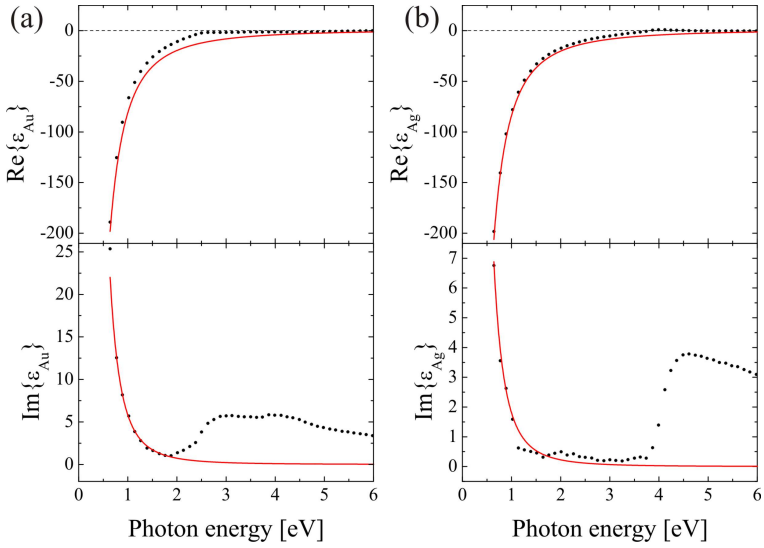

Figure 2.1: Real- and imaginary part of the dielectric function ϵ of bulk gold (a) and silver (b) as a function of photon energy: The black dots are experimental values taken from Ref. [25] and the red lines are calculated via Eqn. (2.13) with parameters as given in Table 2.1.

2.2 Metal Stripe Insulator Interfaces

On a metal-insulator interface a bound solution of Maxwell's equations (2.1)-(2.4) can be found for a mode propagating along the interface. In general, this mode is referred to as surface plasmon polariton (SPP) and can be understood as an electromagnetic wave coupled to the electron density oscillations in the metal and propagating along the interface between the insulator and the metal. SPP modes arise because of free electrons in the metal, expressed via a negative real part of the metals dielectric constant: $Re\{\epsilon_{\mathrm{met}}\} < 0$. A non-zero negative imaginary part of ϵ_{met} on the other side only introduces propagation losses of the SPP mode. More of practical importance, especially with a focus on this thesis, are bound SPP modes on thin

	ω_p $[s^{-1}]$	γ $[s^{-1}]$
Au	$13.8 \cdot 10^{15}$	$107.5 \cdot 10^{12}$
Ag	$14.0 \cdot 10^{15}$	$32.3 \cdot 10^{12}$

Table 2.1: Plasma frequency ω_P and characteristic electron collision frequency γ for gold and silver taken from Refs. [25, 26].

metal films corresponding to an insulator-metal-insulator interface. In case the metal film extends to infinity in the x-direction, as illustrated in Fig. 2.2, an analytic SPP solution to Maxwell's equations exists, which was first provided by J.J. Burke et al. [29]. In this case,

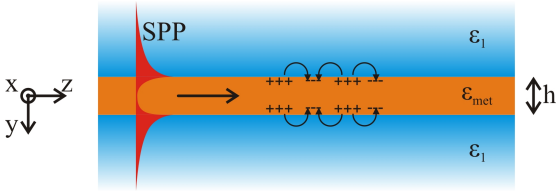

Figure 2.2: Multilayer for the propagation of confined SPP-waves.

the derivation of the fields **E** and **H** is rather simple and will be briefly summarized. Maxwell's equations (2.1)-(2.4) have to be applied to the geometry shown in Fig. 2.2. In absence of external charge and current densities and under the assumption of a harmonic time dependence of the electric field $\mathbf{E}(\mathbf{r}, t) = \mathbf{E}(\mathbf{r})e^{-i\omega t}$, the wave equation for the electric field can be written as

$$\nabla^2 \mathbf{E} + k_0^2 \epsilon \mathbf{E} = 0, \tag{2.14}$$

where $k_0 = \omega/c$ is the wave vector in vacuum. With respect to the metal surface the only solution to the wave equation (2.14) is a transverse magnetic (TM) mode for which the electric field is polarized in the y-z plane; a transverse electric (TE) mode is non-existing. After solving for the TM-mode boundary conditions, a dispersion equation

for the propagating SPP modes can be derived, which is given by

$$\begin{aligned} \tanh\left(k_{\perp,2}h\right)\left(\epsilon_1\epsilon_3 k_{\perp,2}^2 + \epsilon_{met}^2 k_{\perp,1}k_{\perp,3}\right) &+ \\ \left[k_{\perp,2}\left(\epsilon_1 k_{\perp,3} + \epsilon_3 k_{\perp,1}\right)\epsilon_{met}\right] &= 0. \end{aligned} \tag{2.15}$$

The coefficients $k_{\perp,i}$, $i = \{1, met, 3\}$, are obtained from the wave equation as $k_{\perp,i}^2 = k_\parallel^2 - \epsilon_i k_0^2$ with $k_\parallel$ being the complex SPP modes propagation constant and h is the height of the metal film. $k_{\perp,1}$ and $k_{\perp,3}$ are the coefficients determining the exponential decay of the fields in region 1 and 3, respectively. The dispersion Eqn. (2.15) has two solutions, a symmetric and an antisymmetric bound mode, identified as such on their respective transversal field patterns [29]. Depending on their propagation losses, the symmetric and antisymmetric modes are generally referred to as long-range (LR) and short-range (SR) SPPs, respectively. For a gold film height of 14 nm, calculating $\epsilon_{\mathrm{Au}}(\omega)$ using the Drude model (2.13) with the parameters as specified in Table 2.1, and a symmetric surrounding dielectric medium benzocyclobutene (BCB) with a constant refractive index $n_{\mathrm{BCB}} = 1.539$, the LR-SPP and SR-SPP solutions of Eqn. (2.15) are plotted in Fig. 2.3. For low photon energies, corresponding to

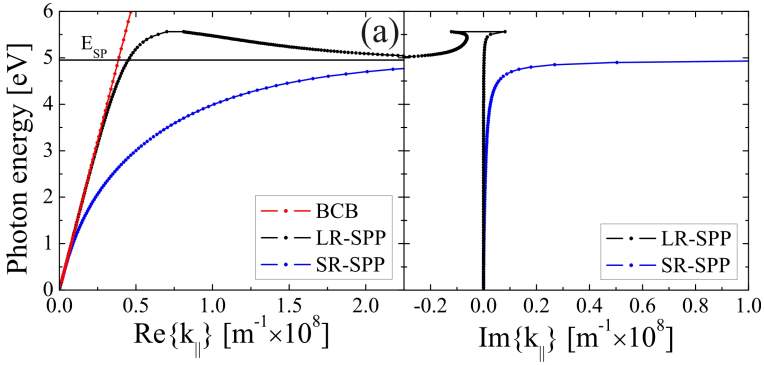

Figure 2.3: Calculated dispersion of a 14 nm thin gold film embedded in BCB: photon energy versus the real- (a) and the imaginary part (b) of the propagation constant $k_\parallel$.

the infra-red and near-infra-red spectral region, the propagation constants of the LR-SPP and SR-SPP modes are close to the light line

of the insulator BCB. At higher photon energies, corresponding to the UV-regime, the wave-vectors increase and asymptotically go to infinity when $\hbar\omega$ approaches the surface plasmon energy E_{SP}, which is defined as $E_{\mathrm{SP}} = \hbar\omega_P/\sqrt{1+\epsilon_{\mathrm{BCB}}}$. Since for photon energies $\approx E_{\mathrm{SP}}$ the wave vectors go to infinity, the group velocity $v_{\mathrm{gr}} \to 0$ and the SPP modes acquire an electrostatic character. It should be emphasized that the graphs in Fig. 2.3 were calculated under the assumption that $\epsilon_{\mathrm{Au}}(\omega)$ can be described by the Drude model given by Eqn. (2.13) with parameters specified in Table 2.1, which in case of gold breaks down for photon energies larger than $2eV$, as already mentioned.
In case of a metal stripe with a finite width an analytic solution of Maxwell's equation does not exist. To find the mode profile and their corresponding propagation constant $k_{\parallel} = n_{\mathrm{eff}}k_0$, the finite element method software package Comsol Multiphysics has been used. The wave equation was solved in the transverse x-y plane for the sample geometry shown in Fig. 2.4 (a) with perfectly matched layer boundaries located many μm away from the metal structure. As an example of the simulation outcome, a normalized power density plot of a zero order TM_{00} LR-SPP mode on a gold stripe embedded in BCB with a height of 14 nm and a width of 1 μm is plotted in Fig. 2.4 (b). The

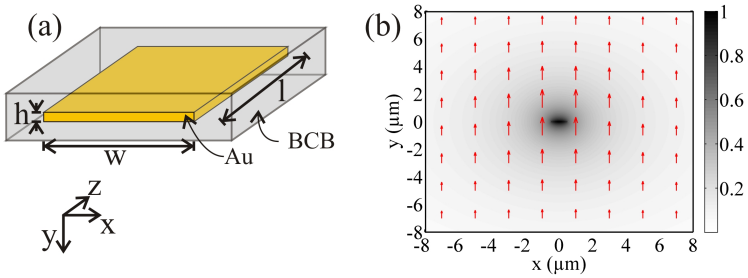

Figure 2.4: (a) Sketch of the sample for propagating LR-SPP modes. (b) Normalized power density plot of a LR-SPP mode on a gold stripe embedded in BCB with a height and with of 14 nm and 1 μm, respectively. The red arrows show the direction of the electric field E_{x} and E_{y} in the transverse plane of the stripe.

red arrows indicate the direction of the electric field E_{x} and E_{y} in

the transverse plane of the stripe and displays that the mode is TM polarized with respect to the metal stripe surface in the x-z plane. Fig. 2.5 shows the dependence of both the real (a) and imaginary part (b) of n_{eff} on the stripe width. Additionally plotted are the n_{eff} of higher order TM_{m0} modes, where m is an integer denoting the number of nodes in the electric field along the x-direction. It can be seen that for increasing stripe width n_{eff} approaches asymptotically the value derived via Eqn. (2.15) for all modes and therefore proves the validity of the model.

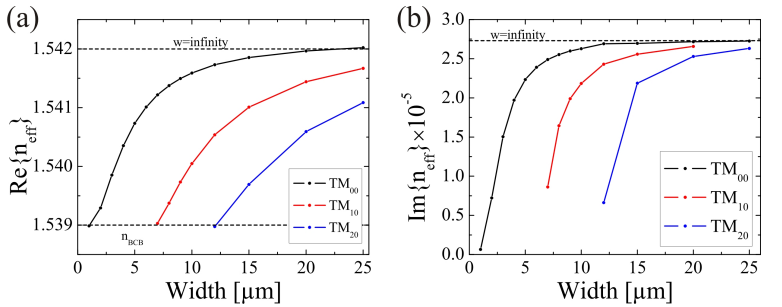

Figure 2.5: (a) Real- and (b) imaginary part of the LR-SPP effective refractive index n_{eff} of gold stripes with a height of $14nm$ embedded in BCB versus various gold stripe width.

Of experimental interest is the LR-SPP mode field diameter (MFD) in the x- and y-direction of the transverse plane. The MFD is defined via the $1/e^2$ power decay from its maximum value and obtained by numerically evaluating power line plots through the metal stripe center. Some results are shown in Fig. 2.6 (a). In the y-direction, the mode profile is exponential, while in the x-direction a nearly Gaussian mode profile is obtained. For various stripe width and a constant stripe height of 14nm, the horizontal (x) and vertical (y) MFD of the LR-SPP modes are plotted in Fig. 2.6 (b). As can be seen, for a stripe width between 1 μm and 2 μm the horizontal and vertical MFD are almost identical. For a stripe width of less than 2 μm the MFD increases, thus the mode becomes more delocalized and extends largely into the dielectric. For a stripe width larger than 2 μm the LR-SPP mode is relatively well localized on the stripe since the MFD

in the x-direction is only slightly larger than the corresponding stripe width. This MFD behavior is similar to of what can be found for standard TE dielectric wave-guides [30]. For increasing stripe width, the MFD in the vertical (y) direction asymptotically approaches the value obtained analytically for a gold film of infinite width.

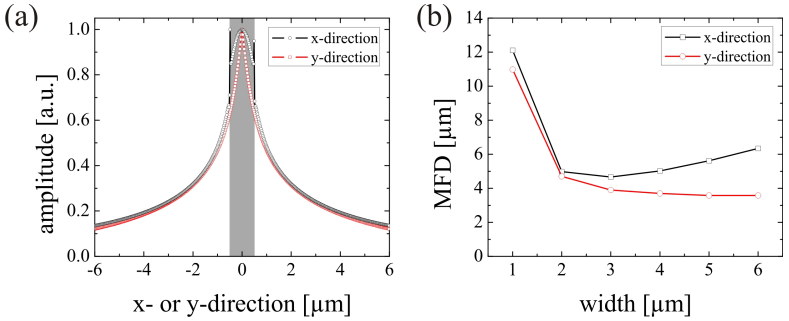

Figure 2.6: (a) Intensity profile in horizontal and vertical direction of the mode shown in Fig. 2.4. The grey shaded area illustrates the width of the metal stripe. (b) MFD as a function of the stripe width.

2.3 Surface Plasmon Polaritons on Nano-wires

The derivation and analysis of SPP modes on thin conducting wires is the topic of this section. If the wire radius is of the order of 10th of nanometers, these wires are usually refereed to as nano-wires.

The nano-wire structure under consideration is illustrated schematically in Fig. 2.7. It is a cylinder of radius R, which is centered around the z-axis and surrounded by an insulating material with dielectric constant ϵ_1. The optical properties of the cylinder are described by the dimensionless dielectric constant ϵ_{met}. Similar to the description in the previous section, of particular interest is the case of a conducting nano-wire surrounded by a lossless dielectric medium with $Re\{\epsilon_{\text{met}}\} < 0$ and $Im\{\epsilon_1\} = 0$. For solving such a system with a

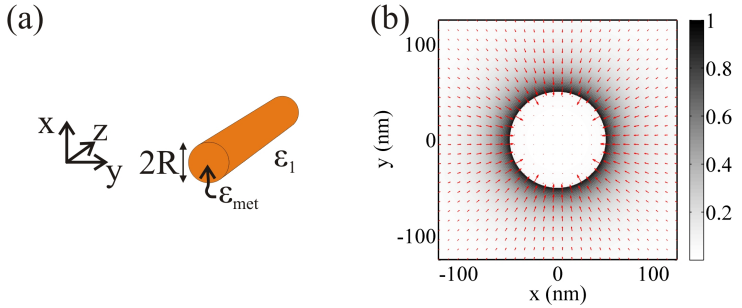

Figure 2.7: (a) Sketch of a nano-wire of radius R with dielectric constant ϵ_{met} embedded in non-conducting material with dielectric constant ϵ_1. (b) Normalized power density plot of the fundamental mode $m = 0$ for a silver nano-wire of radius $R = 50$ nm surrounded by a non-conducting material of dielectric constant $\epsilon_1 = 2$ for a vacuum wavelength $\lambda_0 = 700$ nm.

high degree of symmetry, one can use the separation of variables and find field solutions $\mathbf{E}$ and $\mathbf{H}$ to Maxwell's equations, as described for instance in [31]. In cylindrical coordinates, with radius $r = \sqrt{x^2 + y^2}$ and azimuthal angle ϕ, the electric field might be written as

$$\mathbf{E}_{\text{i}} = \mathcal{E}_{\text{i,m}} \mathbf{E}_{\text{i,m}} \left(k_{\text{i}\perp} r\right) e^{im\phi} e^{ik_{\parallel} z}, \tag{2.16}$$

where i = {met,1 } denotes the regions inside and outside of the cylinder and m is an integer describing the winding of the mode. A normalized power density plot of the lowest order mode for a wire of $R = 50$ nm is shown in Fig. 2.7 (b). The red arrows indicate the direction of the electric field E_{x} and E_{y}. The longitudinal component of the wave-vector $k_{\parallel}$, which is the modes complex propagation constant, is related to the wave vector $k_i = \sqrt{\epsilon_i} 2\pi/\lambda_0$ in region i and the transverse wave vector $k_{\text{i}\perp}$ via $k_{\text{i}}^2 = k_{\parallel}^2 + k_{\text{i}\perp}^2$. The electric field $\mathbf{E}_{\text{i,m}}(k_{\text{i}\perp} r)$ represents some normalized mode profiles and the coefficients $\mathcal{E}_{\text{i,m}}$ must satisfy a set of equations that enforce the necessary boundary conditions at the metal-dielectric interface $r = R$. A non-trivial solution of the nano-wire structure is given by the mode

equation [14]

$$\frac{m^2 k_\parallel^2}{R^2}\left(\frac{1}{k_{met\perp}^2}-\frac{1}{k_{1\perp}^2}\right)^2=\left[\frac{1}{k_{met\perp}}\frac{J_m\prime(k_{met\perp}R)}{J_m\prime(k_{met\perp}R)}-\frac{1}{k_{1\perp}}\frac{H_m\prime(k_{1\perp}R)}{H_m\prime(k_{1\perp}R)}\right]\times \left[\frac{k_{met}^2}{k_{met\perp}}\frac{J_m\prime(k_{met\perp}R)}{J_m\prime(k_{met\perp}R)}-\frac{k_1^2}{k_{1\perp}}\frac{H_m\prime(k_{1\perp}R)}{H_m\prime(k_{1\perp}R)}\right], \tag{2.17}$$

where J_m and H_m are m-th order Bessel - and Hankel functions, respectively. As a function of m, R, and ϵ_i, Eqn. (2.17) determines the allowed values of $k_\parallel$.

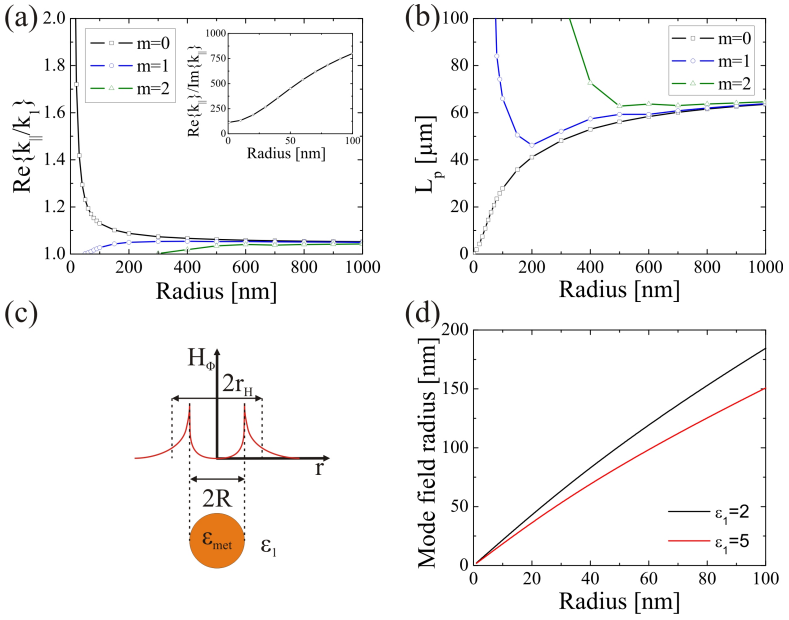

Figure 2.8: (a) Real part of the allowed plasmon modes $Re\{k_\parallel\}$ versus the radius of the nano-wire for different mode indices m. Plotted in the inset is $Re\{k_\parallel\}/Im\{k_\parallel\}$, which is finite as $R \to 0$. (b) Plasmon mode propagation length $L_p = \left(2Im(k_\parallel)\right)^{-1}$. (c) Illustration of the mode field radius r_H. (d) Mode field radius versus the wire radius R for two different ϵ_1.

The following solutions are being obtained for a vacuum wavelength $\lambda_0 = 700$ nm. Silver is used as a metal and the Drude model Eqn. (2.13) is applied to calculate $\epsilon_{\text{met}}(\omega)$. The surrounding non-conducting material is assumed to have a dielectric constant $\epsilon_1 = 2$. In Fig. 2.8 (a), the allowed wave vectors $k_{\|}$ for the three lowest order modes m are shown as a function of the wire radius R, obtained by solving Eqn. (2.17) numerically. For a wide range of wire radii the structure supports higher order modes ($m \geq 1$) which are cut-off at a radius $R \approx 50$ nm. For smaller wire radii only the lowest order mode ($m = 0$) is supported, which is characterized by a $k_{\|} \sim 1/R$ dependency. As an example, the mode profile as well as the polarization of the $m = 0$ mode of a wire with a radius $R = 50$ nm is shown in Fig. 2.7 (b). For a decreasing wire radius the fundamental mode becomes more tightly confined to the metal-insulator interface, what causes the propagation losses to increase. This is illustrated in Fig. 2.8 (b), where the plasmon propagation length $L_p = \left(2Im(k_{\|})\right)^{-1}$ is plotted versus R. Nevertheless, as $R \to 0$ the ratio $Re\{k_{\|}\}/Im\{k_{\|}\}$ approaches a non-zero value, as displayed in the inset of Fig. 2.8 (a). This means that the mode can still travel some distance of the order of a few nm even though the mode is tightly confined to the wire surface and very lossy. It should be noted, that these results are based on classical calculations with the assumption that the properties of bulk silver remain valid as $R \to 0$.

An additional parameter of interest is the mode field radius r_{H} of the $m = 0$ mode. r_{H} is defined through the decay of the azimuthal component of the magnetic field $H_{\phi,1}$ in region 1 and given by the equation $H_{\phi,1}(r_{\text{H}}) = e^{-1}H_{\phi,1}(R)$ [2]. The mode field radius r_{H} is illustrated schematically in Fig. 2.8 (c). In Fig. 2.8 (d), r_{H} is plotted versus R for two different ϵ_1. Since r_{H} decreases with R the mode remains tightly confined to the nano-wire surface, what is a remarkable feature since $R \ll \lambda$. Furthermore, for an increasing ϵ_1 the plasmon mode confinement to the wire-dielectric interface increases and simultaneously the effective plasmon mode volume V_{eff} also decreases. This behavior has consequences on the coupling efficiency of a single emitter to the plasmon mode, as will be discussed in more detail in section 6.5.1.

3

Surface Plasmon Structure Fabrication and Testing

3.1 Sample Fabrication

The basis for experiments in the field of plasmonics are metallic nanostructures with well defined shapes and material properties. Depending on the structures required, various different fabrication techniques for building plasmonic micro- and nano-structures can be used, such as UV- or electron-beam lithography followed by metal sputtering deposition or wet chemical growth using a polyol process or electrolysis. These processes are the underlying building block for the samples being studied during this work and are described below in more details.

3.1.1 LR-SPP Structures

Samples for studying LR-SPP propagation were prepared on Silicon substrates. First, a uniform layer of benzocyclobutene (BCB) polymer was spin coated with a thickness of $13-15$ μm on the substrate, and subsequently a layer of UV-resist was deposited. Second, the stripe wave guides with width ranging from 1 μm to 12 μm were patterned using standard UV-lithography, followed by the deposition of

a 14 nm or 15 nm thick gold layer, and lift-off. Third, another layer of BCB was spin coated on top of the gold structures with the same spinning conditions as used for the first one. Ensuring a symmetric structure around the metal is very important for low propagation losses and the mode field diameter. To achieve this, the top side and bottom side polymer BCB was cured under identical conditions and thick enough to accommodate the EM-field, as a comparison with Fig. 2.6 (b) shows. Finally, the waver was cut into individual samples with metal stripe length ranging from 1 mm up to 5 mm.

3.1.2 Nano-wire Structures

The silver nano-wires for the experiments described in chapters 6 were fabricated by a polyol reduction of $AgNO_3$ following the recipe described in Ref. [32]. For this process, 5 ml of Ethylene Glycol (EG) was heated in an Erlenmeyer flask with stopper to a temperature of $151.5°C$ and constantly stirred at 260 rpm. A constant temperature throughout the process is very important since a variation in temperature will lead to different results of the aspect ratio of the wires. Therefore, the Erlenmeyer flask has been placed in an oil bath. Separate solutions of 2 mg $CuCl_2 \cdot 2H_2O$, 49 mg $AgNO_3$, and 47.9 mg polyvinyl pyrrolidone (PVP) were prepared each in 3 ml of EG. After one hour waiting time 40 μl of the $CuCl_2 \cdot 2H_2O$ solution were added to the heated EG using an electronic pipette. After additional 15 minutes 1.5 ml of the PVP solution were added to the heated EG, and immediately after that 1.5 ml of the $AgNO_3$ solution. Finally, the process was run for additional 1.5 hours. During the reaction, the following color changes were observed: Within 1 min the solution turns yellow, within 3 min the solution turns red/orange, within 5 min the solution turns greenish, and then from greenish to brown/red. After 1.5 hours, the end product should be opaque grey. Finally, the end product was washed two times with acetone and one times with distilled water using a centrifuge process. In order to characterize the size distribution of the wires they were spin coated on a Si substrate and analyzed with a scanning electron microscope (SEM). In Fig. 3.1, the image of a single wire taken with a SEM is presented. The respective length- and diameter distribution of a total number of 69 wires is presented in Fig. 3.2. A majority of wires have a length

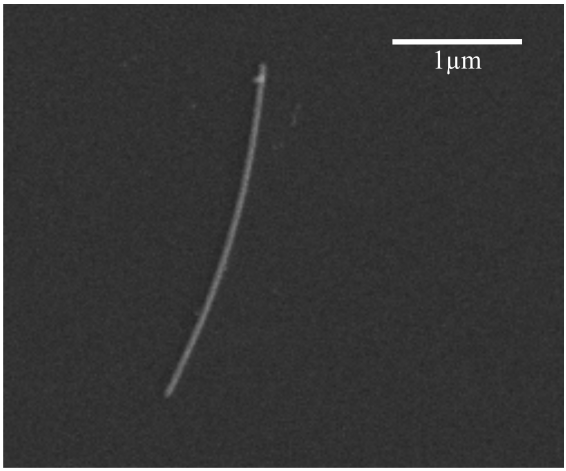

Figure 3.1: SEM image of a single, wet chemically prepared nanowire.

of > 2 μm . On one side, this assures that most of the wires are long enough to clearly resolve plasmon emission from the wire end facets in a diffraction limited microscope. On the other side, most of the wires are shorter than the plasmon propagation length $L_p = 6$ μm for a wire radius $R = 25$ nm. The majority of wires have a radius of < 50 nm, what ensures that only the fundamental mode $m = 0$ is supported at a vacuum wavelength around $\lambda_0 = 700$ nm, as seen from Fig. 2.8 and described before.

3.2 LR-SPPs Excitation

The excitation of SPPs on thin metal films has been intensely studied since the late 1970's. Excitation of bound SPP modes on thin films of (quasi) infinite and also finite width can be achieved rather efficiently via evanescent coupling using a prism in the Otto or Kretschmann configuration or grating coupling [33]. For the scope of this thesis these techniques are less preferable and 'end-fire' coupling has been used instead for the excitation of LR-SPP modes. This has been

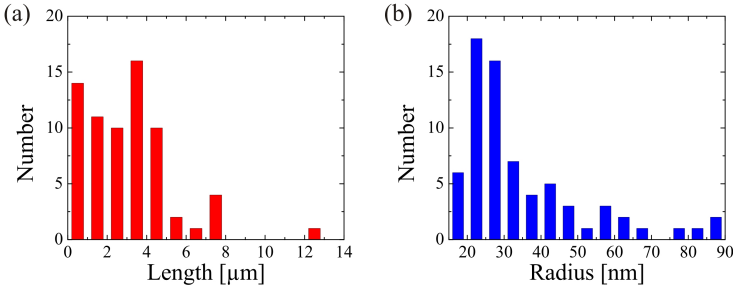

Figure 3.2: Characterization of an ensemble of fabricated nano-wires with respect to their length (a) and diameter (b).

proposed by Stegeman et al. [34] in 1983 and first demonstrated by Charbonneau et al. [35] with a fiber based setup. The underlying principle is that the LR-SPP mode profile has a very large overlap with a TEM_{00} Gaussian laser beam of similar dimension. Furthermore, the small **k**-vector mismatch between the light line and the LR-SPP mode allows that LR-SPPs can be efficiently excited by 'end-fire' coupling using free propagating laser beams. For this purpose, the freely propagating laser field with a vacuum wavelength of 1064 nm was carefully focused on the end-facet of the metallic stripe to ensure a good mode matching between the LR-SPP mode and the laser mode. The re-emitted light field was either measured with an analogue detector or imaged with a CCD camera. A typical image of an out-coupled LR-SPP mode is shown in Fig. 3.3 (a). Fig. 3.3 (b) shows the absolute LR-SPP transmission versus the polarization of the incident light field. 0° is corresponding to TM-polarized incident light and 90° is corresponding to TE-polarized incident light with respect to the metal stripe surface. The transmission is maximized for TM polarized light in agreement with the theory described in section 2.2 and decreases as $\sim \cos(\alpha)^2$ while turning the polarization from TM to TE. For TE polarized light, only scattered as well as higher order modes are measured at the output of the waveguide. These higher order modes are also partly measured on the output and explain the offset in the measurement for TE polarized incident light.

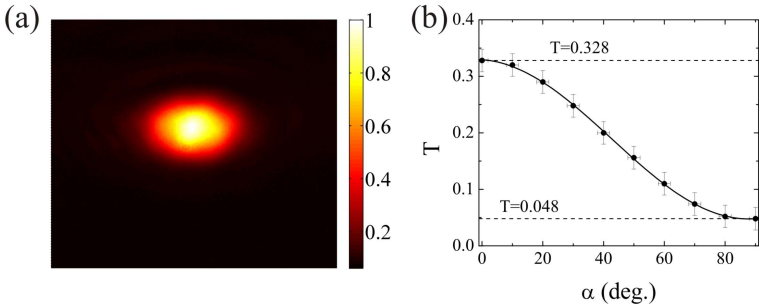

Figure 3.3: (a) Image of the LR-SPP output mode of a gold stripe with a width of 2 μm , a height of 14 nm, and a length of 2 mm for a TM-polarized incident light. (b) LR-SPP absolute transmission of the mode shown in (a) versus the polarization of the incident light field.

3.3 Fabry-Pérot like Resonances of LR-SPPs

Introduction

Provided that the metal stripe end faces reflect an incident propagating SPP, a thin metal stripe can be understood as a surface plasmon resonator. In this case, resonator modes exist whenever half an integer of the surface plasmon wavelength equals the metal stripe length. However, due to surface plasmon propagation losses the maximum achievable resonator length is limited by the plasmon propagation losses. In the literature, a number of experiments were reported observing SPP resonances on silver nano-wires [4, 36, 37] and gold or silver films with slit-grove nano-structures [38]. In all these studies, SPPs were excited by illuminating the structures with a broad band light source. The transmitted spectra showed clear periodic modulations, which could be used, for instance, to calculate the SPP group velocity and determine propagation losses.
In this section, the observation of Fabry-Pérot like resonances on gold stripes supporting LR-SPP modes is reported. The cavity mirrors are

formed by the front and end faces of the metal stripe. In a simplified picture, the mode index difference between the plasmon mode and free space modes can be used to calculate the reflection coefficient according to Fresnel equations [30] under normal incidence. Instead of observing periodic spectral fluctuations, as done in other studies, the length of LR-SPP waveguide will be changed slightly, what is enabled by the comparatively large coefficient of thermal expansion of the surrounding BCB.

Experiment

A schematic diagram of the experiment is shown in Fig. 3.4 (a). To excite the LR-SPP mode, a strong laser beam has been guided through a highly asymmetric beam splitter with a power reflectivity of 99%. Subsequently, the light from the low transmission port was mode matched to the LR-SPP mode using 'end-fire' coupling, as illustrated in Fig. 3.4 (a). The sample holder itself was composed of

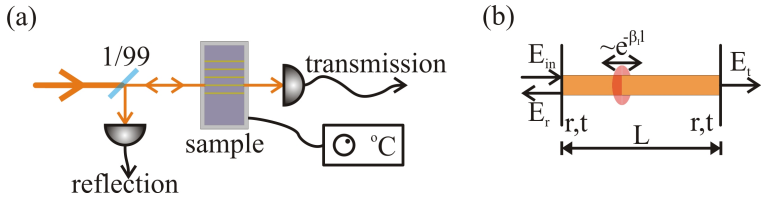

Figure 3.4: (a) Schematic diagram of the experimental setup to measure the transmission and reflection properties of LR-SPPs: 1/99 - asymmetric beam splitter with a power transmissivity and reflectivity of 1% and 99%, respectively. The sample was mounted on a peltier element to control its temperature. Not shown are the optics for mode matching the free propagating laser beam to the LR-SPP mode. (b) Illustration for calculating the absulute power transmission and reflection coefficients: r,t - reflection and transmission from a single interface.

a thermoelectric element and a bras block on top of it, where the sample was positioned. The thermoelectric element uses the peltier

effect to adjust the temperature of the sample. Above the thermoelectric element and approximately 1 mm underneath the sample, the temperature was measured on the sample mount using a $10k\Omega$ temperature sensor[1]. The short distance between the sensor and the SPP sample ensures that the recorded temperature corresponds most accurately to the temperature of the sample. As illustrated in Fig. 3.4 (a), the light transmission has been measured directly behind the sample. The re-emitted SPP mode was collimated by a lens, guided through a pin hole in order to suppress stray light, and detected using a pin-photodiode. The excitation of the LR-SPP mode was verified by testing its polarization dependence according to the measurement shown in Fig. 3.3 (b). The reflected signal has been accessed via the highly reflecting port of the asymmetric beam splitter, as illustrated in Fig. 3.4 (a), and recorded with a similar photodiode as used for the transmission measurement. For all measurements carried out in this experiment the power incident on the sample has been adjusted to 0.5 mW. Using the effect of thermal expansion, the temperature of the sample will be changed in order to vary the length of the gold stripe on the order of a few μm . Due to thermal expansion of the sample holder and the sample itself, it was necessary to re-align the incident laser beam for every sample temperature adjustment.

Results

The measured transmission and reflection coefficients for three LR-SPP wave-guides of length 2 mm, 4 mm, and 5 mm are presented in Fig. 3.5. The LR-SPP wave guides were produced on the same Si waver with a gold stripe cross section of 2 μm by 14 nm. It can be seen from Fig. 3.5 that by increasing the sample temperature the transmission and reflection coefficients vary as $\cos^2(\omega_T T + \delta_T)$, where T is the temperature, ω_T is the period of the variation oscillation, and δ_T is a phase constant. Furthermore, the transmission maxima (minima) overlap precisely with the reflection minima (maxima). In addition, the amplitude decreases with increasing waveguide length. Since the LR-SPP waveguide length increases with increasing sample temperature due to thermal expansion, the observed behavior suggests that

[1]Epcos 8407 with $R(T = 25^\circ C) = 10k\Omega$.

the oscillation can be explained by a Fabry-Pérot cavity like effect. The model for this is illustrated in Fig. 3.4 (b), where E_{in}, E_{r}, and E_{t} are the electric field amplitudes of the incident mode, the reflected mode, and the transmitted mode, respectively. r, t are the electric field reflection and transmission coefficients obtained from n_{eff} via $r = \frac{n_{\mathrm{eff}}-1}{n_{\mathrm{eff}}+1}$ and $t = \sqrt{1-r^2}$. It is assumed that the LR-SPP is a plane wave and the polarization dependence can be neglected. The imaginary part of the propagation constant of the mode is expressed as β_I. As the mode propagates along the gold stripe, the electric field amplitude decreases as $\sim e^{-\beta_I l}$, where l is the length the mode propagate.

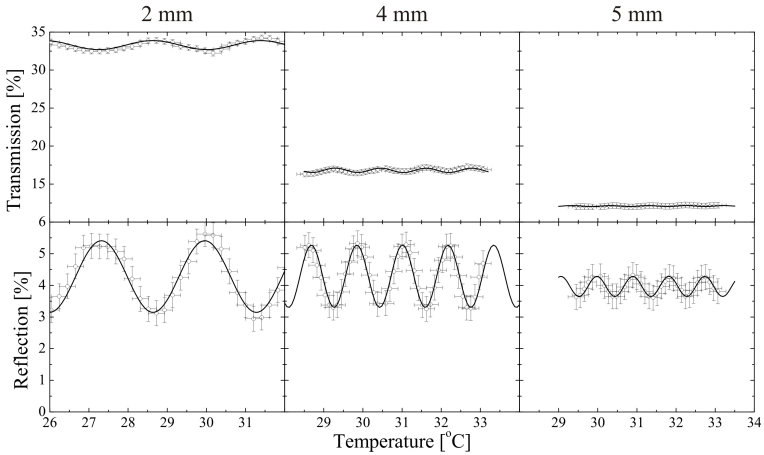

Figure 3.5: Transmission and reflection through LR-SPP wave-guides for various length versus the temperature of the wave-guide. The stripe width and height are 2 μm and 14 nm, respectively, for all wave-guides.

Before investigating the LR-SPP transmission and reflection, the thermal expansion of the sample will be analyzed. Assuming that the thermal expansion of the sample is linear, the change of the waveguide length ΔL goes with the temperature change ΔT as

$$\Delta L = \alpha_{\mathrm{L}} L \Delta T, \tag{3.1}$$

where α_{L} is the coefficient of thermal expansion (CTE) and L is the initial length of the sample. Assuming that the oscillations in Fig. 3.5 arise from a standard Fabry-Pérot cavity like effect as described above, one identifies the distance between two transmission maxima m and $m+2$ to be a cavity length change of $\Delta L = \lambda_0/n_{\mathrm{eff}}$. Combining this with Eqn. (3.1), one can find a linear relation between the oscillation frequency ω_{T} and the cavity length

$$\omega_{\mathrm{T}}(L) = \frac{\alpha_{\mathrm{L}} n_{\mathrm{eff}} L}{\lambda_0}. \tag{3.2}$$

A plot of $\omega_{\mathrm{T}}(L)$ versus the sample length L is shown in Fig. 3.6 (a). From the fit to the data points the thermal expansion coefficient α_{L} is determined to be $\alpha_{\mathrm{L}} = 80 \cdot 10^{-6} \pm 1.71 \cdot 10^{-6}\,^{\circ}\mathrm{C}^{-1}$, where $n_{\mathrm{eff}} = 1.539$ has been used. In the literature, the CTE of BCB is specified to be $\alpha_{\mathrm{BCB}} = 42 \cdot 10^{-6}\,^{\circ}\mathrm{C}^{-1}$ [39], which is comparable to the measured value. It should be noted, that also different values have been reported in other references, see e.g. [40], which are more close to the value measured here. The reason why the measured CTE is higher than other values reported in the literature is not quite clear. Bad thermal coupling between the sample holder and the sample itself would suggest even higher oscillation frequencies and therefore an even larger α_{L}. One possible reason is that the determined α_{L} arises from an increased temperature around the gold stripe, where due to the LR-SPP dissipation the temperature is locally increased. The expansion effect of the silicon substrate and the gold stripe itself can be neglected. At room temperature the CTEs of silicon and gold are specified to be $\alpha_{\mathrm{Si}} = 2.6{\cdot}10^{-6}\,^{\circ}\mathrm{C}^{-1}$ [41] and $\alpha_{\mathrm{Au}} = 14{\cdot}10^{-6}\,^{\circ}\mathrm{C}^{-1}$ [42], which are much smaller than the α_{L} measured here.

In the following, the transmission and reflection amplitudes will be investigated in greater details. Solving the model of Fig. 3.4 (b) for an infinite number of round trips, one can calculate the power reflection and transmission coefficients for a Fabry-Pérot resonator of length L, which are given by

$$R(\delta) = \frac{r^2\left(1 + a^4 - 2a^2\cos(\delta)\right)}{1 + (ra)^4 - 2(ra)^2\cos(\delta)} \quad \text{and} \tag{3.3}$$

$$T(\delta) = \frac{a^2\left(1 - r^2\right)^2}{1 + (ra)^4 - 2(ra)^2\cos(\delta)}, \tag{3.4}$$

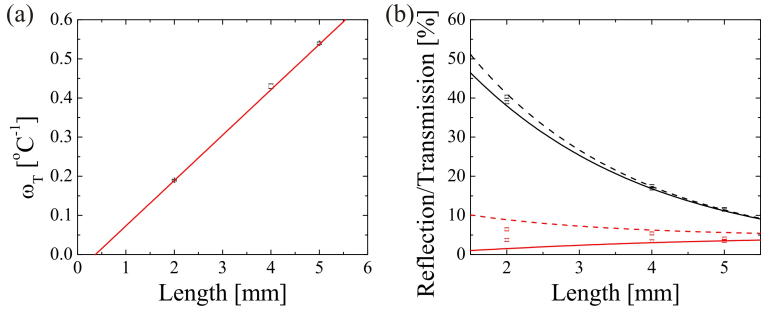

Figure 3.6: (a) Oscillation frequency ω_{T} versus sample length. (b) Modeled maximum (dashed lines) and minimum (solid lines) transmission (black lines) and reflection (red lines) for a lossy Fabry-Pérot cavity with an imaginary LR-SPP propagation constant of $\beta_{\mathrm{I}} = 209.3\,\mathrm{m}^{-1}$.

where $a = e^{-\beta_{\mathrm{I}} L}$ describes the damping of the electric field amplitude per half round trip and $\delta = 2k_{\parallel}L$ is a phase factor for a given resonator length. For an infinite resonator length L the reflection coefficient approaches the value for a single interface $R_{L\to\infty} = r^2$ and the transmission $T_{L\to\infty} = 0$. Using β_I as a fitting parameter and accounting for mode matching inefficiencies between the incident laser mode and the LR-SPP mode, these equations have been fitted to the minimum and maximum reflection and transmission coefficients, as presented in Fig. 3.6 (b). Experimentally, mode matching inefficiencies can arise due to sample cleaving inaccuracies or different mode field properties of the incident laser field, since the setup needed to be slightly modified for different stripe lengths. From the fit shown in Fig. 3.6 (b), an imaginary part of the refractive index $Im\{n_{\mathrm{eff}}\} = \beta_{\mathrm{I}}/k_0 = 3.54 \cdot 10^{-5}$ is obtained, which is more than three times larger than the value expected from the simulation presented in Fig. 2.5 (b) for a stripe width of 2 μm and even slightly larger than the value for a stripe of infinite width.

Conclusion

In conclusion, oscillations of the LR-SPP transmission and reflection have been observed upon changing the temperature of the LR-SPP sample. From the oscillation frequency, the coefficient of thermal expansion of the composite BCB gold structure hosting the LR-SPP mode has been determined to be $\alpha_{\mathrm{L}} = 80 \cdot 10^{-6} \pm 1.71 \cdot 10^{-6}\,^{\circ}\mathrm{C}^{-1}$, which is bigger than the values for BCB reported in the literature. The observed behavior is explained by a Fabry-Pérot cavity model with LR-SPP propagation losses as a damping factor. The imaginary part of the propagation constant has been determined to be $3.54 \cdot 10^{-5}\mathrm{m}^{-1}$, a value which is higher than obtained from a finite element model.

4

Non-linear Propagation of Surface Plasmon Polaritons

4.1 Introduction

The nonlinear properties of SPP modes have been studied much less than the linear properties although it is well known that the nonlinearity of metal may be significant. The second order nonlinearity of metal surfaces has been explored already in the sixties (see, e.g. [43]). It was shown that the second-harmonic response is strongly enhanced if the surface is illuminated under the right angle to excite the SPP mode due to the enhancement of the local field at the surface [44]. Later, most experiments focussed on dielectric materials with embedded metallic nano-particles, thus exploiting the nonlinear response of the metal in an otherwise transparent medium (see e.g. the review [45]). Experiments exploring non-linear effects in transmission through pure metallic and very thin samples were reported only recently, e.g. [46, 47, 48]. These experimental and theoretical studies showed that there is a strong third order $\chi^{(3)}$ Kerr non-linearity in metallic media, resulting in an intensity dependent refractive index. In standard non-linear optics, the intensity dependent refractive index is described as $n = n_0 + 2n_2|E(\omega)|^2$, where n_0 represents the weak field refractive index and $n_2 = \frac{3\chi^{(3)}}{4n_0}$ [49]. The main contribu-

tions to the third order susceptibility $\chi^{(3)}$ in bulk metal arises from the immediate nonlinear response of the dipole transitions between the valence and conduction bands (the interband contribution $\chi^{(3)}_{\mathrm{ib}}$) and the heating of the electron gas (the hot electron contribution $\chi^{(3)}_{\mathrm{he}}$). The third order non-linear strength of gold were estimated experimentally as [45]

$$\begin{aligned} \mathrm{Im}\,\chi^{(3)}_{\mathrm{ib}} &\approx -10^{-8}\,\mathrm{esu} \quad \text{and} \\ \mathrm{Im}\,\chi^{(3)}_{\mathrm{he}} &\approx +10^{-7}\,\mathrm{esu}. \end{aligned}$$

Electrons are assumed to respond fast to the excitation and due to the positive sign of $\mathrm{Im}\,\chi^{(3)}_{\mathrm{he}}$ it is expected to observe a saturation effect of the absorption.
In this chapter the measurement of the third order nonlinearity of a LR-SPP mode on a thin gold film is reported. A nonlinear absorption as well as a nonlinear phase shift is demonstrated, thus measuring the imaginary and the real part of the Kerr coefficient, respectively. In addition to the fast Kerr nonlinearity, a strong thermal effect is measured which increases the LR-SPP absorption due to the absorbed photon energy.

4.2 Non-linear Absorption of a Continuous Laser Beam

A simplified schematic diagram of the experimental setup is presented in Fig. 4.1. The incident laser beam with a vacuum wavelength of $\lambda_0 = 1064$ nm has been modulated using a fast rotating disc with alternating transparent and absorbing elements. The rotating disc was placed at the position of the beam waist to obtain fast switching of the light. The input power P_{in} was measured before the rotating disc. For temperature stabilization the sample has been mounted on a piezo electric element, as explained in section 3.3. The time dependence of the output power P_{out} for a 3 mm long gold stripe is shown in Fig. 4.2 (a) for four different input powers P_{in}. One can see that after the chopper wheel opening, P_{out} increases on a time scale of the order of hundred μs for all input power. For larger input

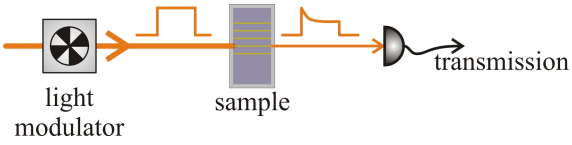

Figure 4.1: Simplified schematic diagram of the experimental setup for measuring the non-linear properties of LR-SPPs: The laser beam is modulator by a fast rotating disc with alternating transparent and absorbing elements. Not shown are the optics for mode matching the free propagating laser beam to the LR-SPP mode.

powers, the output power first increases before it slowly relaxes to a steady-state value. From this result one can conclude that two processes contribute to the non- linear absorption of the plasmon. First, a fast nonlinear effect increases the transmission similar to a saturable absorber. Second, the decrease on longer time scales might be attributed to a slow heating effect which increases the absorption of the gold film. However, the results in Fig. 4.2 (a) are not sufficient to determine the timescales of the two effects due to the limited time resolution of the detection setup. This point will be discussed in the following sections. The following discussion focuses on the steady state transmission on a time scale of approximately 1 ms.

Fig. 4.2 (b) shows the measured values of the transmission coefficient $T = P_{\mathrm{out}}/P_{\mathrm{in}}$ as a function of the input power for different lengths of the stripe. One observes that the transmission first increases with the input power due to the nonlinear saturation of the absorption. However, the transmission decreases again for larger input powers, which is attributed to the heating of the sample. Such a light induced heating effect cannot be completely counteracted by the Peltier cooling mechanism. This is corroborated by the fact, that the transmission decrease is stronger for the steady state transmission T_{ss} (shown in Fig. 4.2 (b)) than for the peak value T_{peak} (cf. Fig.4.2 (a)) right after switching on the laser beam. Simultaneous measurements of the Peltier current confirm a sample heating, as shown for instance in Fig. 4.2 (c). In order to verify that the nonlinear effect originates from the metal and not from the surrounding dielectric, the laser

beam was also sent through pure BCB of 1 mm length. No notable change of the transmission with the input power was observed.

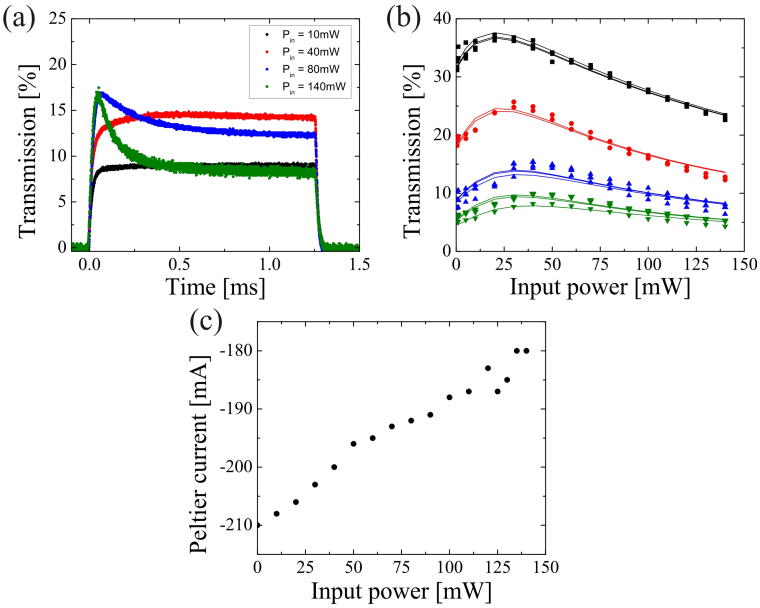

Figure 4.2: (a) Time dependence of the transmission of a plasmonic waveguide of length $l = 3$ mm for four different values of the input power P_{in}. (b) Intensity dependence of the absorption of the LR-SPP mode on a thin gold film of length 2 mm (black), 3 mm (red), 4 mm (blue), and 5 mm (green) for a cw input in the steady state. The dots are experimental values and the solid lines are a fit according to Eqn. 4.1. (c) Peltier current, that is related to the sample temperature, versus the input power for a 4 mm long stripe.

In order to model the saturation effect the absorption is assumed to be described by the modified Lambert-Beer law

$$\frac{dP(z)}{dz} = \alpha(P)P(z). \tag{4.1}$$

The absorption coefficient $\alpha(P)$ depends on the actual value of the

transmitted power and is comprised of three contributions. First, a linear absorption loss and scattering losses from surface roughness and impurities are taken into account. These two effects are not distinguished in the described transmission experiments and the corresponding absorption coefficient is denoted as ξ. Second, there are slow thermal effects due to the heating of the sample. The temperature change of the film at steady-state is proportional to the power dissipated in the metal. It is assumed that the heating effect increases the absorption coefficient by an amount given by γP. Third, the intensity-dependence of the absorption coefficient of the metal, i.e. the true Kerr effect, is dominated by two contributions [45]: The saturation of electronic interband transitions and the so called 'hot electron' contribution. Following [50], a saturable absorber-like nonlinearity is assumed with coefficients β and P_{sat}. Then, the total absorption coefficient can be written as

$$\alpha(P) = \xi + \gamma P + \frac{\beta}{1 + P/P_{\mathrm{sat}}}, \tag{4.2}$$

where the parameters are determined by the experimental data. For the fit of the output power, Eqn. (4.1) was numerically integrated for every sample and every value of the input power. The complete data is fitted simultaneously with the same values of the material parameters ξ, γ, β and P_{sat}.
Furthermore, it is assumed that the coupling to the LR-SPP mode is not perfect so that $P(z = 0) = C_{\mathrm{n}} P_{\mathrm{in}}$, where C_{n} is the coupling efficiency to sample n. For each sample this coupling efficiency can be different, but it is assumed that it does not depend on the input power. The result of the fits are compared to the measurement data in Fig. 4.2, showing good agreement for the complete power range and the various samples of different length. The following values for the fit coefficients were found

$$\begin{aligned} \xi &= 3.2 \times 10^{-7}\mathrm{m}^{-1}, \\ \gamma &= 16\mathrm{mW}^{-1}\mathrm{m}^{-1}, \\ \beta &= 610\mathrm{m}^{-1}, \quad \text{and} \\ P_{\mathrm{sat}} &= 8.9\mathrm{mW}. \end{aligned}$$

The fitted values for the coupling efficiencies C_{n} all lie between 50%

and 63%. Taking into account an in-coupling efficiency of 63%, an imaginary part of the refractive index of 10×10^{-5} is found. This value is about three times higher than what one expects for a gold stripe with a height of 15 nm.

4.3 Non-linear Absorption of a Pulsed Laser Beam

In order to further explore the nonlinear absorption of a plasmon and to determine the time scales of the different nonlinear effects, transmission measurements of laser pulses in the micro- to millisecond time scale were studied. The laser pulses for these studies were generated by a mode filtering cavity that is scanned through the resonance by a movable mirror mounted on a piezoelectric crystal, as illustrated in Fig. 4.3. This generates a Lorentzian input pulse whose peak power

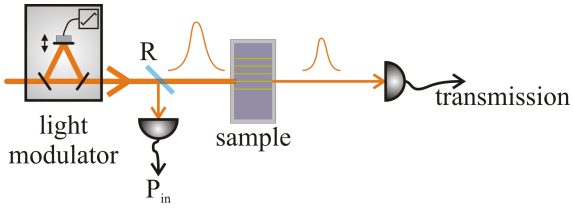

Figure 4.3: Simplified schematic diagram of the experimental setup for measuring the non-linear absorption of LR-SPPs excited with a pulsed laser beam. The laser beam is modulated by scanning a high Finesse cavity through the resonance. Approximately $R = 2.2\%$ were tapped off after modulation for calibrating the input power P_{in}.

is given by the power of the incident cw laser. Simultaneously to the recording of the output power P_{out}, the input power P_{in} has been measured by tapping off approximately 2.2% of the beam after modulation. The transmission was recorded for different pulse lengths as well as for different peak powers. In a first set of experiments the transmission through a plasmonic mode on a thin metal stripe was measured for short pulses with a maximum peak power of 150 mW

and eight different values of the pulse duration. The metal stripe had a width of 2 μm , a height of 15 nm, and a length 3 mm. Fig. 4.4 (a)

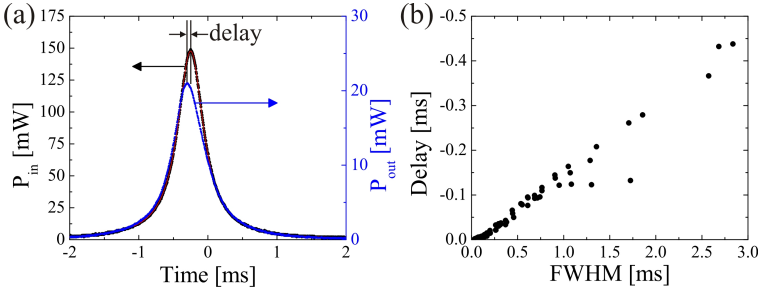

Figure 4.4: (a) Transmission of a laser pulse through a LR-SPP mode on a 3 mm long gold film. The shape of the output pulse (blue dots, right scale) is compared to the incident pulse (black dots, left scale). The red line is a Lorentzian fit to the incident pulse, from which the FWHM of this pulse was determined to be 0.457 ms. (b) Delay of the output pulse as a function of the FWHM of the input pulse.

shows an example of the time dependence of the input and the output pulse after transmission through the plasmon mode. Obviously, the shape of the output pulse is significantly changed as the transmission depends on the input power. Furthermore, a hysteresis behavior is observed: The absorption is stronger for the falling than for the rising part of the pulse. This proves that the nonlinear effect increasing the absorption is not instantaneous but rather acts on a timescale in the micro- to millisecond regime, which is typical for thermal effects in nano-scale photonic structures [49]. A notable consequence is that the output pulse appears to be shifted to earlier times, as shown in Fig. 4.4 (a) and summarized for several pulses in Fig. 4.4 (b).

In order to describe this behavior quantitatively the absorption is fitted according to Lambert-Beer's law (4.1) as described in the previous section. However, now the non-instantaneous thermal effects have to be taken into account. Thus, the thermal part of the nonlinear absorption coefficient (4.2) is substituted with a time dependent

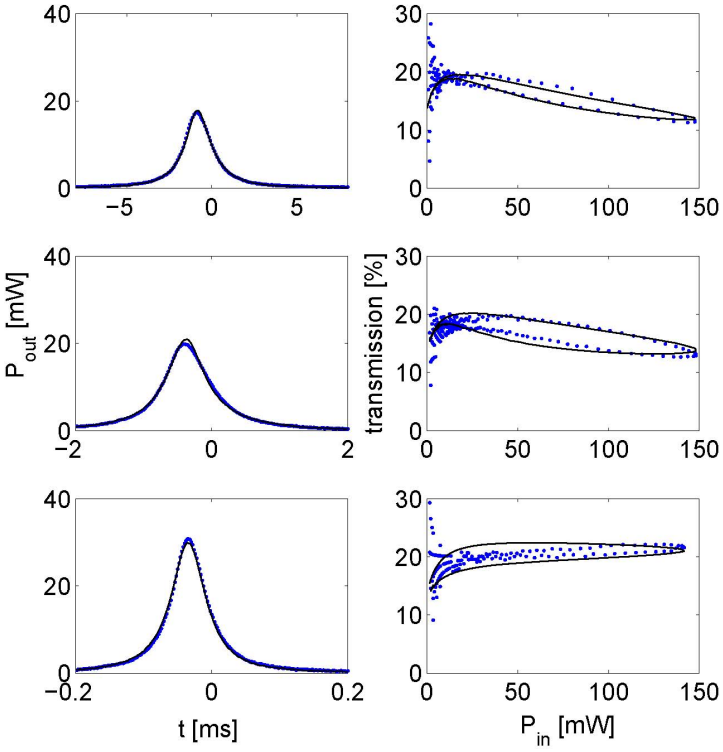

Figure 4.5: Transmission of laser pulses with different durations of 1.4 ms (top), 0.6 ms (center), and 0.06 ms (bottom) through a LR-SPP mode on a 3 mm long gold film: Left panel - output power vs. time, right panel - transmission vs. input power. The blue dots are the experimental data and the black solid lines are fits as described in the text.

term and it now reads

$$\alpha(z,t) = \xi + \frac{\beta}{1 + P(z,t)/P_{sat}} + \frac{\gamma}{\tau} \int_{-\infty}^{t} e^{(t-t')/\tau} P(z,t')dt'. \quad (4.3)$$

The exponential memory kernel with time constant τ in Eqn. (4.3)

arises when it is assumed that the heat diffuses out of the sample. The experimental data of the eight measurements was then fitted with the time dependent absorption coefficient (4.3), the output of which is shown in Fig. 4.5. The resulting values for the fit parameters are given by

$$\begin{aligned} \xi &= 294 \times 10^{-6}\mathrm{m}^{-1}, \\ \gamma &= 5.2\mathrm{W}^{-1}\mathrm{m}^{-1}, \\ \beta &= 202\mathrm{m}^{-1}, \\ P_{\mathrm{sat}} &= 1.8\mathrm{mW}, \text{and} \\ \tau &= 0.22\mathrm{ms}. \end{aligned}$$

A good agreement of the fits and the experimental data is observed. It is notable, that the hysteresis behavior due to the thermal effect is most pronounced for input pulses with an intermediate duration, i.e. when the input pulses FWHM is of the order of τ like for the central graphs in Fig. 4.5. For longer pulses, the slow thermal nonlinearity affects the rising and falling parts of the pulse in almost the same way (cf. the top graphs in Fig. 4.5) while it has no significant effect for the short pulses at all (cf. the bottom graphs in Fig. 4.5).

4.4 Non-linear Phase Shift

The real part of the third order susceptibility introduces a phase shift on the light field propagating through the medium. In order to measure the phase shift induced by the LR-SPP mode an interferometric setup has been used, as shown in Fig. 4.6. A Lorentzian input pulse is generated by the same modulated filter cavity and then split on a 96/4 beam splitter to form a strong pump and a weak probe beam. Both beams pass the interferometer in counter propagating directions, which includes the passage through a plasmonic waveguide with a length of $l = 3$ mm. Finally, the beams are recombined and the output power is measured in order to reconstruct the interference pattern.
Both plasmonic modes, the pump and the probe, experience a phase shift due to the Kerr effect. However, the phase shift of the probe beam is generated by cross-coupling from the strong pump beam

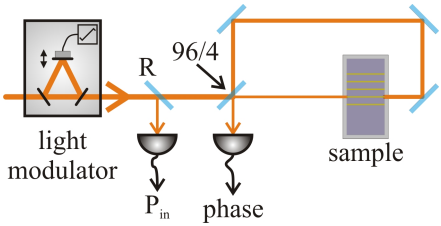

Figure 4.6: Simplified schematic diagram of the experimental setup for measuring the non-linear phase shift induced by of LR-SPPs. The laser beam is modulator by scanning a high Finesse cavity through the resonance. Approximately $R = 2.2\%$ were tapped off after modulation for calibrating the input power P_{in}.

and is thus twice as large. This is the so called weak-wave retardation [49], where nonlinear effects induced by the weak probe beam are discarded. Thus, the focus lies only on the nonlinear phase shift induced by the strong pump beam.
After the passage through the plasmon, the two beams therefore acquire a phase shift which is given by

$$\frac{d\phi(z,t)}{dz} = \beta P(z,t) + \frac{\gamma}{\tau}\int_{-\infty}^{t} e^{(t-t')/\tau} P(z,t')\,dt'. \tag{4.4}$$

Again, a fast contribution with strength β and a slow contribution with strength γ and a time constant τ are taken into account. The slow thermal contribution was derived as follows. The thermal part of the change of the index of refraction is to the first order proportional to the temperature change (cf. Eqn. (4.5.1) in [49]). The change of the temperature in time is modeled by a relaxation ansatz based on the heat equation (cf. Eqn. (4.5.2) in [49]). The heat outflow is proportional to the temperature with a relaxation time τ while the heat inflow is proportional to the laser power. Thus, the following differential equation for the time dependence of the index of refraction change is obtained

$$\frac{dn(t)}{dt} = -\frac{n(t)}{\tau} n + \frac{\gamma}{\tau} P(t), \tag{4.5}$$

which is readily integrated with the result given in Eqn. 4.4. Here, a standard Kerr type nonlinearity is assumed instead of a saturable absorber type nonlinearity. This assumption is based on the fact that a fit with a saturable absorber type nonlinearity did not lead to a good agreement with the experimental data[1]. The assumption is further supported by the theoretical analysis of Kerr nonlinerities in semiconductors, where the real part of the Kerr coefficient shows almost no saturation, while the imaginary part does [51].

For simplicity it is assumed that the power distribution of the pump beam varies only very little in time. Then, one can simply integrate the expression (4.4) over z and write

$$\phi(t) \approx \bar{\beta} P_{\mathrm{in}}(t) + \frac{\bar{\gamma}}{\tau} \int_{-\infty}^{t} e^{(t-t')/\tau} P_{\mathrm{in}}(t')\, dt'. \tag{4.6}$$

This phase shift can be measured by the interference pattern of the interferometer output.

Fig. 4.7 shows the transmission of Lorentzian pulses with different duration through the Mach-Zehnder interferometer. In the left-hand side panel, the output power $P_{\mathrm{out}}(t)$ is compared to a Lorentzian fit $P_{\mathrm{Lor}}(t)$, showing a pronounced interference pattern superimposed on the Lorentzian pulse shape. This becomes even clearer by comparing the difference between the experimental data and the Lorentzian fit, what is shown in the right-hand side panel of Fig. 4.7. This oscillating signal is then fitted with the function

$$P_{\mathrm{out}}(t) - P_{\mathrm{Lor}}(t) = c P_{\mathrm{in}}(t) \times \cos(\phi(t) + \phi_0), \tag{4.7}$$

where the phase shift $\phi(t)$ is given by Eqn. (4.6). The data from nine experimental runs with different pulse durations has been fitted, i.e. with the same values for $\bar{\beta}$, $\bar{\gamma}$, and τ. The result is plotted as a black line in the right-hand side panel of Fig. 4.7, demonstrating good agreement with the experimental data (blue line). The results

[1] Actually, a fit with a saturable absorber like nonlinearity leads to exceptionally large values for P_{sat}. But then one can replace this nonlinearity by its first-order Taylor approximation, which once again leads to a standard Kerr-type nonlinearity.

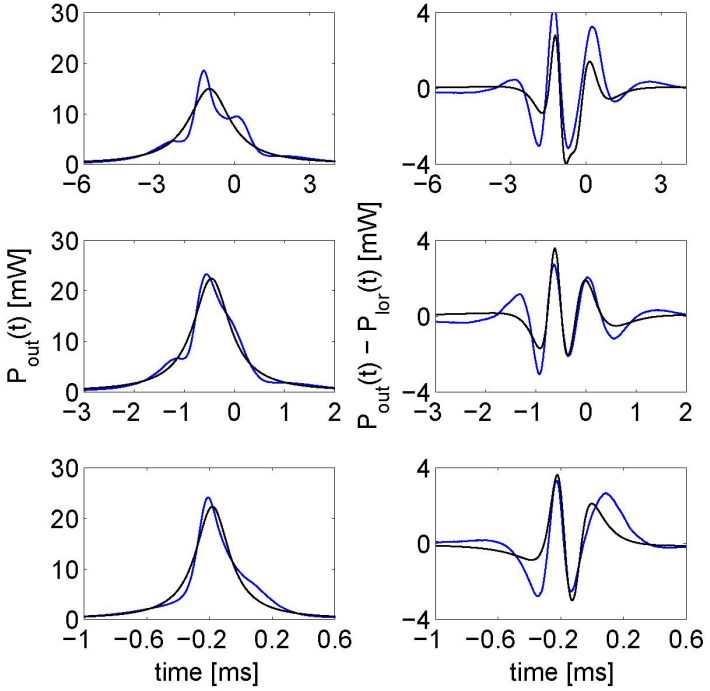

Figure 4.7: Interference pattern in the transmission through an asymmetric Mach-Zehnder interferometer due to the plasmonic Kerr effect: The left panel shows the transmitted power (blue line) compared to a Lorentzian fit (black line). The deviation from the Lorentzian is plotted on the right panel, showing a pronounced interference pattern caused by the different phase shifts of the pump and the probe beam. A fit according to Eqn. (4.7) (black line) shows a good agreement to the experimental data (blue line).

for the fit coefficients are given by

$$\begin{aligned} \bar{\beta} &= 9.57\,\mathrm{mW}^{-1}, \\ \bar{\gamma} &= 15.36\,\mathrm{mW}^{-1}, \quad \text{and} \\ \tau &= 0.63\,\mathrm{ms}. \end{aligned} \tag{4.8}$$

4.5 Conclusion and Outlook

In the present chapter the Kerr effect for a long range surface plasmon polariton mode on a thin gold film embedded in a dielectric material (BCB) has been investigated. The nonlinearity arises from the metallic stripe itself and not from the surrounding dielectric. By analyzing the nonlinear absorption as well as the phase shift, both the real and the imaginary part of the Kerr coefficient $\chi^{(3)}$ was determined.
It was shown that two effects with different time scales contribute to the nonlinear absorption. First, a slow contribution increases the absorption, which is attributed to thermal effects in the sample. The timescale of approximately 0.2 ms has been deduced from the hysteresis of the transmission curves measured with Lorentzian laser pulses of different width. Second, the genuine nonlinearity of the absorption coefficient occurs on timescales much faster than the pulses used in the present experiment, i.e. below the microsecond regime. It was shown that this effect is well described by a saturable absorber type nonlinearity with a saturation power in the mW range.
Furthermore, the nonlinear phase shift (the actual Kerr effect) was analyzed in an interferometric setup by observing the interference pattern at the interferometer output. An estimate for the Kerr coefficient induced by the metal requires a detailed analysis of the electromagnetic field. One has to include a geometrical factor accounting for the portion of the electromagnetic field which is actually guided inside the metal. This is the subject of ongoing work and will be reported elsewhere when conclusions are drawn. Simple transmission measurements through bulk BCB are not completely sufficient to exclude the impact of BCB, as reported in section 4.2. Dielectric waveguides based on pure BCB need to be fabricated and their nonlinear properties compared to the results obtained from LR-SPP waveguides with similar mode fields.
All experimental results can be understood quantitatively with a model including linear, thermal, and a saturable absorption. However, the calculated values of the fitting parameters have to be interpreted with care because it is not easy to distinguish the three different contributions from each other. For example, a change of $\xi + \beta$ has a drastic effect on the quality of the fit, whereas a simultaneous increase of ξ and a decrease of β has a weak effect only. This

is especially true for the measurement of the real part of the Kerr coefficient.
The main open problem is a careful analysis of the fast nonlinearity, which will require ultrashort laser pulses with an appropriate wavelength. A major challenge is to prove that the fast nonlinearity is indeed a coherent Kerr effect which could then be used, for instance, to generate squeezed light in an integrated plasmonic device similar to nonlinear fiber-optic interferometers [52].

Part II

Excitation of Quantized Surface Plasmon Polaritons

5

SPP Excitation with Quadrature Squeezed Light

5.1 Introduction

In the present chapter the compatibility of the quantum plasmonic technology with the continuous variable quantum domain (described in an infinite dimensional Hilbert space) is investigated by demonstrating the plasmonic excitation, propagation, and detection of deterministically prepared quadrature squeezed vacuum states. A squeezed vacuum state is used to excite an electron resonance on the surfaces of a metallic gold waveguide to form a SPP. Despite linear loss and decoherence in the plasmonic mode it is demonstrated that quadrature squeezing is retained in the retrieved light state. Importantly, the input state and output state are fully characterized by performing a complete quantum tomographic reconstruction of their density matrixes. This is in contrast to previous experiments on plasmon assisted quantum state transmission [19, 20], where only a certain property of the quantum state was investigated.

5.2 Continuous Variable Description of the Electromagnetic Field

Before investigating the quantum properties of LR-SPPs, a brief introduction to the continuous variable description of quantum optics is given in this section. Starting point for the continuous variable description of the electromagnetic field are Maxwell's equations in the absence of charges and current. After quantizing the field amplitudes, a possible solution of the electric field $\hat{E}(t)$ with frequency ω and at time t might be written as

$$\hat{E}(t) = i\hat{a}(t)e^{-i\omega t} - i\hat{a}^{\dagger}(t)e^{i\omega t}, \tag{5.1}$$

where $\hat{a}(t)$ and $\hat{a}^{\dagger}(t)$ are dimensionless annihilation and creation operators of the quantized harmonic oscillator which satisfy the commutation relation $\left[\hat{a}(t), \hat{a}^{\dagger}(t)\right] = 1$. The annihilation and creation operators are non-Hermitian and therefore not directly measurable. It is thus convenient to introduce the general quadrature operators $\hat{X}^{\phi}(t)$ and $\hat{Y}^{\phi}(t)$ via [53]

$$\hat{X}^{\phi}(t) = e^{i\phi}\hat{a}^{\dagger}(t) + e^{-i\phi}\hat{a}(t) \quad \text{and} \tag{5.2}$$

$$\hat{Y}^{\phi}(t) = i\left(e^{i\phi}\hat{a}^{\dagger}(t) - e^{-i\phi}\hat{a}(t)\right), \tag{5.3}$$

which are often referred to as the position ($\hat{X}(t)$) and momentum ($\hat{Y}(t)$) operators of the quantized harmonic oscillator. With these definitions, the electric field (5.1) can be written as

$$\hat{E}(t) = \hat{X}^{\phi}(t)\sin(\omega t) - \hat{Y}^{\phi}(t)\cos(\omega t). \tag{5.4}$$

Using the commutator relation for $\hat{a}^{\dagger}(t)$ and $\hat{a}(t)$ it is straight forward to show that the commutator for the quadrature operators is given by

$$\left[\hat{X}^{\phi}(t), \hat{Y}^{\phi}(t)\right] = 2i. \tag{5.5}$$

This shows, that $\hat{X}^{\phi}(t)$ and $\hat{Y}^{\phi}(t)$ form a pair of conjugate operators. Due to Heisenberg's inequality[1]

$$\Delta^2\hat{X}^{\phi}(t)\Delta^2\hat{Y}^{\phi}(t) \geq 1, \tag{5.6}$$

[1] For a pair of Hermitian operators $\hat{A}$ and $\hat{B}$ the general form of Heisenberg's inequality is $\Delta^2\hat{A}\Delta^2\hat{B} \geq \frac{1}{4}\left|[\hat{A}, \hat{B}]\right|^2$.

$\hat{X}^{\phi}(t)$ and $\hat{Y}^{\phi}(t)$ cannot be simultaneously prepared with infinite accuracy. In Eqn. (5.6), $\Delta^2\hat{X}^{\phi}(t) = \langle\hat{X}^{\phi}(t)^2\rangle - \langle\hat{X}^{\phi}(t)\rangle^2$ is the variance of $\hat{X}^{\phi}(t)$ and $\langle\ldots\rangle$ denotes the expectation value for a given quantum state. Quantum states for which Eqn. (5.6) equals one are called minimum uncertainty states. Notable examples of such states are, for instance, the vacuum state $|0\rangle$ and the coherent state $|\alpha\rangle$. The latter is obtained by applying the displacement operator

$$D(\alpha) = \exp(-\frac{1}{2}|\alpha|^2)\sum_n \frac{(\alpha\hat{a}^{\dagger})^n}{n!} \tag{5.7}$$

on the vacuum state, where α is the amplitude of the coherent state. The uncertainty measured for any phase ϕ of the coherent state is always identical and equal to one, i.e. $\Delta^2\hat{X}^{\phi}(t) = \Delta^2\hat{Y}^{\phi}(t) = 1$. A state for which $\Delta^2\hat{X}^{\phi}(t) < 1 < \Delta^2\hat{Y}^{\phi}(t)$ is called a squeezed state, which is obtained by applying the one mode squeezing operator [54]

$$\hat{S}(r,\theta) = e^{\frac{r}{2}(e^{-i\theta}\hat{a}^2 - e^{i\theta}\hat{a}^{\dagger 2})} \tag{5.8}$$

on the coherent state $|\alpha\rangle$. θ is the squeezing angle in the phase-space quadrature plane and r is the squeezing parameter determining the degree of squeezing. In contrast to the coherent state, which after losses remains a minimum uncertainty state (just with smaller amplitude), a pure squeezed state transforms into a mixed state with smaller amplitude.

5.3 Squeezed Vacuum Light Field

A sketch of the experimental setup including an illustration of the quadrature squeezed light source, the LR-SPP sample, and the characterization stage is shown in Fig. 5.1. The experimental strategy is as following. First, the squeezed light source is characterized. This is done by removing the LR-SPP sample from the setup and directly performing a measurement on the output of the squeezed light source. Second, the LR-SPP sample is placed back into the setup and a LR-SPP mode is excited by the squeezed light source. The re-emitted quantum state will then be measured by the same characterization technique as used before to ensure similar experimental conditions.

These measurements are followed by a detailed analysis of the individual quantum states.

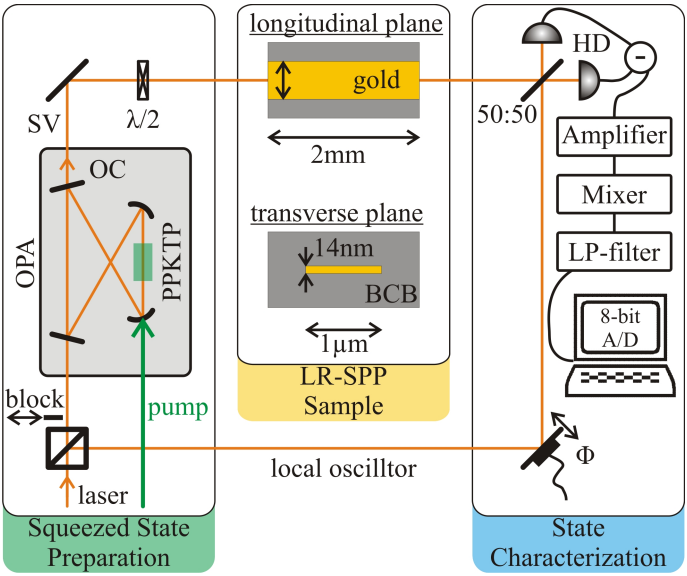

Figure 5.1: Sketch of the experimental setup for LR-SPP excitation with vacuum squeezed light: OPA - optical parametric amplifier, PPKTP - periodically poled KTP crystal, OC - output coupler, SV - squeezed vacuum, $\lambda/2$ - half-wave plate, Φ - piezo actuated mirror for phase variation, 50:50 - symmetric beam splitter, and HD - homodyne detection scheme.

The squeezed light field was produced by an optical parametric oscillator (OPO) operating below threshold. OPOs operating below threshold are commonly referred to as optical parametric amplifiers (OPAs). As illustrated in Fig. 5.1, the OPA cavity is composed of four mirrors in a bow-tie configuration. Two mirrors are concave with a radius of curvature of 25 mm and high-reflection coating at the fundamental wavelength of 1064 nm. The other two mirrors are plane, one of which is high reflection coated. The second plane mirror, which is called the output coupler (OC), has a power transmissivity of 10%.

The two curved mirrors are separated by ≈ 31 mm and the total optical round trip path length is ≈ 275 mm, resulting in a beam waist of 19 μm in between the two curved mirrors. At the center of this beam waist a periodically poled potassium titanyl phosphate (PPKTP) crystal with dimensions of $10 \times 2 \times 1\,\mathrm{mm}^3$ was placed for parametric down-conversion. Down-conversion to the fundamental cavity mode was achieved by pumping the PPKTP crystal with the second harmonic field at 532 nm, as shown in Fig. 5.1. The cavity beam waist was chosen appropriately to satisfy the Boy-Kleinman condition for the PPKTP crystal length [55]. Further details of the OPA design and its operation principle are summarized in Appendix A. For characterizing the squeezed light field, the OPA output mode

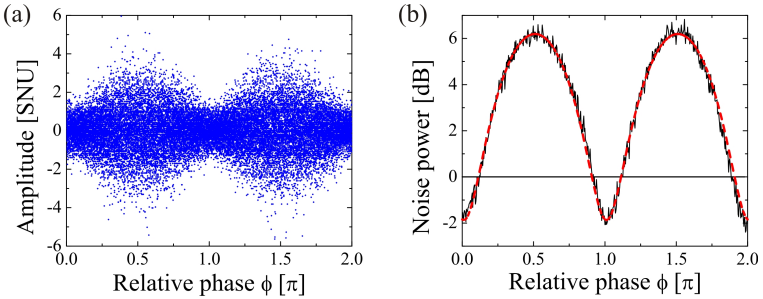

Figure 5.2: Time domain data in shot noise units (SNU) (a) and variance (b) of the squeezed vacuum mode: (a) The data contains approximately $0.5M$ data points linearly distributed over a phase variation between the signal mode and the LO from 0 to 2π. (b) Noise power relative to the shot noise level calculated either from (a) (black line) or from the density matrix $\hat{\rho}_{in}$ (red dashed line).

was matched to the mode of a bright local oscillator (LO) emerging from the same laser on a 50 : 50 beam splitter (BS). The contrast $C = (I_{\max} - I_{\min}) / (I_{\max} + I_{\min})$ on the BS between the OPA mode and the LO was measured to be 88.5%. After setting the LO power to 14 mW, the two output modes of the BS were then recorded by two analogue detectors, subtracted, amplified by 50 dB, down-mixed at an optical side band frequency of 4.7 MHz, again amplified by 30

dB, and finally low pass filtered with $f_{3\mathrm{dB}} = 150$ kHz. The resulting signal was then recorded by a oscilloscope[2] with a time resolution of 0.4 μs. In Fig. 5.2 (a) the resulting time domain data of the squeezed vacuum input state containing approximately 0.5 million data points is presented in shot noise units (SNU) for a variation of the relative phase between the LO and the signal mode from 0 to 2π. The shot noise unit is given by the fluctuation of the vacuum mode, which was recorded independently by blocking the OPA mode with the before mentioned LO power. The noise power with respect to the shot noise level (and therefore the squeezing and anti-squeezing) of the input state can be directly calculated from the time domain data and is shown by the black trace in Fig. 5.2 (b). Each data point of the variance is calculated for a time interval of 0.4 ms, thus considering ≈ 1000 quadrature data points. From this trace, the amount of squeezing and anti-squeezing of the input state are found to be -1.9 ± 0.1 dB and 6.1 ± 0.1 dB with respect to the shot noise level, respectively.

After this, the data has been further analyzed by applying the maximum likelihood algorithm to the data in order to reconstruct the states density matrix $\hat{\rho}_{\mathrm{in}}$ in the Fock-state representation. For this, no additional binning has been applied to the rough data. Each data point represents exactly one projective quadrature measurement. The method of reconstructing the states density matrix using the maximum likelihood method is described in detail in Appendix B. Fig. 5.3 (a) shows the absolute values of the reconstructed density

[2] LeCroy Waverunner LT374L with 8bit resolution.

matrix

$$\hat{\rho}_{\text{in}} = \begin{pmatrix} 0.70 & 0 & -0.2 & 0 & 0.07 & 0 & -0.03 \\ 0 & 0.12 & 0 & -0.06 & 0 & 0.03 & 0 \\ -0.2 & 0 & 0.09 & 0 & -0.05 & 0 & 0.02 \\ 0 & -0.06 & 0 & 0.04 & 0 & -0.02 & 0 \\ 0.07 & 0 & -0.05 & 0 & 0.03 & 0 & -0.01 \\ 0 & 0.03 & 0 & -0.02 & 0 & 0.01 & 0 \\ -0.03 & 0 & 0.02 & 0 & -0.01 & 0 & 0.01 \end{pmatrix} + i \begin{pmatrix} 0 & 0 & 0.01 & 0 & -0.01 & 0 & 0 \\ 0 & 0 & 0 & 0.01 & 0 & 0 & 0 \\ -0.01 & 0 & 0 & 0 & 0 & 0 & 0 \\ 0 & -0.01 & 0 & 0 & 0 & 0 & 0 \\ 0.01 & 0 & 0 & 0 & 0 & 0 & 0 \\ 0 & 0 & 0 & 0 & 0 & 0 & 0 \\ 0 & 0 & 0 & 0 & 0 & 0 & 0 \end{pmatrix}. \quad (5.9)$$

From the density matrix $\hat{\rho}_{\text{in}}$ the variance of the input state can be calculated for each quadrature $\hat{X}^{\phi}$ via

$$\Delta^2 \hat{X}^{\phi} = Tr\{\hat{X}^2 \hat{\rho}_{in}\} - Tr\{\hat{X}\hat{\rho}_{in}\}^2, \quad (5.10)$$

which is shown by the red dashed line in Fig. 5.2 (b). Another

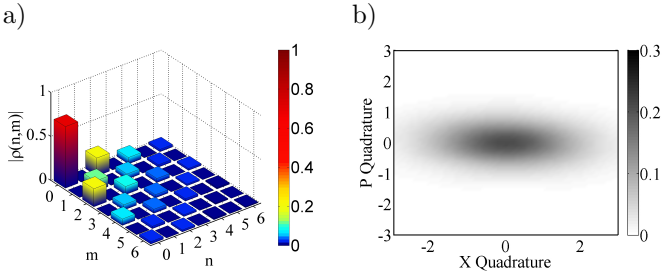

Figure 5.3: Absolute values of the reconstructed density matrix $\hat{\rho}_{in}$ (a) and Wigner-function (b) of the input state.

way of illustrating a quantum state is given by the Wigner-function $W(X, Y)$, where $X = \langle \hat{X}^{\phi=0} \rangle$, $(Y = \langle \hat{Y}^{\phi=0} \rangle)$ are the amplitude

(phase) of the light field. The Wigner-function $W(X,Y)$ is a so-called quasi probability distribution because it can be negative for some quantum states, e.g. for the single photon state $|1\rangle$. $W(X,Y)$ can be calculated directly from the density matrix $\hat{\rho}$ via

$$W(X,Y) = \frac{1}{\pi\hbar}\int_{-\infty}^{+\infty} \langle X + \frac{Q}{2}|\,\hat{\rho}\,|Y - \frac{Q}{2}\rangle\, dQ. \qquad (5.11)$$

Fig. 5.3 (b) shows a surface plot of the Wigner-function $W(X,Y)_{\text{in}}$ of the input state $\hat{\rho}_{\text{in}}$ calculated via Eqn. (5.11).

An alternative approach of analyzing the results would have been to reconstruct $W(X,Y)$ by applying the inverse Radon transformation directly on the time domain data and reconstructing $\hat{\rho}$ from $W(X,Y)$, as described in Ref. [56]. However, the result of that approach might yield artifacts in the Wigner-function as well as negative diagonal elements in $\hat{\rho}$, which are clearly un-physical.

5.4 Squeezed Surface Plasmons

After characterizing the input state, the LR-SPP sample has been inserted into the setup and the OPA mode was carefully aligned to a gold stripe with a width, height, and length of 2 μm , 14 nm, and 2 mm, respectively, exactly following the description in section 3.2. A transmission through the sample of 32.5% was measured for this gold strip. The overlap between the re-emitted LR-SPP mode and the LO mode on the 50 : 50 BS was measured to be 90.1% and is therefore comparable to the previous measurement of the input squeezed state. The recorded time domain data of the squeezed LR-SPP mode as well as the noise power relative to the shot noise level are presented in Fig. 5.4 (a) and (b), respectively. Identical settings as for the squeezed vacuum state were used for the acquisition system. In Fig. 5.5 (a) and (b) the absolute values of the density matrix

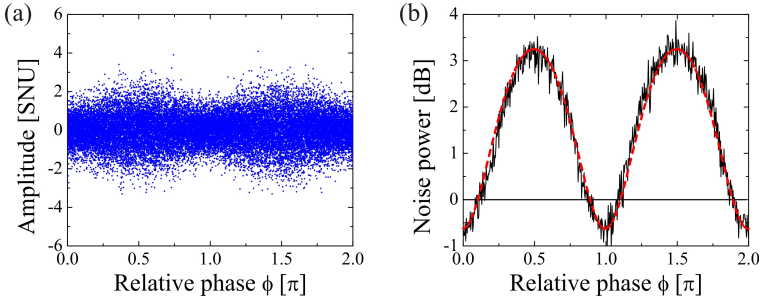

Figure 5.4: Time domain data (a) and variance (b) of the LR-SPP mode: (a) The data contains approximately $0.5M$ data points linearly distributed over a phase variation between the signal mode and the LO from 0 to 2π. (b) Noise power relative to the shot noise level calculated either from (a) (black line) or from the density matrix $\hat{\rho}_{LR-SPP}$ (red dashed line).

$$\hat{\rho}_{LR-SPP} = \begin{pmatrix} 0.84 & 0 & -0.13 & 0 & 0.02 & 0.00 & -0.01 \\ 0 & 0.09 & 0 & -0.03 & 0 & 0.01 & 0 \\ -0.13 & 0 & 0.05 & 0 & -0.01 & 0 & 0 \\ 0 & -0.03 & 0 & 0.01 & 0 & 0 & 0 \\ 0.02 & 0 & -0.01 & 0 & 0 & 0 & 0 \\ 0 & 0.01 & 0 & 0 & 0 & 0 & 0 \\ -0.01 & 0 & 0 & 0 & 0 & 0 & 0 \end{pmatrix} \tag{5.12}$$

and the corresponding Wigner-function $W(X,Y)_{\text{LR-SPP}}$ of the LR-SPP mode are shown. The amount of squeezing and anti-squeezing in the re-emitted light field is therefore measured to be -0.7 ± 0.1 dB and 3.2 ± 0.1 dB relative to the shot noise level, respectively. Therefore, it can be concluded that the retrieved state is squeezed and that the squeezing survived the plasmonic propagation.

5.5 Modeling the Surface Plasmon Mode

Next, it will be investigated whether the operation, that transforms the density matrix of the input state $\hat{\rho}_{\text{in}}$ to that of the output state

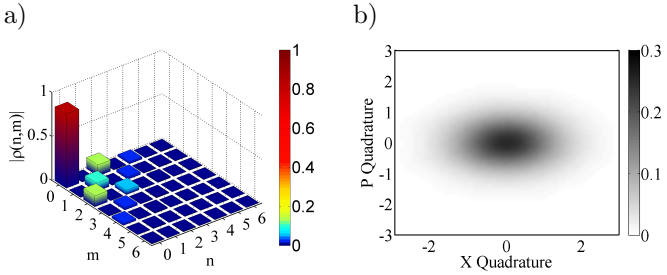

Figure 5.5: Absolute values of the reconstructed density matrix $\hat{\rho}_{\text{LR-SPP}}$ (a) and Wigner-function (b) of the LR-SPP mode.

$\hat{\rho}_{\text{LR-SPP}}$ can be described by the unitary beam splitter operator

$$\hat{U}_{\text{BS}} = e^{\frac{\theta}{2}(\hat{a}^\dagger \hat{b} e^{i\Phi} - \hat{a}\hat{b}^\dagger e^{-i\Phi})}. \tag{5.13}$$

Here, $\hat{a}$ and $\hat{b}$ are the field operators of the beam splitter input modes, Φ is the relative phase between the modes $\hat{a}$ and $\hat{b}$, and θ is linked to the transmission η via $\eta = cos^2(\frac{\theta}{2})$. The expected output state is thus

$$\hat{\rho}_{\text{out}}(\eta) = Tr\{\hat{U}_{\text{BS}}(\eta)\hat{\rho}_{\text{in}} \otimes |0\rangle\langle 0| \hat{U}^\dagger_{\text{BS}}(\eta)\}, \tag{5.14}$$

where the second beam splitter input mode was assumed to be a vacuum mode with $\hat{\rho}_{\text{vac}} = |0\rangle\langle 0|$ and the trace is taken over one of the output modes of the beam splitter. To see whether $\hat{\rho}_{\text{out}}(\eta)$ is similar to the actually measured output state $\hat{\rho}_{\text{LR-SPP}}$ the fidelity $F(\eta)$ between the two states has been computed. Following the description of Ref. [57], the fidelity is given by

$$F(\eta) = Tr\{\sqrt{\hat{\rho}_{\text{out}}(\eta)}\hat{\rho}_{\text{LR-SPP}}\sqrt{\hat{\rho}_{\text{out}}(\eta)}\}^{1/2}, \tag{5.15}$$

with $0 \leq F(\eta) \leq 1$ and $F(\eta) = 1$ if and only if $\hat{\rho}_{\text{out}}(\eta) = \hat{\rho}_{\text{LR-SPP}}$. In Fig. 5.6, the fidelity F is plotted as a function of the beam splitting ration η. In the extreme cases, a value of $\eta = 0$ corresponds to the overlap between $\hat{\rho}_{\text{LR-SPP}}$ and the vacuum state $\hat{\rho}_{\text{vac}}$ and a value of $\eta = 1$ corresponds to the overlap between $\hat{\rho}_{\text{LR-SPP}}$ and the incident squeezed vacuum state $\hat{\rho}_{\text{in}}$. With respect to η, a maximum fidelity

of $F = 0.993$ for $\eta = 0.33$ was found, as shown in Fig. 5.6. This value of η coincides with the value obtained in the classical transmission measurement shown in Fig. 3.3 (a), thus strongly indicating that the plasmonic decoherence can be solely simulated by a beam splitter interaction. For visualizing the similarity between $\hat{\rho}_{LR-SPP}$ and $\hat{\rho}_{\text{out}}(\eta = 0.33)$, their real and imaginary parts are presented in Fig. 5.7. Note that for both $\hat{\rho}_{\text{LR-SPP}}$ and $\hat{\rho}_{\text{out}}(\eta = 0.33)$ the imaginary elements are close to zero.

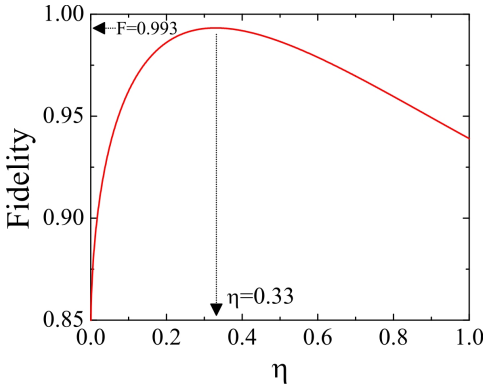

Figure 5.6: Fidelity F between the modeled output state $\hat{\rho}_\eta$ and the LR-SPP state $\rho_{\text{LR-SPP}}$ as a function of the transmission through a beam splitter η.

5.6 Interpretation and Conclusion

In the following the experimental results are justified by using theoretical arguments. The propagation of plasmons can be considered as photonic excitations of the electric field that are mapped onto the (quasiparticle) excitations of the polarizable medium. One can split the electrical polarization $\hat{P}$ of the medium into positive and negative frequency components, $\hat{P} = \hat{P}^+ + \hat{P}^-$, and expand the positive part

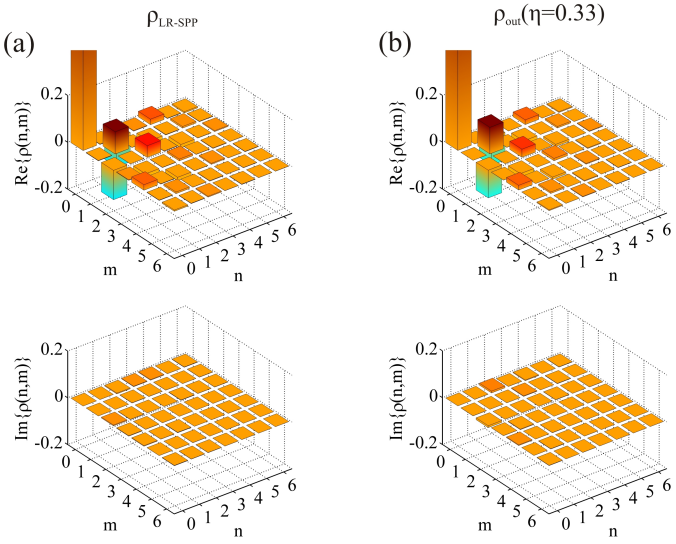

Figure 5.7: Illustration of the measured LR-SPP density matrix $\rho_{\text{LR-SPP}}$ (a) and the modeled output density matrix $\rho_{\text{out}}(\eta = 33\%)$ (b). Shown the real (top) and imaginary (bottom) parts of the density matrices.

$\hat{P}^{+}$ in terms of the electric field, $\hat{E} = \hat{E}^{+} + \hat{E}^{-}$;

$$\hat{P}^{(+)} = \sum_{m=0}^{\infty} \sum_{n=0}^{\infty} \hat{c}_{mn}(\{\hat{O}_i\}) \left(\hat{E}^{(-)}\right)^{m} \left(\hat{E}^{(+)}\right)^{n}, \tag{5.16}$$

where the possibility is included that the expansion coefficient $\hat{c}_{mn}$ may depend on a set of state operators $\{\hat{O}_i\}$ describing the state of the polarizable medium, e.g. phonon operators or temperature. The expansion coefficient $c_{mn}(\{\hat{O}_i\})$ thus gives access to information about the nature of the excitation of the medium and, e.g., quasi particle interactions. The experiment was performed in the low intensity limit, in which case the polarization reduces to

$$P^{(+)} = \hat{c}_{00}(\{\hat{O}_i\}) + \hat{c}_{01}(\{\hat{O}_i\})\hat{E}^{(+)}, \tag{5.17}$$

where the $\hat{E}^{(-)}$ term was excluded since a negligible intensity is observed when the incoming field is in vacuum. This also means that $\langle \hat{c}_{00}^{\dagger} \hat{c}_{00} \rangle = 0$ must be required. Since the equation of motion of the electric field is linear, the expression for $\hat{P}^{(+)}$ means that the outgoing field $\hat{E}_{\text{out}}^{(+)}$ can be written as a combination of two terms

$$\hat{E}_{\text{out}}^{(+)} = \hat{G}(\{\hat{O}_i\})\hat{c}_{00}(\{\hat{O}_i\}) + \hat{G}(\{\hat{O}_i\})\hat{E}_{\text{in}}^{(+)}, \tag{5.18}$$

where $\hat{G}(\{\hat{O}_i\})$ is the Greens function of the plasmonic propagation. If any dependence on internal state operators $\{\hat{O}_i\}$ is ignored in the expansion coefficient $\hat{c}_{00}$ and $\hat{c}_{01}$ in Eq. (5.16), one can find that the input/output relation for a single mode operator $\hat{a}$ is given by

$$\hat{a}_{\text{out}} = \sqrt{1-\eta}\hat{v} + \sqrt{\eta}\hat{a}_{\text{in}}, \tag{5.19}$$

where $\hat{v}$ is a combination of the $\hat{c}_{00}$ operators with the factor $\sqrt{1-\eta}$ separated out for convenience. Then from $\langle \hat{c}_{00}^{\dagger} \hat{c}_{00} \rangle = 0$ it immediately follows that $\langle \hat{v}^{\dagger} \hat{v} \rangle = 0$ and consistency of the commutation relations requires that $[\hat{v}, \hat{v}^{\dagger}] = 1$. $\hat{v}$ is thus a single mode vacuum operator in agreement with our experimental observation. The results therefore show that the classical description $P^{(+)} = \epsilon_0(\epsilon - 1)E^{(+)}$ (where the permittivity of the material ϵ is just a constant) remains valid for the metal down to the level of single photons if a vacuum contribution to the operator equations is added. This conclusion is consistent with the theoretical interpretation in Ref. [58] of the experiments in Ref. [19], where it is concluded that the polarization degrees of freedom leaves no "which-way" information in the solid. The present work extends that conclusion by showing that also the presence or absence of a photon leaves no "which-way" information. It should be noted, however, that even in the regime of linear optics a different behavior occurs if the polarizability depends on fluctuating parameters of the material. A notable example of this is the observation of Brillouin scattering in optical fibers [59].

6

Coupling Single Defects in Diamond to Surface Plasmon Polaritons

6.1 Introduction

Spurred by recent developments in the field of quantum computing and quantum information science, there has been a strong interest in exploring the coherent interaction between single quantum systems and photon fields. Such interactions could allow for long distance quantum communication [60] and scalable quantum computers [61]. The so-called strong coupling regime in quantum electrodynamics has been achieved for a number of physical systems like, for instance, Cooper pairs interacting with super-conducting cavities [62], single atoms in Fabry-Pérot cavity [63, 64], and between a single atom and the whispering-gallery mode of a micro-resonator [65]. All these approaches are rendered possible due to a reduction of the effective mode volume V_{eff} of the photons.

The experiment described in this chapter aims for the coupling between a nitrogen-vacancy color center in diamond to the plasmonic mode propagating along a nano-wire [13]. The coupling occurs, similar to the approaches mentioned above, due to a sub-wavelength confinement of the plasmon.

6.2 The Nitrogen-Vacancy Defect in Diamond

More than 100 different types of defects in diamond are known, among one of which is the nitrogen-vacancy center. Since its first discovery in the 1960s it has attracted the attention of the scientific community because of its unique properties.

The NV center is a single optical active level within the diamond band gap of 5.50 eV [66, 67]. One area of interest arises from its non-zero spin ground state. The ground state can be treated as a qubit and the optical transitions can be used for qubit manipulation and read out [68, 69, 70, 71], rendering the NV-center to a possible qubit candidate for quantum computing applications [72]. The NV-centers single photon emission renders this system to a broadband source, which might find applications in quantum cryptography [73, 74, 71, 75]. The NV center is a possible candidate for optically coupled quantum registers [70] and distributed quantum computation [76]. As it was shown recently, the proximal nuclear spins of adjacent atoms can be coherently controlled via hyperfine interaction [77]. This can be used as a basis for quantum memory with an extremely long coherence time [78].

The electronic structure of the NV-center has been reviewed in a number of articles, see for instance [79], and will just briefly be summarized here. A simplified model describes the NV-center as a substitutional nitrogen atom adjacent to a vacancy in the diamond lattice. At room temperature, one observes a strong optical transition with a zero phonon line (ZPL) at 637 nm (1.945 eV) accompanied by a vibronic band at higher energy in absorption and a lower energy in emission. Detailed analysis of the ZPL unveiled that the center has trigonal C_{3v} symmetry [80]. Electron parametric resonance on a point which was correlated with the NV-center showed trigonal symmetry with a spin polarized triplet state (S=1). This S=1 state implies an even number of electrons. Since the substitutional nitrogen atom has five valence electrons, the NV-center must have been charged in these measurements. Therefore, it was assumed that the NV center is negatively charged with an extra electron presumably donated by isolated substitutional nitrogen defects. From detection of the

NV center in the dark at 100K by electron parametric resonance researchers have concluded that the S=1 state is the ground state of the NV center [81]. Later on, this has been confirmed by hole burning measurements [82], optically detected magnetic resonance [83], and Raman heterodyne measurements [84].

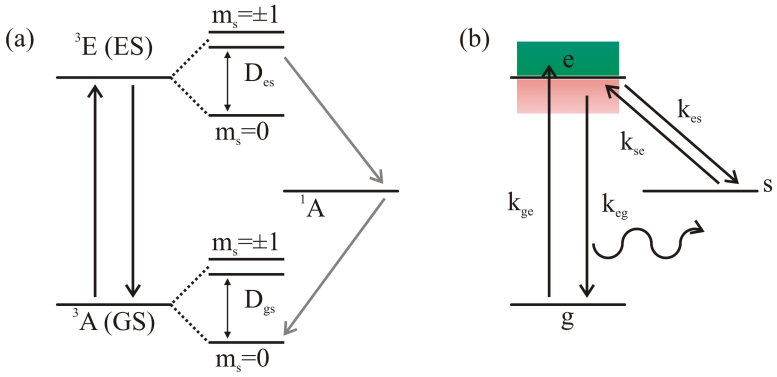

Figure 6.1: (a) Energy diagram of a NV defect. Both the GS ^3A and the ES 3^E are spin triplets, with a zero field splitting D_{gs} and D_{es} between the $m_S = 0$ and $m_S = \pm 1$ levels. Largely spin-conserving transitions are shown by the black arrows. The dominant non-radiative relaxations through ^1A (gray arrows) is not spin conserving. (b) Energy diagram model used as a basis for the rate-equations. Transitions from the shelving state 's' to the ground state 'g' are neglected.

The energy level diagram of the NV defect, as known up to now, is illustrated in Fig. 6.1 (a). The ground state (GS) splitting between the $m_s = 0$ singlet state and the $m_s = \pm 1$ doublet state was measured to be $D_{gs} = 2.88$ GHz. Only recently, the state structure of the excited state (ES) has been investigated experimentally, showing a zero-field splitting of $D_{es} = 1.43$ GHz [85, 86]. Optical transitions between the GS and the ES are primarily spin conserving, as illustrated by the black arrows in Fig. 6.1 (a) [79]. Only non-radiative transitions through an intersystem crossing to ^1A are not spin conserving, as

illustrated by the gray arrows in Fig. 6.1 (a). Under optical pumping, this allows for initialization into the $m_s = 0$ state [79]. Since the transition via the ^1A state is non-radiative, its presence only becomes evident by measuring the auto-correlation function of a single NV defect, as will be discussed in section 6.4.

Due to its high concentration in the atmosphere, nitrogen is present as an impurity with varying concentration in diamond. Diamonds are categorized in classes Ia to IIb, labeling different impurity concentrations. These different types of diamond are summarized in Table 6.1. In diamonds with a sufficiently high nitrogen concentration NV-centers can form naturally. If required, the NV-center concentration can be enhanced by irradiating the diamonds with focused electrons of 400keV or Ga^+ ions of 30keV, hereby creating vacancies in the diamond lattice. Subsequent annealing at 750°C in vacuum allows the vacancies to become mobile and form NV defects [87]. However, this method is only useful for creating clusters with a large number of NV defects. Another way of creating NV-

diamond type	dominating impurity
Ia	nitrogen aggregates with 100 to $<$ 1000 ppm
Ib	nitrogen $>$ 1 ppm
IIa	nitrogen $<$ 1 ppm
IIb	boron

Table 6.1: Different types of diamond and their dominating impurity.

centers is by nitrogen implantation and subsequent annealing of type IIa diamonds with an abundant nitrogen concentration of less than 1 ppm [88]. In these studies, the ^{15}N isotope has been employed in order to distinguish implanted from abundant ^{14}N nitrogen. The yield in these studies for single NV-center formation has been calculated to be 2.5%. Due to NV-center electron spin interaction with other spins and phonons in the diamond lattice, a single impurity spin will usually lose its phase quickly. Due to strong binding between low-mass carbon atoms, diamond owes phonon-limited spin lattice relaxation times around $10^2 - 10^4$ s. Thus, the phase coherence time of electron spins is limited by dipolar interactions with other spins, i.e. the

nuclear spin bath arising from the presence of ^{13}C atoms. The most abundant isotope ^{12}C (98.9%) is spin free. By preparing NV-centers in ultra-pure isotopically purified ^{12}C CVD diamond, an electron spin phase coherence time of more than 1 ms has been measured [89].
For this work, nano-crystal diamonds MSY 0-0.05 Mikron GAF from Microdiamant AG were used. These diamonds have a mean diameter of ≈ 30 nm and a maximum size of ≈ 50 nm. In approximately 1% of the nano-crystals single NV defects can be found [90].

6.3 The Experimental Setup

The experimental setup used for the studies on single NV-centers as well as NV-centers coupled to plasmonic nano-structures is illustrated in Fig. 6.2. The samples were illuminated by either a continuous wave laser[1] or a pulsed laser[2] with 8 ps pulse width and variable repetition rate ranging from 1 MHz up to 20 MHz. Both lasers are operating at a vacuum wavelength of 532 nm. For focusing the pump light to a near diffraction limited spot on the sample, a standard microscope objective[3] with a numerical aperture (NA) of 0.95 and a focal length of $f = 2$ mm was used. For some of the measurements, an oil immersion lens with a $NA = 1.4$ and $f = 2$ mm was alternatively employed. A piezo-actuated stage[4], on which the objective was mounted, was used to controllably scan the pump laser spot across the sample surface. The fluorescence light from the sample was collected with the same objective and split on a 50 : 50 beam splitter, as illustrated by the red lines in Fig. 6.2 (a). The beam splitter output modes were imaged on a pinhole for selecting a diffraction limited spot from the probe, before being spectrally filtered and detected by avalanche photo diodes[5] (APDs). Though not specified by the manufacturers data sheet, the timing resolution of the APDs is expected to be ≈ 300 ps [91]. The spectral filters were composed of a 532 nm notch-filter and two long pass filters with cut-offs at 600 nm and 650 nm for

[1] Coherent Compass 215M-75 SL
[2] Fianium FP532-PP-01
[3] Olympus MPLAPO 100X/0.95
[4] MCL Nano-T225 with $200 \times 200 \times 50\,\mu\text{m}^3$ scanning range
[5] Perkin Elmer SPCM-AQRH-14-FC

suppressing reflected pump light and Raman scattered photons. One of the beam splitter output modes first passed through a confocal lens configuration, before being projected on the pinhole via passing a x-y galvanometric mirror[6]. The galvanometric mirror scanned the image plane formed in between the pair of confocal lenses (1st image plane in Fig. 6.2 (a)), thereby enabling a scan of the sample around the point of excitation within the objectives field of view. In the same detection channel behind the pinhole, a flip mirror allowed us to switch between detection with an APD or a grating spectrometer[7], as illustrated in Fig. 6.2 (a). A time to amplitude converter[8] (TAC) was used to witness the emission of single photons and to measure the lifetime of NV-defects. These measurements are described in detail in the following section. In Fig. 6.2 (b), a typical fluorescence image of a single NV-center is shown, obtained by detecting the APD signal while scanning the objective (hence the pump laser with a power of 544 μW) across the position of the defect. In this case, the sample has been prepared by spin-coating a water solution containing 10 carat nano-diamonds and 0.5 w% polyvinyl acetate (PVA) on a quartz substrate with 5000 rpm for 10 seconds. Prior to the deposition, the substrate was cleaned in a plasma asher to remove residual organic dirt and to render the substrates surface hydrophilic. Cleaning the substrate in the plasma asher showed to be an important step in the sample preparation. In case this cleaning step was left out the sample surface was hydrophobic and almost no nano-diamonds were deposited on the sample.
The spectrum of this NV defect, which is shown in Fig. 6.3 (a), is marked by its characteristic ZPL at 637nm and a red shifted phonon broadened emission peak.

6.4 Single Photon Emission from a Single NV Defect

One can describe the population dynamics of the NV-center with a rate equation of a three level system, which for this system was first

[6]Cambridge Technology 6240H
[7]Andor Shamrock SR-500 with Andor DU970N electron multiplying CCD
[8]PicoHarp 300

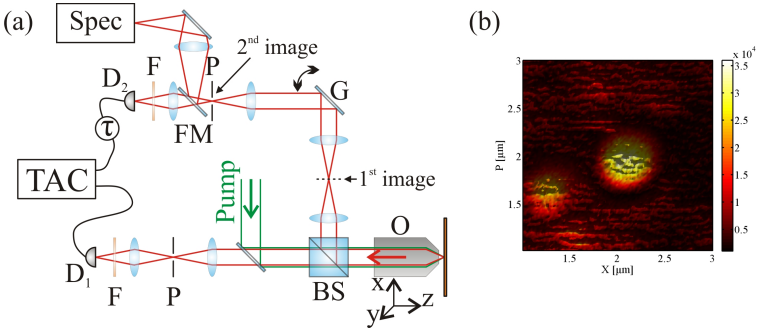

Figure 6.2: (a) Schematic diagram of the home-build confocal microscope: O - objective, BS - 50 : 50 beam splitter, P - pinhole, F - fluorescence filter, $D_{1,2}$ - avalanche photo diode, G - galvanometric mirror, FM - flip mirror, TAC - time to amplitude converter, and Spec - grating spectrometer. (b) Fluorescence image of a single NV-defect.

applied by Kurtsiefer et al. in 2000 [74]. The energy level labeling and the different rates are illustrated in Fig. 6.1 (b). When neglecting all coherences, the population dynamics of the ground (g), the excited (e), and the shelving state (s) are governed by

$$\begin{pmatrix} \dot{\rho}_\mathrm{g} \\ \dot{\rho}_\mathrm{e} \\ \dot{\rho}_\mathrm{s} \end{pmatrix} = \begin{pmatrix} -k_\mathrm{ge} & k_\mathrm{eg} & 0 \\ k_\mathrm{ge} & -k_\mathrm{eg} - k_\mathrm{es} & k_\mathrm{se} \\ 0 & k_\mathrm{es} & -k_\mathrm{se} \end{pmatrix} \begin{pmatrix} \rho_\mathrm{g} \\ \rho_\mathrm{e} \\ \rho_\mathrm{s} \end{pmatrix}, \tag{6.1}$$

where ρ_i, $i = \{\mathrm{g}, \mathrm{e}, \mathrm{s}\}$, is the population probability of state i and $\rho_\mathrm{g} + \rho_\mathrm{e} + \rho_\mathrm{s} = 1$. In this model, possible non-radiative transitions from the shelving state to the ground state are neglected because they are about three orders of magnitude smaller than all other rates [74]. The emission rate of a photon R is proportional to the population of the excited state ρ_e, which in the steady state regime ($\dot{\rho}_\mathrm{g} = \dot{\rho}_\mathrm{e} = \dot{\rho}_\mathrm{s} = 0$) can be written as

$$\rho_\mathrm{e}(t \to \infty) = \frac{k_\mathrm{se} k_\mathrm{ge}}{k_\mathrm{ge} k_\mathrm{es} + k_\mathrm{ge} k_\mathrm{se} + k_\mathrm{eg} k_\mathrm{se}}. \tag{6.2}$$

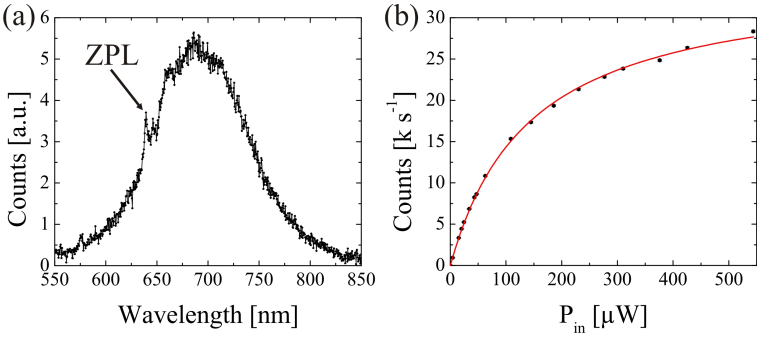

Figure 6.3: (a) Spectrum of a single NV-center. (b) Count-rate of the same NV defect as a function of pump power.

This population shows a saturation behavior as a function of the pump rate k_{ge}. The measured emission rate of the NV defect from Fig. 6.2 (b) as a function of pump power is shown in Fig. 6.3 (b), recorded with APD D_1. The count rate $R(P_{\mathrm{in}})$ follows a function $R(P_{\mathrm{in}}) = R_\infty \frac{P_{\mathrm{in}}/P_{\mathrm{sat}}}{1+P_{\mathrm{in}}/P_{\mathrm{sat}}}$, where R_∞ is the rate for $P_{\mathrm{in}} \to \infty$ and P_{sat} is the saturation pump power defined as $R(P_{\mathrm{sat}}) = R_\infty/2$. From the fit in Fig. 6.3 (b), the coefficients have been determined to be $R_\infty = 35k\,\mathrm{s}^{-1}$ and $P_{\mathrm{sat}} = 144\,\mu\mathrm{W}$.
The emission of a single photon from a single NV-center is witnessed by measuring the second order correlation function $g^{(2)}(\tau)$ in a Hanbury Brown and Twiss (HBT) measurement setup [92, 93]. A HBT measurement setup is composed of a beam splitter (BS) and two APDs D_1 and D_2 detecting single photons at arrival times $t_1 = t$ and $t_2 = t + \tau$, as shown in Fig. 6.2 (a). $g^{(2)}(\tau)$ is defined as

$$g^{(2)}(\tau) = \frac{\langle i_1(t) i_2(t+\tau)\rangle}{\langle i_1(t)\rangle \langle i_2(t+\tau)\rangle}, \tag{6.3}$$

where $i_1(t+\tau)$ and $i_2(t)$ are the photon counts of the detectors D_1 and D_2, respectively, and $\langle \ldots \rangle$ denotes averaging over time t. This equation can be understood by considering that a single photon emitted by a NV-center can either be transmitted or reflected on the BS. In a particle picture, energy conservation requires that the detection

of a single photon occurs either by detector D_1 or detector D_2. Practically, $g^{(2)}(\tau)$ is measured by accumulating histograms using a time to amplitude converter (TAC), as shown in Fig. 6.2 (a), where the APD signal D_1 was used as the start trigger and the APD signal D_2 as the stop trigger of the TAC. In order to acquire negative times, the signal of D_2 was delayed by a 260 ns cable delay line. The time resolution of the TAC, which defines the time averaging in Eqn. (6.3), was set to 64 ps for all measurements. Thus, in case of a single photon emission no coincidences $\langle i_1(t)i_2(t+\tau)\rangle$ are measured for $\tau = 0$. Finally, $g^{(2)}$ was normalized such that $g^{(2)}(\tau = \infty) = 1$. Note, that for an N-photon Fock state $g^{(2)}(0)_N = 1 - 1/N$ [93]. Hence, the condition $g^{(2)}(0) < 0.5$ is sufficient to prove that the emitted light is prepared in the single photon state.
In order to derive an analytic expression for $g^{(2)}(\tau)$ of an NV-center, one first has to solve the rate equation (6.1), where the system is initially prepared in the ground state, i.e. $\rho_{\mathrm{g}}(t = 0) = 1, \rho_{\mathrm{e}}(t = 0) = \rho_{\mathrm{s}}(t = 0) = 0$. Then, $g^{(2)}(\tau)$ is obtained by normalizing $\rho_{\mathrm{e}}(\tau)$ to $\rho_{\mathrm{e}}(\tau = \infty)$ [74, 93], giving the result

$$g^{(2)}(\tau) = \frac{\rho_{\mathrm{e}}(\tau)}{\rho_{\mathrm{e}}(\tau = \infty)} = 1 + C_2 e^{-|\tau|/\tau_2} + C_3 e^{-|\tau|/\tau_3}, \tag{6.4}$$

with the decay rates and coefficients given by

$$\begin{aligned} 1/\tau_{2,3} &= A/2 \pm \sqrt{(A/2)^2 - B}, \\ C_2 &= \frac{1 - \tau_2 k_{\mathrm{se}}}{k_{\mathrm{se}}(\tau_2 - \tau_3)},\ C_3 = -1 - C_2, \end{aligned} \tag{6.5}$$

with

$$\begin{aligned} A &= k_{\mathrm{ge}} + k_{\mathrm{eg}} + k_{\mathrm{se}} + k_{\mathrm{es}}, \quad \text{and} \\ B &= k_{\mathrm{ge}}k_{\mathrm{es}} + k_{\mathrm{ge}}k_{\mathrm{se}} + k_{\mathrm{eg}}k_{\mathrm{se}}. \end{aligned} \tag{6.6}$$

In Fig. 6.4 the measured and modeled (using Eqn. (6.4)) second order correlation function $g^{(2)}(\tau)$ are plotted for a pump power of 80 μW (a) and 576 μW (b), respectively. On a short time scale around $\tau = 0$, the auto-correlation function $g^{(2)}(\tau) < 0.5$. Hence, only a single photon is emitted from the NV defect within the time window where $g^{(2)}(0) < 0.5$. Generally, this behavior is referred to as photon

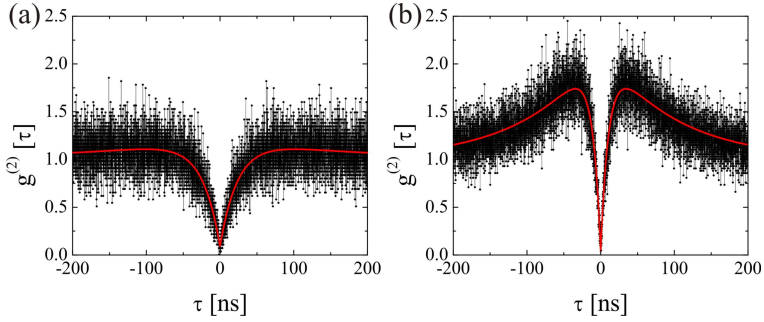

Figure 6.4: Measured (black dots) and fitted (red line) second order correlation function $g^{(2)}(\tau)$ of a single NV-center with a pump power of (a) 80 μW and (b) 576 μW.

anti-bunching. On a slightly longer time scale, the light field emitted by the NV emitter bears photon bunching properties, as $g^{(2)}(\tau) > 1$. This behavior is in contrast to a pure two level system and due to the presence of the thermally coupled shelving state. As can be seen from Fig. 6.4, the photon bunching only becomes clearly measurable for higher excitation powers.

It is important to note that the radiative decay time of NV defects depend on the refractive index n of the surrounding medium as $1/n$ [94, 95]. In comparison to bulk diamond, which has a refractive index of $n_{\text{diamond}} = 2.4$ and an excited state lifetime of 11.6 ns [96], the lifetime of NV-defects in nano-crystals is expected to be higher. This is due to the fact that nano-crystals are surrounded by air ($n = 1$) on one side and attached to the glass substrate ($n \approx 1.5$) on the other side. Furthermore, the NV-defect might be located at any position within the nano-crystal, i.e. either in the crystal center or more close to the crystal surface. Since that position is not known and since the orientation of nano-crystals on the sample surface is random, the refractive index that the NV defect effectively feels is expected to follow a broad distribution. As a consequence of this, the radiative decay time of NV-centers in nano-crystal diamonds is expected to be broadened, too. Fig. 6.5 (a) shows the distribution of

NV-center life-times in diamond nano-crystals, where the decay time of a total of 31 NV defects has been measured. These measurements were performed as follows. Single NV-centers were excited using the pulsed laser with a repetition rate of 5 MHz. Using the TAC with a time resolution of 64 ps, the laser trigger is start signal, and APD counts from D_2 as stop signal, lifetime histograms were obtained. Such a lifetime histogram is shown in Fig. 6.5 (b). An exponential fit to the data then yields the lifetime of the NV-defect under investigation. Due to possible contamination of the sample, some of the

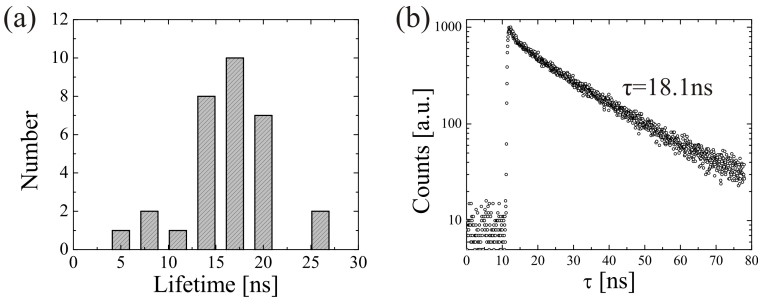

Figure 6.5: (a) Lifetime distribution of single NV defects in diamond nano-crystals. (b) Example lifetime measurement obtained under pulsed excitation.

centers have a lifetime which is shorter than the one measured in bulk diamond. However, the majority of defects decay noticeably slower with a peak value around 17 ns.

6.5 Single Surface Plasmon Excitation

The aim of the experiment described in this section is to control the coupling of a single NV defect to a metallic nano-structures, thereby increasing the decay rate into the plasmon mode while simultaneously decreasing the relative rate into all other modes. In general, coupling an emitter to a resonant mode will ultimately change the life-time of the excited state of the emitter. This effect has first

been addressed by Edward M. Purcell in 1946 [97], and is known as the Purcell effect. In other words, it means that the emission properties of quantum emitters such as atoms, molecules, quantum dots, or NV centers do not only depend on their intrinsic properties, but also on the local electromagnetic environment. This is somewhat similar to the dependence of the lifetime on the refractive index of the medium surrounding the emitter, as has been already mentioned in the previous section. Modifications of the emission lifetime, spectral distribution, and spatial emission pattern have been demonstrated near planar interfaces [98], through resonant coupling to optical micro-cavities [99, 100, 101], and recently through coupling to metal nano-structures [102, 103, 104, 15, 105, 106, 17, 107, 90]. Most closely related to the work discussed in this section is the coupling of NV defects to silver nano-wires, which has been achieved only very recently [108]. Excitation of plasmon resonances in metallic nano-structures, which act as optical nano-antennas, leads to two kind of effects: First, highly localized photon fields are created that enhance the excitation rate. Second, the density of states of the final state is increased, that enhances both the radiative and non-radiative decay rates of nearby emitters. A key feature of the emitter-plasmon coupling is the reduction of the effective mode volume V_{eff} of photons, which in turn results in a substantial increase of the emitter-plasmon coupling constant $g \propto 1/\sqrt{V_{\text{eff}}}$.

6.5.1 Theory on Single Emitter Plasmon Coupling

The model illustrating the NV defect nano-wire system and the different decay channels are shown in Fig. 6.6. It should be noted that even though the focus of this section is on NV defects, the theoretical description is quite general and thus also describes the coupling of various other emitters like, for instance, semiconductor quantum dots or CdSe nano-crystals. In the experiment, the NV defect is positioned in a distance d away from the nano-wire center. The dipole moment $\mathbf{p}_0$ of the emitter should be aligned along along the radial direction r of the wire to obtain a maximum overlap to the electric field $\mathbf{E}_{pl}$ of the plasmonic mode, $\mathbf{E}_{\text{pl}} \cdot \mathbf{p}_0$. This becomes evident from the polarization of the fundamental mode, as discussed in section 2.3. The

total decay rate Γ_{tot} is composed of three decay channels. The first channel is the decay into non-radiative modes $\Gamma_{\text{non-rad}}$ due to photonic losses ($IM\{k_{\parallel}\}$) in the nano-wire. The second channel is the radiative mode Γ_{rad} corresponding to a coupling into free space. The third and most important channel is the decay into the surface plasmon mode Γ_{pl}. In the following, the decays into the different channels for realistic material parameters and dimensions will be discussed.

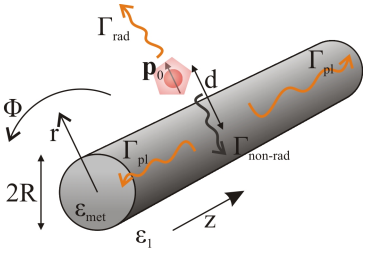

Figure 6.6: Model of a NV defect with dipole moment p_0 positioned in a distance d from the center of a nano-wire. The dipole moment should be aligned along the radial component r of the wire. Illustrated are the decay channels Γ_{rad}, $\Gamma_{\text{non-rad}}$, and Γ_{pl}.

Derivations of the decay rates $\Gamma_{\text{rad}}, \Gamma_{\text{non-rad}}$, and Γ_{pl} are based on classical calculations in the quasi-electrostatic limit, which were first presented in Ref. [13] for an emitter metal nano-wire system and further elaborated on in Ref. [14]. The spontaneous emission rate enhancement of a single emitter placed at a distance d from the center of a nano-wire with radius R is (Ref. [14])

$$\frac{\Gamma_{\text{rad}}}{\Gamma_0} = \left| 1 + \frac{\epsilon - 1}{\epsilon + 1} \frac{R^2}{d^2} \right|^2 , \tag{6.7}$$

where $\epsilon = \epsilon_{\text{met}}/\epsilon_1$ and Γ_0 is the emission rate of the emitter in a uniform dielectric ϵ_1. As the emitter approaches the nano-wire the decay into non-radiative modes $\Gamma_{\text{non-rad}}$ increase as

$$\frac{\Gamma_{\text{non-rad}}}{\Gamma_0} = \frac{3}{16 k_0^3 (d-R)^3} \text{Im}\left(\frac{\epsilon - 1}{\epsilon + 1} \right) . \tag{6.8}$$

$\Gamma_{\text{non-rad}}$ reflects the losses in the system being present due to a non-zero imaginary part of ϵ_{met}. As it can be seen, the non-radiative losses are diverging when the emitter approaches the wire surface as $1/(d-R)^3$. Thus, it is evident that losses into non-radiative modes directly influence the efficiency of the device. The decay rate into the fundamental (m=0) plasmon mode is given by

$$\frac{\Gamma_{\text{pl}}}{\Gamma_0} = \alpha_{\text{pl}} \frac{K_1^2(k_{1\perp} d)}{(k_0 R)^3}, \tag{6.9}$$

with the coefficients

$$\alpha_{\text{pl}} = \frac{3(\epsilon_1 - \epsilon_{\text{met}})}{\epsilon_1^{3/2}} \frac{C^2 I_1(C) I_0(C)}{d\chi(C)/dx} \quad \text{and} \tag{6.10}$$

$$\chi(x) = \epsilon_1 I_0(x) K_0'(x) - \epsilon_{\text{met}} K_0(x) I_0'(x). \tag{6.11}$$

In the nano-wire limit, i.e. when the wave vector $k_{\|}$ follow a $\propto 1/R$ dependence, the coefficient $C \approx k_{1\perp} R$. I_{j}, j $= \{0, 1\}$, and K_1 are modified Bessel functions of the first and second kind, respectively. As a function of emitter distance d, these equations describe the decay rates into the respective channels for a given wire radius R and dielectric constants ϵ_{met} and ϵ_1.

It is convenient to introduce the distance $d' = d - R$ from the wire surface to the emitter and to perform all calculations in this basis. For a realistic wire radius of $R = 25$ nm, the various decay rates are plotted as an example in Fig. 6.7 (a). It can be seen, when the emitter approaches the surface of the wire, all decay rates increase monotonically. In a wide range of d', Γ_{pl} is enhanced significantly compared to Γ_0 and the dominant decay channel of the emitter. Only close to the nano-wire surface the non-radiative rate dominates over all other decay channels. Therefore, in order to quantify the emitter coupling efficiency into the plasmon mode it is convenient to introduce a "Purcell factor"

$$P = \frac{\Gamma_{\text{pl}}}{\Gamma_{\text{rad}} + \Gamma_{\text{non-rad}}} \tag{6.12}$$

and the coupling efficiency to the plasmon mode

$$\eta_{\text{pl}} = \frac{\Gamma_{\text{pl}}}{\Gamma_{\text{rad}} + \Gamma_{\text{non-rad}} + \Gamma_{\text{pl}}}. \tag{6.13}$$

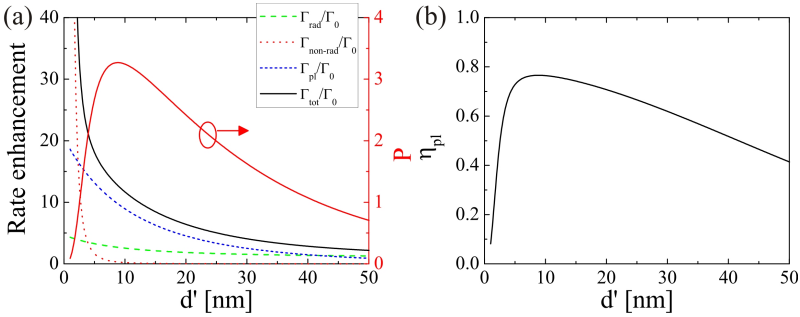

Figure 6.7: (a) Fluorescence rates of a NV center as a function of emitter distance d' from the wire surface for a nano-wire with $R = 25$ nm, a vacuum wavelength of $\lambda_0 = 700$ nm, and $\epsilon_1 = 2$. The red line shows the Purcell factor as defined in the text. (b) Coupling efficiency to the plasmon mode $\eta_{\rm pl}$ as a function of d' for the same parameters as in (a).

For the rates shown in Fig. 6.7 (a), the Purcell factor is plotted as the red solid line in the same graph. $\eta_{\rm pl}$ is plotted in Fig. 6.7 (b) for the rates from (a). Since $\Gamma_{\text{non-rad}}$ is dominating when $d' \to 0$, the plasmon excitation efficiency drops and vanishes for $d' = 0$.

Considering a NV defect in a diamond nano-crystal, one has to account for the rather high refractive index of diamond with $n_{\rm diamond} = 2.4$ This high refractive index of diamond will influence the plasmon mode and subsequently the coupling to it. It suggests that the effective permittivity $\epsilon_{1,\rm eff}$ determining the plasmon mode locally in the vicinity of the diamond is somewhat close to $\epsilon_{diamond} = n^2_{\rm diamond}$. To illustrate the influence of an increased refractive index induced by $\epsilon_{\rm diamond}$, Fig. 6.8 shows $10\log_{10}(P)$ as a function of both R and d' for two different dielectric constants $\epsilon_1 = 2$ (a) and $\epsilon_1 = 5$ (b). The Purcell factor decreases with increasing ϵ_1 for the whole range of parameters R and d'. To further investigate this qualitatively, in Fig. 6.9 the maximum Purcell factor (solid line) obtained by optimizing over emitter distance d' as well the corresponding optimum emitter distance d'_{opt} (dashed line) defined via $\max\{P(d')\} = P(d'_{opt})$ are plotted

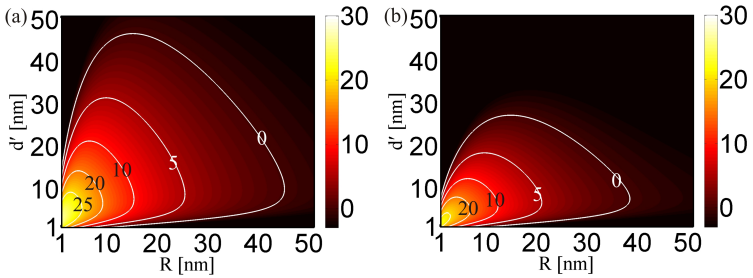

Figure 6.8: $10\log_{10}(P)$ as a function of wire radius R and NV defect distance d' from the surface of the wire for $\epsilon_1 = 2$ (a) and $\epsilon_1 = 5$ (b).

versus the wire radius R for $\epsilon_1 = 2$ (black) and $\epsilon_1 = 5$ (red). As can be seen from the graph, for an increased ϵ_1 the maximum achievable Purcell factor decreases significantly and, in addition, the emitter has to be placed closer to the wire surface in order to obtain the most efficient coupling. This can be explained as follows. In case ϵ_1 increases the surface plasmon mode becomes more localized to the nano-wire surface. This effect was shown qualitatively in Fig. 2.8 (d) for the same parameters as used here. Consequently, in order to increase the overlap between the plasmon mode and the NV-centers dipole moment for increasing ϵ_1, the emitter has to be positioned closer to the nano-wire surface, i.e. d' has to decrease. As a consequence of this, with decreasing d' the decay into the non-radiative mode increases and hence the Purcell factor drops.

6.5.2 Experiment on NV Defect Plasmon Coupling

After investigating the NV defect - plasmon coupling theoretically, the following section is devoted to its experimental realization. The wires employed were synthesized silver nano-wires, whose fabrication was described in detail in section 3.1. Due to the wet chemical growth mechanism these wires are expected to be crystallographically mono

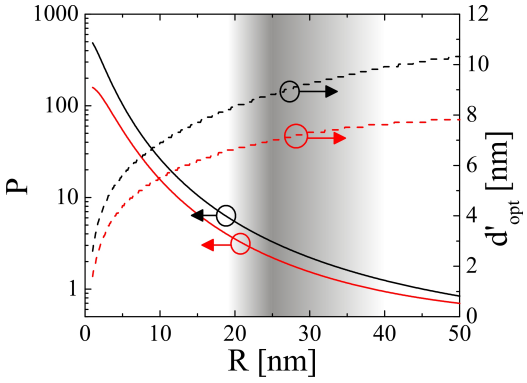

Figure 6.9: Maximum Purcell factor P (left scale, solid lines) and optimum distance to the emitter d' (right scale, dashed lines) for various wire radii and $\epsilon_1 = 2$ (black) and $\epsilon_1 = 5$ (red). The gray shaded area illustrates the radius distribution of the fabricated wires.

crystalline and thus expected to support SPP modes with smallest possible propagation losses.

The samples for studying NV defect - plasmon coupling were prepared as follows. After cleaning the quartz substrate in a plasma asher, the nano-wires were spin coated with ≈ 1000 rpm and a waiting time of ≈ 5 min a prior switching on the spinner. The waiting time depends on the wire density in the solution as well as their adhesion to the surface of the substrate, and was chosen appropriately to obtain single, well separated wires on the sample. On top of the wires, a layer of nano-diamonds was spin coated from a solution with a diamond concentration of ≈ 10 carat/l and 0.5w% PVA. Hence, only by chance a single nano-diamond containing a single NV defect with the right dipole moment orientation is located on top of a nano-wire. After mounting the sample in the confocal microscope (shown in Fig. 6.2 (a)) individual nano-wires were analyzed by fluorescence imaging. In these images, NV defects being located on top of a wire could be identified by a significantly increased luminescence from the nano-wire surface as well as their characteristic spectra. The radiative decay of

the NV defect into the plasmon mode, and thus the NV defect, could be identified by measuring the fluorescence from the nano-wire ends directly. This was done by imaging the fluorescence of the nano-wire with the galvanometric mirror while keeping the position of the pump beam fixed on the NV defect side. As an example, Fig. 6.10 (a) shows the fluorescence image of a combined NV defect - nano-wire system obtained by exciting the NV defect (marked as center) with a pump power of 160 μW. The galvanometric fluorescence image of this NV

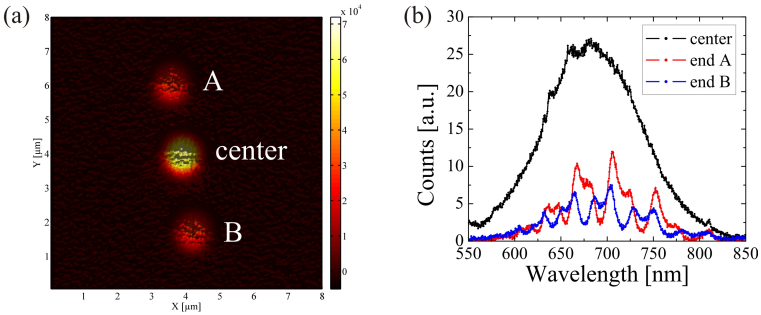

Figure 6.10: Fluorescence image (a) and spectra (b) of a NV defect coupled to a silver nano-wire.

defect - nano-wire system is characterized by three strong emission peaks. The first one is located approximately at the center of the wire and corresponds to the radiative decay channel Γ_{rad} of the emitter. Two more emission peaks appear on the wire ends corresponding to the decay into the plasmonic channel Γ_{pl}, which are labeled as A and B in Fig. 6.10 (a). While propagating along the nano-wire, the plasmonic field amplitude decays as $\propto e^{Im\{k_{\|}\}z}$, where $Im\{k_{\|}\}$ is the imaginary of the plasmon propagation constant. Furthermore, the plasmon scattering into free space modes strongly depends on the nano-wire radius and is expected to decrease for decreasing wire radii [15]. Because of these reasons, the measured intensity on A and B are only proportional to Γ_{pl}.

The respective spectra measured from 'center', 'A', and 'B' are presented in Fig. 6.10 (b). In comparison with an uncoupled NV defect

(see for instance Fig. 6.3), the central emission has a very similar spectrum and thus confirms that this is a NV defect which is coupled to the wire. The spectra taken at the wire ends 'A' and 'B' are strongly modulated due to the fact that the nano-wire can be understood as being a lossy Fabry-Pérot resonator with plasmon mode propagation losses and is consistent with previously reported results [4, 37, 108]. Each end of the wire reflects an incident plasmonic mode with a reflection coefficient ρ [109, 108]. Seen from the NV defect side, a plasmon

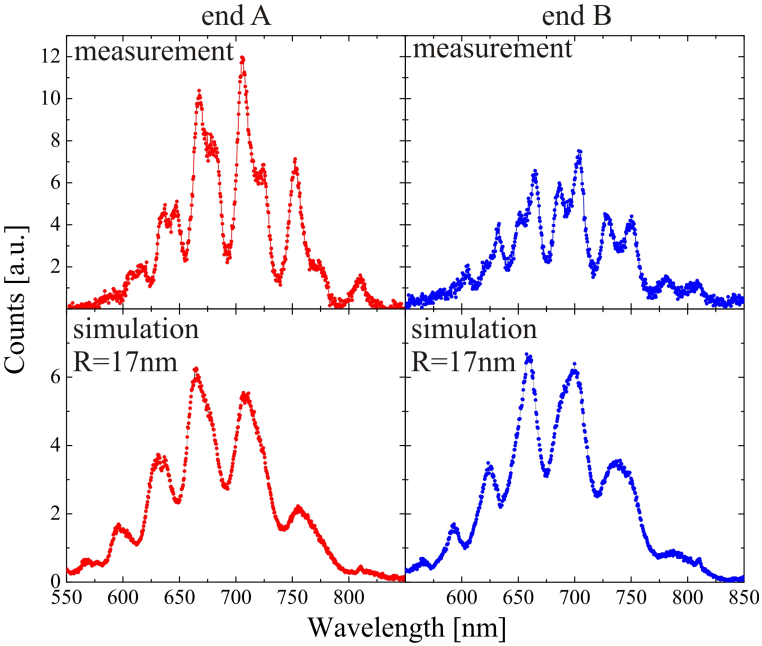

Figure 6.11: Measured and simulated spectra of nano-wire ends. left - wire end A, right - wire end B. Top row - measurement, bottom row - simulation with $R = 17nm$.

propagating towards either end of the wire can be excited. At the wire end A (B) the mode is reflected with an amplitude proportional to ρ and interferes with the mode propagating towards end B (A).

After considering an infinite number of round trips the plasmonic field amplitudes E_{A} and E_{B} on end A and B, respectively, can be expressed as

$$E_{\mathrm{A}} = E_0 \left\{ e^{ik_\parallel d_{\mathrm{A}}} + \rho e^{ik_\parallel d_{\mathrm{B}}} e^{ik_\parallel d} \right\} \frac{1}{1-\rho^2 e^{2d(ik_\parallel)}}, \quad (6.14)$$

$$E_{\mathrm{B}} = E_0 \left\{ e^{ik_\parallel d_{\mathrm{B}}} + \rho e^{ik_\parallel d_{\mathrm{A}}} e^{ik_\parallel d} \right\} \frac{1}{1-\rho^2 e^{2d(ik_\parallel)}}, \quad (6.15)$$

where d_{A} and d_{B} are the distances from the NV defect to the wire ends A and B, respectively, $d = d_{\mathrm{A}} + d_{\mathrm{B}}$ is the total length of the wire, and E_0 is the initial plasmonic field at the NV defect side. The amplitude $E_0 = E_0(\omega)$ is assumed to be proportional to the spectrum of the NV defect and $d_{\mathrm{A}} = 2.1\,\mu$m and $d_{\mathrm{B}} = 2.2\,\mu$m are taken from the fluorescence image Fig. 6.10 (a). The calculation of ρ is summarized in Appendix C. Due to the strong dispersive nature of $k_\parallel = k_\parallel(R)$ (cf. Fig. 2.8), also ρ is strongly depending on the wire radius. For instance, for very thin wire with a radius less than $30nm$ a reflectivity close to unity is obtained, whereas the reflectivity drops to $\approx 7\%$ for large R. The simulated spectra using Eqns. (6.14) and (6.15), which were optimized for $R = 17$ nm, are presented in Fig. 6.11 together with the measured spectra. This radius gives good agreement between experiment and simulation and can be expected from the scanning electron microscope analysis, as shown in Fig. 3.2. As one can see from Fig. 6.11, the measured spectra are superimposed by a smaller modulation. This could be explained by the formation of a shorter Fabry-Pérot cavity than the wire length due to, for instance, small silver nano-particles [37].

The auto-correlation function measured on this system did not show any photon anti-bunching characteristics and is therefore not shown here. This might have manifold reasons: First, the nano-crystal might have contained more than one NV center. Second, fluorescence from the nano-wire might have masked single photon emission by producing noise, and by this destroying the correlation signal. Third, the coupling of the NV defect to the plasmon mode was rather strong such that the anti-bunching dip in the auto-correlation measurement was not resolvable for this system.

For a different NV defect - nano-wire system the anti-bunching dip in the auto-correlation function could be resolved and is presented

in Fig. 6.12. Both measurements shown were obtained for a pump intensity of 160 μW. Fig. 6.12 (a) shows the autocorrelation function measured on the radiative decay channel Γ_{rad}, i.e. the galvanometric channel was aligned to the NV defect side. The autocorrelation function shown in (b) was obtained by aligning the galvanometric channel to one of the wire ends. Thus, this measurements show the correlation between Γ_{rad} and Γ_{pl}. In both graphs the anti-bunching

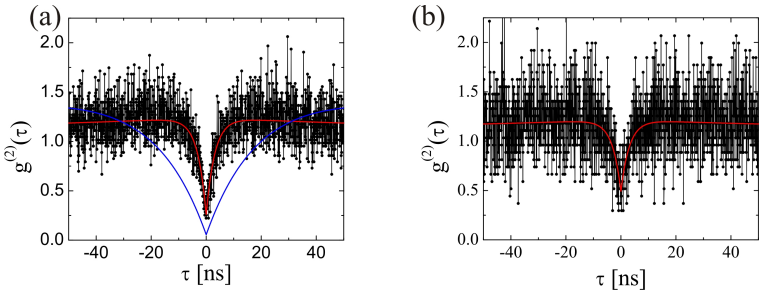

Figure 6.12: Auto-correlation measurement of a NV defect coupled to a nano-wire: (a) correlation between NV defect and (b) between NV defect and wire end.

dip is clearly visible. They are both characterized by a decay time $\tau_2 = 3.1$ns. The values of $g^{(2)}(\tau = 0)$ are determined to be 0.26 in (a) and 0.49 in (b) and demonstrate the excitation of single surface plasmons excited by a NV defect. To illustrate the coupling strength of the NV defect to the SPP mode, the modeled auto-correlation function of an uncoupled NV defect (the same one as shown in Fig. 6.4) is overlayed by a blue line in Fig. 6.12 (a), obtained experimentally for exactly the same pump intensity. In this case, the autocorrelation function of the uncoupled NV defect was characterized by a lifetime $\tau_2 = 18.9$ ns. Since in general τ_2 of uncoupled NV defects in nanodiamonds is broadened, as explained before, this comparison only gives a qualitative measure for the coupling strength. In addition to this, the orientation of the nano-crystals and with this the NV defects dipole moment are random. This fact has as a consequence that the excitation rate k_{ge} will also be influenced by the orientation of the

crystal and has to be taken into account.
The coupled NV defect nano-wire systems are very fragile with respect to pump power and the duration of excitation. Usually, a nano-wire which was not fluorescing at the beginning of the measurement started to show fluorescence after pumping it for a short period of time, which usually was of the order of a dew minutes only. As one consequence of this, the background noise increased due to increased fluorescence from the nano-wire and thus the anti-bunching dip in the $g^{(2)}$ measurement vanished. In the following section, several ideas for improving the experiment will be outlined.

6.6 Outlook

The model of single emitter coupling to metallic nano-wires shows that the emitter decay into the plasmonic channel strongly depends on the distance of the NV defect to the nano-wire surface. Furthermore, it was assumed in the model that the orientation of the emitters dipole moment is along the radial direction of the wire. In addition, a dependence on the dielectric property of the surrounding medium has to be considered. Thus, future investigations of single NV defect - plasmon mode coupling will have to be carried out in a more deterministic way by controlling the positioning of the single nano-diamond with respect to the nano-wire. For instance, this can be done by using an atomic force microscope (AFM). In recent publications, people showed that single diamond nano-crystals could be moved across the sample and be placed at desired positions, for instance on top of a photonic crystal cavity [110]. In another work, single gold nano-spheres were moved around single diamond nano-crystals with an AFM [90]. Motivated by these demonstrations, future investigations of the NV center - plasmon coupling might include the following steps. First, single crystal nano-diamond will be deposited on the sample in small quantity using a tapered fiber [110]. By using the confocal microscope in combination with an AFM operating in tapping mode, single crystals containing one NV defect with desired properties will be selected and separated from other crystals. Second, after depositing a small quantity of nano-wires on the same substrate, the NV center will be brought in a controlled way in the

near vicinity of the wire by switching the AFM from tapping mode operation to contact mode operation. By recording the fluorescence decay lifetime, which determines the total decay rate Γ_{tot}, in combination with Γ_{rad} and Γ_{pl} this will allow to determine the optimum NV center nano-wire coupling distance d'_{opt} and with this the maximum Purcell factor, as described by the model in section 6.5.1. A modified schematic diagram of the experimental setup for this approach is shown in Fig. 6.13. Another parameter which is required

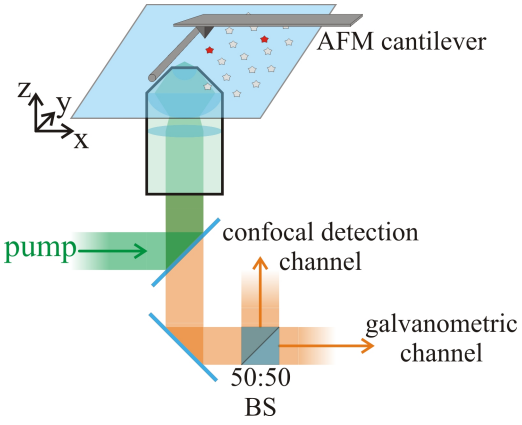

Figure 6.13: Future experimental setup for controlled coupling of NV defects to metallic nano-wires.

to be optimized is the size of the nano-diamonds. As calculated in section 6.5.1, the optimum coupling distance d'_{opt} is less than 10 nm for a wide range of wire radii R. To open the possibility of investigating the whole parameter range of d', single digit nano-diamonds with diameter of less than 10 nm will have to be used. Implanted NV defects in nano-diamonds as small as 4 nm were reported for instance in Ref. [111].

One characteristic feature of synthesized nano-wires is that their size as well length is randomly distributed. In addition to this they can only be spin coated on the substrate such that their position with respect to other structures is random. To circumvent these points, we

started to work on lithographic gold and silver nano-wires. As summarized in Appendix D, structures grown lithographically are highly fluorescing with a spectrum largely overlapping with the broad NV spectrum. In addition to this, due to their poly-crystalline composition lithographically grown nano-wires have huge propagation losses such that no propagating SPPs could be observed in the near infrared spectral region.
The efficient single emitter excitation of surface plasmons on nano-wires is only the first step towards single photon generation on demand [13, 14] and other quantum photonic devices based on, for instance, strong non-linear interaction at the level of single photons like a single photon transistor [16]. In order to build such a device it is necessary to couple the plasmonic mode of a nano-wire efficiently to either free space modes or to a dielectric waveguide. The latter structure has recently been described in a theoretical article on short-range plasmon mode coupling to dielectric wave-guides [112]. In this article it was shown that efficient coupling of the SR-SPP mode to the mode of the dielectric waveguide can be obtained with a coupling interaction length of a few μm with coupling losses originating only from SPP propagation losses.

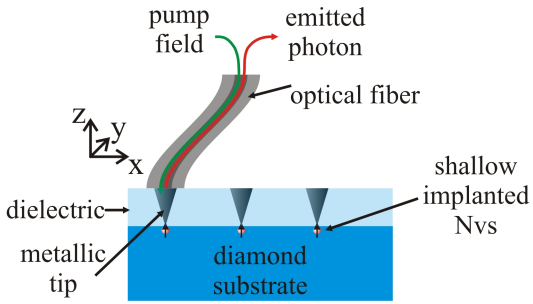

Figure 6.14: Proposal for efficient coupling of shallow implanted NV defects to an optical fiber.

Another very interesting approach is to couple the plasmonic mode of a tapered metallic structure directly to an optical fiber supporting higher order Laguerre Gaussian modes [113]. Such a device, which is

illustrated in Fig. 6.14, could be used for both, efficient single photon generation as well as strong non-linear interaction at low light levels. Its functionality is as follows. The pump light field is guided inside the optical fiber in the negative z-direction and butt-coupled to the plasmonic mode on the wide end of a metallic tip. The plasmon mode propagates along the tapered metallic cone towards the tip [114, 115], where it excites a single NV-center. Subsequently, the NV-defect couples to the plasmonic mode [13, 14], which then propagates along the metal cone in the positive z-direction, before it couples into the fiber. As a sample base could serve an ultra-pure (110) diamond substrate with shallow implanted NVs. The NV-centers symmetry axis is along any of the four tetrahedral $\langle 111 \rangle$ crystallographic directions. By chance, this direction could be the [111] or the $[\bar{1}\bar{1}1]$ direction, which has a significant component perpendicular to (110) and thus allows coupling between the plasmon mode and the NV-center [14]. The NV center position needs to be determined accurately. For this, a technique called stimulated emission depletion (SED) could be used. The ability of SED for locating NV-centers with an accuracy down to $5.8nm$ has been shown recently [116]. The diamond will then be covered by a dielectric medium with a thickness of a few μm. In order to position metallic tips on top of the NV-centers, conical holes will need to be etched into the dielectric material with the NV center lying along the cone axis. The cones will be filled up by thermal metal evaporation. An optical fiber, which supports higher order Laguerre Gauss modes, will be positioned on top of the metallic cones and be used to guide both the pump light field as well as re-emitted 'single' photons [113].

6.7 Conclusion

In this chapter, the electronic properties of NV-centers in diamond were described in great detail. This description was followed by a presentation of the home-build confocal microscope used for characterizing the single photon emission properties of NV-centers. The functionality of this setup include fluorescence imaging, lifetime measurement, $g^{(2)}(\tau)$ measurement, and spectral characterization. All of these characterization methods were described in detail. The second-

order correlation function of a single NV-defect has been introduced theoretically and confirmed by the experiment. Following this, the model for single emitter coupling to the plasmonic mode of a metallic nano-wire was presented. After this, an experiment has been performed where a single NV-center was coupled to the plasmonic mode of a chemically prepared silver nano-wire. The plasmon excitation and re-emission was shown by a fluorescence image as well as the according spectra. Single plasmon excitation was confirmed by a $g^{(2)}(\tau)$ measurement. Following this, the experimental limitations of the presented measurements were discussed. Spin-coating is certainly not the optimum way of preparing coupled NV-center nano-wire systems due to the resulting random orientation of the NV-centers with respect to the nano-wire. To circumvent this problem, an improved experimental approach using atomic force microscopy in combination with fluorescence imaging was suggested. Finally, the functionality and fabrication procedure of an integrated structure was presented. This structure can be fabricated by available nano-fabrication techniques and is based on bidirectional photon/plasmon coupling, adiabatic plasmon mode propagation, and interaction between the plasmonic mode and a single NV-center.

7

Conclusion and Outlook

In this work, the excitation and characterized of non-classical surface plasmon modes was investigated. After a general introduction to SPP modes on metal stripes and nm-sized cylindrical wires, the fabrication of these structures has been presented.

The excitation of LR-SPP modes on metal stripes has been achieved with free space optics and verified by its polarization dependency. Fabry-Pérot like resonances of these LR-SPP modes were investigated for three different wave-guide lengths by measuring simultaneously the transmission and reflection while tuning the temperature of the sample. The observed oscillations could be simulated by a lossy Fabry-Pérot cavity. By fitting the model to the experimental results, the LR-SPP propagation losses were obtained. It was found that the propagation losses are slightly higher than expected from theory.

Due to the third order non-linearity of gold, a power dependent absorption from LR-SPPs propagating along thin gold films is expected. This behavior was studied in detail in Chapter 4. By measuring the transmission of a continuous wave laser field, the steady state absorption could be analyzed and modeled by a power dependent absorption coefficient in Beer's law. LR-SPP modes were also excited using Lorentzian shaped laser pulses with μs to ms durations. From these measurements, a 'slow' thermal dependence of the absorption

coefficient could be deduced. However, the duration of the applied pulses is too long for the investigating fast absorption properties of the LR-SPP mode.

The experiment described in Chapter 5 analyzes the excitation of LR-SPP with quadrature squeezed vacuum states. In comparison to previous work done in this field, where non-classical SPPs were analyzed in a two-dimensional Hilbert space, the analysis performed in this work was done in an infinite-dimensional Hilbert space. The experiment was carried out in two consecutive steps. First, the squeezed vacuum state was characterized completely by reconstructing the density matrix using homodyne detection and a maximum likelihood method. Second, a LR-SPP mode on a thin gold film embedded in BCB was excited by the same squeezed vacuum state. The re-emitted optical mode was then characterized using the same method. The impact of the LR-SPP mode on the squeezed vacuum state could be simulated by a standard beam splitter model. The result of this simulation was compared to the initial squeezed vacuum state using the fidelity as a measure. Very good agreement between the experiment and the LR-SPP beam splitter model was found. The experimental results could be explained by a simple theoretical arguments and are in agreement with previous work done in that field of research.

In Chapter 6, an experiment was described which might path the way towards an efficient single photon source utilizing plasmonic nano-structures and NV-centers embedded in diamond nano-crystals. First, the single photon emission of NV-centers in diamond nano-crystals was studied in detail using a home-build confocal microscope. In the second part of this chapter, the coupling of NV-centers to metallic nano-wires was described using realistic experimental parameters. The coupling of NV defects to plasmonic modes on synthesized nano-wires could be shown by measuring the fluorescence from the end facets of the nano-wire. A measurement of the second-order correlation function confirmed the excitation of single surface plasmons. The sample for these studies was prepared by means of spin-coating. Thus, coupled NV-center plasmon systems only assembled by chance and an optimization of the coupling was not possible. In future, this issue might be circumvented by nano-scale manipulation using an atomic force microscope mounted on top of the present confocal imaging system.

Part III

Appendix

A

Generating Quadrature Squeezed Vacuum States

A.1 Introduction

Over the past decades a various number of different sources for producing quadrature squeezed light have been proposed and also demonstrated. The first squeezing of the electromagnetic field has been demonstrated with non-degenerate four-wave mixing using Na atoms in an optical cavity by Slusher et al. in 1985 [117]. Later on, squeezed states were obtained using degenerate optical parametric down conversion in an optical cavity [118] and by exploiting the Kerr-effect in optical fibers [119]. Up to now, these sources have been improved further and records in quadrature squeezing were reported with -11.5 ± 0.1 dB produced with an optical parametric oscillator [120] and -6.8 ± 0.3 dB produced with ultrashort photonic pulses in a single pass of a birefringent fiber [121].

Due to the availability of a continuous wave (cw) laser, an approach for producing squeezed light with an optical paramagnetic amplifier (OPA) has been chosen.

A.2 The experimental setup

The laser system

The laser which has been used for the squeezed light source is an Innolight cw Diabolo laser with a monolithic neodymium-doped yttrium aluminium garnet (ND:YAG) crystal lasing at a wavelength of 1064 nm. Inside the laser, approximately 90% of the light at 1064 nm is tapped off and used for second harmonic generation (SHG) at 532 nm with a semi-monolithic lithium triborate (LBO) cavity. The 532 nm light was used as pump field for the down-conversion process taking place inside the optical parametric amplifier (OPA).

The mode cleaning cavities

A schematic diagram of the optical experimental setup is presented in Fig. A.1. Right after the laser, the IR beam as well as the green beam were injected both into mode cleaning cavities (MCCs). These MCCs had two purposes. The first one is that the MCCs act as a mode filter on the incident laser beam to provide a spatially uniform TEM_{00} beam on their output. Second, outside the cavity resonance the MCC filters noise from the incident laser beam. Thus, the cavities act as an optical low pass filter on the incident laser and provide shot noise limited beams on their output.
The MCC cavities are composed out of two highly reflective (HR) plane mirrors and one HR curved mirror with a radius of curvature of 1000 mm, as indicated in Fig. A.1. The curved mirrors were mounted on a piezo electric actuator which was used to tune the cavities resonance line to the laser frequency. All cavity mirrors were housed inside a monolithic aluminium block to increase the mechanical stability and isolate the system from air fluctuations. Both MCCs are designed with an optical path length of 400 mm. By measuring the MCCs free spectral range as well as the full width at half maximum (FWHM) of a single transmission peak, the Finesse has been determined to be ≈ 194 for the IR cavity and ≈ 280 for the green cavity. This gives a theoretical line width (half width at half maximum) of 1.9 MHz for the IR MCC cavity and 1.3 MHz for the green MCC cavity. For stable operation on a time scale of several hours, both

MCCs were frequency stabilized to the incident laser beam using the Pound-Drever Hall PDH locking technique [122]. For this, the respective laser beams were phase modulated at an optical side-band frequency of 20 MHz (IR) and 19.2 MHz (green) using two electro-optic modulators (EOMs), as shown in Fig. A.1. The locking signals were detected by measuring the reflection from the MCCs input port.

The optical parametric amplifier

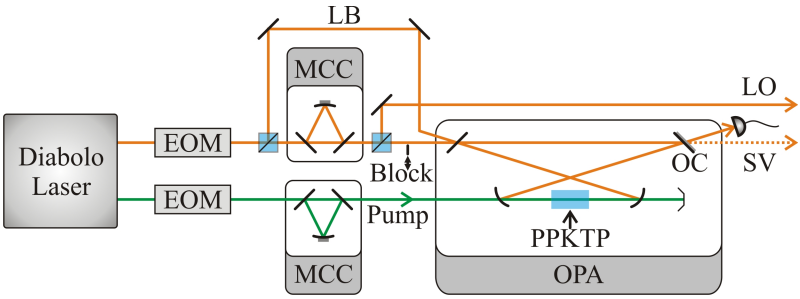

Figure A.1: Schematic diagram of the experimental setup for squeezed vacuum generation: EOM - electro optic modulator, MCC - mode cleaning cavity, LB - locking beam, OPA - optical parametric amplifier, OC - output coupler, LO - local oscillator, and SV - squeezed vacuum.

The OPA built for the experiments in this work is based on a bow-tie shaped optical cavity, as illustrated in Fig. A.1. This design is similar to the cavities in Refs. [123, 124]. The cavity is composed of two plane mirrors and two curved mirrors with a radius of curvature of 50 mm. One of the plane cavity mirrors, which is acting as the output coupler (OC) of the squeezed light field, has a transmissivity of 10%, whereas all other mirrors are highly reflecting. The optical round trip path length is approximately 275 mm. In between the two curved mirrors, a periodically poled KTP (PPKTP) crystal with dimensions $10 \times 1 \times 2\,\mathrm{mm}^3$ is placed. Via a second order χ^2 nonlinear optical process this PPKTP crystal acts as an optical down-

conversion source inside the cavity. For phase matching the PPKTP crystal to the laser light field, the crystal was hosted inside a copper mount and temperature stabilized with a peltier element to $\approx 31°$. The OC has been mounted on a pre-loaded mirror holder including a piezo electric element for fine-tuning its position. The bandwidth of this mount was determined to be $\approx$ 55 kHz. Fig. A.2 (a) shows the transmission through the OPA while linearly tuning the position of the OC. Illustrated are the cavity FSR and the FWHM of a single TEM_{00} transmission peak. From this, the OPA Finesse and the line width are determined to be 52 and 10.5 MHz, respectively.

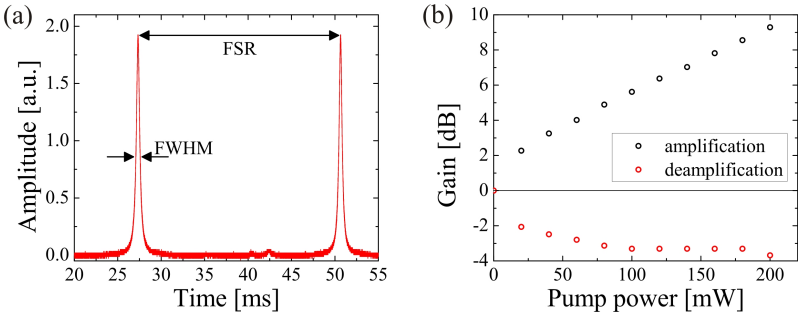

Figure A.2: Transmission through the OPA while linearly sweeping the OPA round trip length. Illustrated is the free spectral range (FSR) of the cavity as distance between two subsequent transmission peaks as well as the full width half maximum (FWHM) of a single peak.

For stabilizing the cavity resonance to the laser frequency, a counter propagating beam emerging from the same laser source is launched into the OPA, as illustrated in Fig. A.1. By using the phase modulation signal at 20 MHz and the Pound-Drever-Hall locking technique [122], the resonance frequency of the OPA could be stabilized for up to several hours.
By injecting the 532 nm pump beam into the OPA, the inside cavity field is amplified or de-amplified depending on the relative phase between the fields. The maximum achievable amplification and de-amplification depending on the pump beam power is presented in Fig. A.2 (b). These results were obtained by seeding the OPA with a

weak beam emerging directly from the IR-MCC and measuring the power on the OPA output. At maximum, a seed de-amplification of ≈ 3.8 dB was observed, what was limited due to phase fluctuations of the system. These gains determine the approximate achievable vacuum squeezing and anti-squeezing values of the OPA when the seed beam is blocked. The achievable squeezing and anti-squeezing values for a given pump power are presented in Fig. A.3. The measurements were taken at an optical side-band frequency of 5 MHz with a resolution of 300 kHz and a video bandwidth of 300 Hz.

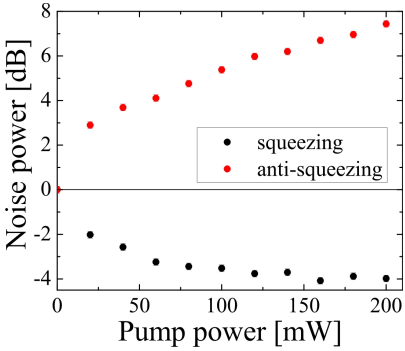

Figure A.3: OPA squeezing and anti-squeezing values versus the pump power of the OPA cavity.

Tomographic Quantum State Reconstruction

B.1 Maximum Likelihood Estimation

A common problem in experimental science can be formulated in the question: Given some observation of a system, which model can best describe the underlying system? Usually one makes assumptions or knows a functional relationship between independent and dependent variables of the system $y = f(x_1, x_2, ...)$, where y is the variable being measured. The model depends on one or more parameters $\mathbf{s}$, $f(x_1, x_2, ...; \mathbf{s})$, and these parameters should be estimated based on the observations $\{y_j\}$. One can calculate the probability $pr\left(\{y_j\}|\mathbf{s}\right)$ for the observed outcome to have happened, given the model and parameters $\mathbf{s}$. For estimation of the parameters, the data $\{y_j\}$ are given and the parameters $\mathbf{s}$ are unknown. The probability for an outcome to occur is considered as a function of the parameters and is called the maximum likelihood function

$$\mathcal{L}(S) \equiv pr\left(\{y_i\}|\mathbf{s}\right). \tag{B.1}$$

The parameters $\mathbf{s}_0$ which are most likely to be correct are the ones that maximize the likelihood function for given data $\{y_j\}$. This principal is the basis for the maximum likelihood method. The parame-

ters $\mathbf{s}_0$ that maximize the likelihood are called the maximum likelihood estimator. If the observations $\{y_j\}$ are independent, the total outcome probability is just the product of the probabilities of the individual samples. Since a logarithm turns a product into a sum, usually the expression

$$\ln\left(\mathcal{L}(S)\right) = \ln \prod_j pr\left(y_j|\mathbf{s}\right) = \sum_j \ln\, pr\left(y_j|\mathbf{s}\right) \tag{B.2}$$

is used for the likelihood. In standard maximum likelihood estimation, the maximization of the log-likelihood can be carried out in various ways, one of which is the iterative expectation-maximization algorithm [125]. Various variations of this algorithm have been used for quantum state estimation, for instance [126, 127, 128].

B.2 Application to Homodyne Measurements

The maximum likelihood method has been applied to characterize squeezed states of light used in chapter 5. For continuous variable quantum states, the maximum likelihood method has been introduced by A. Lvovsky in [129].
The state generation was repeated a large number of times via a continuous operation of the OPA. For each generated state of this ensemble a marginal distribution has been recorded using homodyne detection. The ensemble of detection outcomes correspond to the observations $\{y_j\}$, which are independent from each other. The distribution depends on the prepared state and the phase ϕ_j of the local oscillator set for the homodyne detector. The distribution measured for a local oscillator phase ϕ_j is determined by the density matrix $\hat{\rho}$ of the quantum state generated. Based on the observed samples, the maximum likelihood method has been applied to reconstruct the entries $\hat{\rho}_{m,n}$ of the density matrix $\hat{\rho}$ in the Fock state basis. In this case, the matrix entries $\{\rho_{m,n}\}$ play the role of the parameters $\mathbf{s}$.
With the homodyne detection system, one performs a large set of von Neumann measurements, where each measurement is projecting the state of the system onto an eigenstate of the measurement apparatus

$|y_j\rangle$. Here, the set of all possible outcomes $\{|y_j\rangle\}$ can be associated with either one or several measurement bases. Let f_j be the frequency of occurrences for each outcome. With the system being in the quantum state $\hat{\rho}$ the likelihood of a particular data set $\{f_j\}$ is then given by

$$\mathcal{L}(\hat{\rho}) = \prod_j pr_j^{f_j} = \prod_j \langle y_j| \hat{\rho} |y_j\rangle^{f_j} = \prod_j Tr\{\hat{\Pi}_j \hat{\rho}\}^{f_j}, \tag{B.3}$$

where $\hat{\Pi}_j = |y_j\rangle \langle y_j|$ is the projection operator on state $|y_j\rangle$.
In order to find the ensemble $\hat{\rho}_0$ which maximizes the likelihood (B.3) the iteration operator

$$\hat{R}(\hat{\rho}) = \sum_j \frac{f_j}{pr_j} \hat{\Pi}_j \tag{B.4}$$

is introduced. For the ensemble $\hat{\rho}_0$ that is most likely to be the correct data set $f_j \approx pr_j$ and since $\sum_j \hat{\Pi}_j = \hat{1}$ the equation

$$\hat{R}(\hat{\rho}_0)\hat{\rho}_0 = \hat{\rho}_0 \hat{R}(\hat{\rho}_0) \approx \hat{\rho}_0 \tag{B.5}$$

holds as well as

$$\hat{\rho}_0 \hat{R}(\hat{\rho}_0)\hat{\rho}_0 \approx \hat{\rho}_0. \tag{B.6}$$

The last equation is the basis for the iterative maximum likelihood algorithm. To find the most likely data set $\hat{\rho}_0$ one chooses an initial density matrix $\hat{\rho}^{(0)}$ and applies the repetitive iterations

$$\hat{\rho}^{(k+1)} = \mathcal{N}\left[\hat{R}(\hat{\rho}^{(k)})\hat{\rho}^{(k)}\hat{R}(\hat{\rho}^{(k)})\right], \tag{B.7}$$

where $\mathcal{N}$ denotes normalization to unity trace. Each step monotonically increases the likelihood of equation (B.3) and will asymptotically approach the maximum likelihood ensemble $\hat{\rho}_0$.
For infinitely small bins of the measurement outcome, f_{ϕ_j, y_j} becomes either 0 or 1 and thus the likelihood (B.3) of a data set $\{(\phi_j, y_j)\}$ reduces to

$$\ln\left(\mathcal{L}(S)\right) = \sum_j \ln\, pr_{\phi_j}\left(y_j\right) \tag{B.8}$$

and the iteration operator $\hat{R}(\hat{\rho})$ becomes

$$\hat{R}(\hat{\rho}) = \sum_j \frac{\hat{\Pi}(\phi_j, y_j)}{pr_{\phi_j}(y_j)}. \tag{B.9}$$

In the experiment one measures the field quadratures $\hat{X}^{\phi} = \hat{X}\cos(\phi) + \hat{Y}\sin(\phi)$ of a quantum state $\hat{\rho}$ at various angles ϕ of the local oscillator, where $\hat{X}$ and $\hat{Y}$ are the amplitude and phase quadrature of the light field, respectively. For a given phase ϕ the projection operator is given by

$$pr_{\phi}(y) = Tr\left[\hat{\Pi}(\phi, y)\hat{\rho}\right], \tag{B.10}$$

where $\hat{\Pi}(\phi, y) = |\phi, y\rangle\langle\phi, y|$ is the projector onto this quadrature eigenstate. In the Fock state representation, the projection operator is expressed as

$$\Pi_{mn} = \langle m|\hat{\Pi}(\phi, y)|n\rangle = \langle m|\phi, y\rangle\langle\phi, y|n\rangle, \tag{B.11}$$

where the overlap between the Fock state $\langle m|$ and the quadrature eigenstate $|\phi, y\rangle$ is the solution for a particle in a harmonic potential

$$\langle m|\phi, y\rangle = e^{im\phi}\left(\frac{2}{\pi}\right)^{1/4}\frac{H_m(\sqrt{2}y)}{\sqrt{2^m m!}}e^{-y^2}, \tag{B.12}$$

with $H_m(x)$ being the Hermite polynomial of degree m. Here, the phase space is normalized such that $\left[\hat{X}, \hat{Y}\right] = i/2$.

In general, the description of a continuous variable quantum state of arbitrary amplitude requires an infinite dimensional Fock-state basis. However, the quantum states usually produced in the laboratory have a finite amplitude and thus, the dimension of $\hat{\rho}$ can be truncated to a finite number of Fock states. This is done by excluding Fock terms above a certain threshold from the calculation. In particular, this is valid for weekly squeezed vacuum states as used in chapter 5. In these specific calculations, the dimension of $\hat{\rho}$ has been truncated to a maximum photon number of $m = 15$. This was a valid truncation since basically all entries in $\hat{\rho}_{\text{in}}$ above $m = 6$ were close to 0.

B.3 Notes on the Implementation

For calculating the density matrixes produced in the experiments, the above described maximum likelihood method has been implemented in a Matlab code. Including the data acquisition the carried out steps were as following. First, the shot noise level of the homodyne detector was recorded by blocking the OPA mode with settings of the data acquisition system as mentioned in chapter 5. The shot-noise level is determined by the standard deviation of the recorded shot noise data. Second, the OPA (or LR-SPP) mode was unblocked and the marginal distributions of the produced quantum states were recorded while linearly scanning the phase ϕ of the local oscillator. In a third step, the recorded data was normalized to the shot noise level. For simplicity, this finally obtained data will be denoted as homodyne data in the following.
The local oscillator phase ϕ was scanned linearly with a large amplitude. Thus, the homodyne data include marginal distributions corresponding to several rotations in the quadrature plane. In order to find a data set corresponding to a 2π rotation in the quadrature plane, the variance of of the homodyne data was computed. In the variance plot, a 2π quadrature plane rotation was identified by selecting the data between the minima m and $m+2$, where m is an integer. Such a data set containing approximately 0.5 million points is shown in Fig. 5.2. Each data point y_i of the selected set was then identified by a phase ϕ_i, linearly distributed from 0 to 2π. This complete set $\{(\phi_i, y_i)\}$ served as the input for the maximum likelihood method.
The key step of the maximum likelihood algorithm is the calculation of the matrix elements $R_{mn}(\hat{\rho}^{(k)})$ of the iteration operator $\hat{R}(\hat{\rho}^{(k)})$ each iteration step k. Practically, the matrix elements $R_{mn}(\hat{\rho}^{(k)})$ are obtained by inserting Eqn. (B.10) into Eqn. (B.9), giving the result

$$\begin{aligned} R_{mn}(\hat{\rho}^{(k)}) &= \sum_j \frac{\langle m|\,\hat{\Pi}(\phi_j, y_j)\,|n\rangle}{p r_\phi(y)} \\ &= \sum_j \frac{\langle m|\phi_j, y_j\rangle\,\langle \phi_j, y_j|n\rangle}{\sum_{u,v}\langle u|\phi_j, y_j\rangle\,\langle \phi_j, y_j|v\rangle\,\rho_{u,v}^{(k)}}, \end{aligned} \tag{B.13}$$

what is readily computed for the whole data set $\{(\phi_j, y_j)\}$ using Eqn. (B.12). Now, the density matrix $\hat{\rho}^{(k+1)}$ is easily obtained by

computing $\hat{R}(\hat{\rho}^{(k)})\hat{\rho}^{(k)}\hat{R}(\hat{\rho}^{(k)})$ and re-normalization to unity trace. As an initial density matrix the vacuum state was chosen, $\hat{\rho}^{(0)} = |0\rangle\langle 0|$, since it already has a significant overlap with the finally expected squeezed vacuum state.
Finally, the iteration was terminated if the inequality

$$\delta > \sum_{m,n} \left| \left| \rho_{m,n}^{(k)} \right| - \left| \rho_{m,n}^{(k+1)} \right| \right| \tag{B.14}$$

was fulfilled for $\delta = 1{\cdot}10^{-4}$. $\hat{\rho}^{(k+1)}$ was then taken to be the maximum likelihood estimator $\hat{\rho}_0$ of the quantum state under investigation.

C

Calculation of Nano-wire Reflection Coefficients

The method for calculating the plasmon reflection coefficients from the wire end facets is adopted from the method for an infinite wide slab [108, 109]. A wire with radius R is assumed to be abruptly cut at $z = 0$ and extends in positive $z-$direction, as shown in Fig. 2.7. In all directions, the wire is surrounded by a medium with a real and positive dielectric constant ϵ_1. The wire is assumed to be made of silver with ϵ_{Ag} being calculated using the Drude model Eqn. (2.13). For simplicity, the imaginary part of ϵ_{Ag} is neglected in the following calculations.

For $r < R$, the fields of the fundamental plasmon mode are given by

$$H_\phi = AI_1\left(k_{\perp 2}r\right)e^{ik_{\parallel z}} = H^{SP}_{\phi,r<R}e^{ik_{\parallel z}}, \tag{C.1}$$

$$E_z = -iA\frac{k_{\perp 2}c}{\omega\epsilon_{Ag}}I_0\left(k_{\perp 2}r\right)e^{ik_{\parallel z}} = E^{SP}_{z,r<R}e^{ik_{\parallel z}}, \tag{C.2}$$

$$E_r = A\frac{k_{\parallel}c}{\omega\epsilon_{Ag}}I_1\left(k_{\perp 2}r\right)e^{ik_{\parallel z}} = E^{SP}_{r,r<R}e^{ik_{\parallel z}}, \tag{C.3}$$

and for $r > R$ they are given by

$$H_\phi = A\frac{I_1(k_{\perp 2}R)}{K_1(k_{\perp 1}R)}K_1(k_{\perp 1}r)\,e^{ik_\parallel z} = H^{SP}_{\phi,r>R}e^{ik_\parallel z}, \quad \text{(C.4)}$$

$$E_z = iA\frac{k_{\perp 1}c}{\omega\epsilon_1}\frac{I_1(k_{\perp 2}R)}{K_1(k_{\perp 1}R)}K_0(k_{\perp 1}r)\,e^{ik_\parallel z} = E^{SP}_{z,r>R}e^{ik_\parallel z}, \quad \text{(C.5)}$$

$$E_r = A\frac{k_\parallel c}{\omega\epsilon_1}\frac{I_1(k_{\perp 2}R)}{K_1(k_{\perp 1}R)}K_1(k_{\perp 1}r)\,e^{ik_\parallel z} = E^{SP}_{r,r>R}e^{ik_\parallel z}. \quad \text{(C.6)}$$

Here, A is the plasmonic field amplitude, ω is the frequency of the electromagnetic field, c is the vacuum speed of light, $k_\parallel$ is the wave vector of the plasmon obtained by solving Eqn. (2.17) numerically, $k_{\perp,1,2} = \sqrt{k_\parallel^2 - \epsilon_{1,met}k_0^2}$, and I_m and K_m are m-th order modified Bessel functions.
At $z = 0$ the fields on the nano-wire consist of the incoming and the reflected wave, thus

$$H_\phi(z > 0) = (1-\rho)H^{SP}_\phi, \quad \text{(C.7)}$$

$$E_r(z > 0) = (1+\rho)E^{SP}_r, \quad \text{(C.8)}$$

where ρ is the complex field amplitude reflection coefficient.
For $z < 0$ the plasmonic mode couples to free space modes, which might be expressed as

$$H^{FS}_{\phi,z<0} = \int_0^\infty h_\phi(k)J_1(kr)kdk, \quad \text{(C.9)}$$

$$E^{FS}_{r,z<0} = \int_0^\infty e_r(k)J_1(kr)kdk, \quad \text{(C.10)}$$

where $h_\phi(k)$ and $e_r(k)$ are the amplitudes of the magnetic and the electric field with wave-vectors k, respectively. $e_r(k)$ is related to $h_\phi(k)$ via

$$e_r(k) = \frac{1}{\sqrt{\epsilon_1}}\sqrt{1 - \frac{k^2}{\epsilon_1 k_0^2}}h_\phi(k). \quad \text{(C.11)}$$

At $z = 0$, the azimuthal component of the magnetic field and the radial component of the electric field have to match, giving the con-

ditions

$$(1-\rho)H_\phi^{SP} = H_\phi^{FS}, \quad (C.12)$$

$$(1+\rho)E_r^{SP} = E_r^{FS}. \quad (C.13)$$

Multiplying Eqn. (C.12) by $J_1(k'r)$ and integrating over r yields the amplitude of the magnetic free space modes with the result

$$h_\phi(k) = (1-\rho)\int_0^\infty H_\phi^{SP}(r)J_1(kr)rdr = (1-\rho)h_{phi}^{SP}(k). \quad (C.14)$$

Here, the orthogonality relation of Bessel functions $\int_0^\infty rJ_m(kr)J_m(k'^r) = \frac{1}{k}\delta(k-k')$ was used with $\delta(x)$ being the Dirac delta distribution. Finally, the equation for ρ is obtained by multiplying Eqn. (C.13) with H_ϕ^{SP} and integrating over r, what gives

$$(1+\rho)\int_0^\infty E_r^{SP}(r)H_\phi^{SP}(r)rdr = (1-\rho)\int_0^\infty \frac{1}{\epsilon_1}\sqrt{1-\frac{k}{\epsilon_1 k_0^2}}h_\phi^{SP}(k)^2kdk. \quad (C.15)$$

This equation was solved numerically in Matlab for a different wire radii R and wavelength λ_0 and thus delivers the complex reflection coefficient ρ. To account for the glass substrate and the PVA used in the

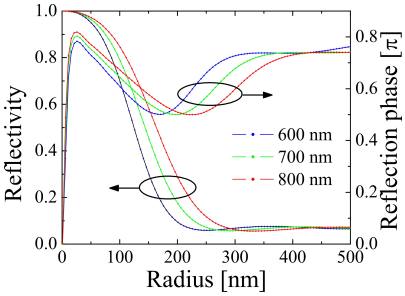

Figure C.1: Reflectivity $|\rho|^2$ and reflection phase $\cos^{-1} Re\{\rho\}/|\rho|$ of a nano-wire end facet as a function of wire radius R for three different vacuum wavelength covering the main experimental range.

experiment, an $\epsilon_1 = 1.2$ was chosen in the simulation. Fig. C.1 shows

the wire reflectivity $|\rho|^2$ and the reflection phase $\cos^{-1}(Re\{\rho\}/|\rho|)$ as a function of R for three different λ_0 covering the relevant spectral region of the experiment.

D

Lithographic Gold Nano-Wires

The work on lithographically fabricated nano-structures for the application in plasmonics is motivated by the improvement of various different micro- and nano-fabrication techniques and in conjunction with the development of novel materials. In comparison to synthesized metallic structures the main advantage of using lithography is that this technique allows one to fabricate structures with almost any shape and dimension. The root mean square accuracy of an electron-beam (e-beam) lithography setup is around 4 nm, and structures with sizes down to 30 nm can be fabricated. However, the properties of nm sized gold stripes need to be further improved, especially for the application in the visible and near infrared region of the spectrum.

D.1 Fabrication of the Structures

Gold nano-wires were fabricated using e-beam lithography. The fabrication started by spin-coating a thin layer of e-beam resist ZEP520A 3.6% with a 1:2 ratio in anisol on a quartz substrate. The spinning was done at 2000 rpm for 30 s resulting in a 90 nm thick resist layer. Afterwards, the resist was cured at 180 °C for 2 min. This was followed by thermal deposition of a 20 nm Al layer to avoid charging of the waver during e-beam exposure. After this, the nano-wire struc-

tures were written with an electron-beam[1] to the resist with a dose of 230 μC/cm^2, with width from 20 nm up to 200 nm and length from 2 μm up to 10 μm. Next, the Al layer was removed in MF-322 by dipping the waver for 1 min in the solution with manual stirring. Following this, the resist was developed in Zed-N50 for 2 min. This step was followed by electron beam evaporative gold deposition[2] of 15 nm at a rate of 0.2 nm/s and lift-off. The lift-off was done in microposit 1165 remover. As an example, Fig. D.1 (a) shows a scanning electron microscope (SEM) image of a few 30 nm wide gold stripes of different length. Due to proximity effects the minimum gold stripe

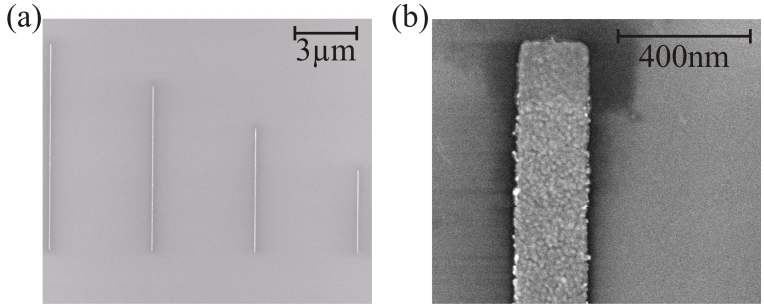

Figure D.1: (a) A few gold nano-wires fabricated on a quartz substrate by electron-beam lithography. These stripe have a width of 30 nm and length from 1 μm up to 10 μm. (b) Close up view of a 200 nm wide gold stripe.

width which could be fabricated was 30 nm. A close up view of a 200 nm wide stripe is presented in Fig. D.1 (b). This image shows that the nano-wire surface is rough and that the wire is composed of nm-sized gold particles.

D.2 Fluorescence Measurements

Fluorescence measurements of the fabricated lithographic gold wires were carried out in the experimental setup shown in Fig. 6.2 (a) with a

[1] JEOL e-beam lithography system with 100 keV.
[2] Alcatel SCM 600 E-beam metal deposition system.

continuous wave excitation laser at $\lambda_0 = 532$ nm. An fluorescence image, taken with an excitation power of 32 μW, is presented in Fig. D.2 (a). It shows that the gold structures are highly fluorescing with a

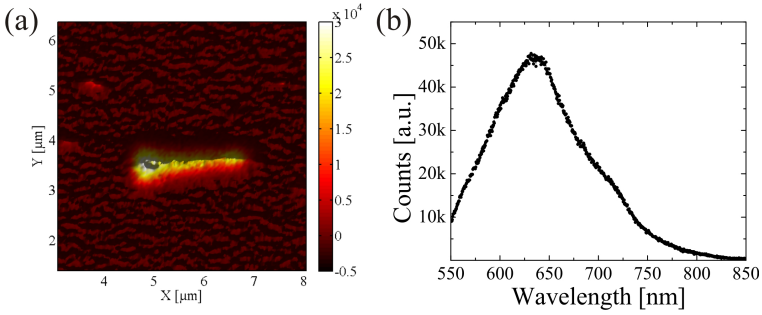

Figure D.2: Fluorescence image of a lithographically fabricated gold tip structure.

spectrum as the one shown in Fig. D.2 (b). The maximum emission from the fluorescence lies at around 630 nm, corresponding approximately to the breakdown wavelength of the free electron gas model. This spectrum has a large overlap with the broad spectrum of a NV defect, thus the two spectra are practically impossible to distinguish. In contrast to synthesized silver nano-wires, no propagating plasmons were detected on the gold structures. Possibly, the poly-crystalline composition of the gold structure cause the SPP propagation loss to be tremendously large, such that the propagation length is on the order of a few nm only. It should be noted that the propagation length of these fabricated gold nano-wires is only ≈ 2 μm for an ideal ϵ_{Au} calculated by the Drude model. As shown in Ref. [4], in case of lithographic silver nano-wires the propagation properties are also very poor.

E

Picture Gallery

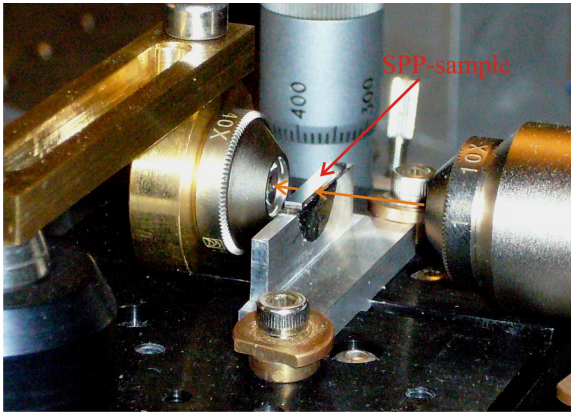

Figure E.1: Picture of the sample holder for LR-SPPs excitation.

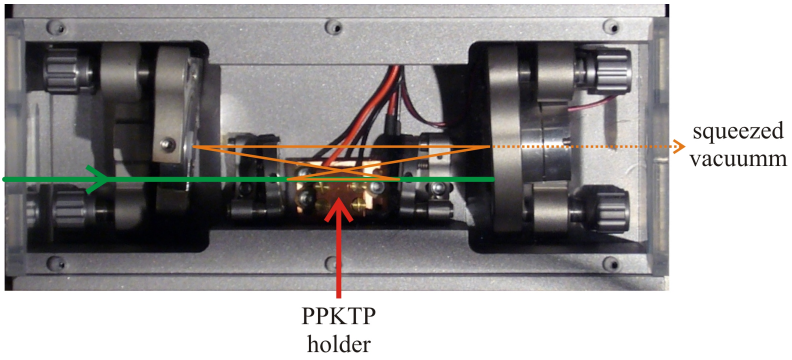

Figure E.2: Picture of the OPA cavity: Illustrated are the pump field (green), the intracavity field (orange, solid line), and the output squeezed vacuum field (orange, dashed line).

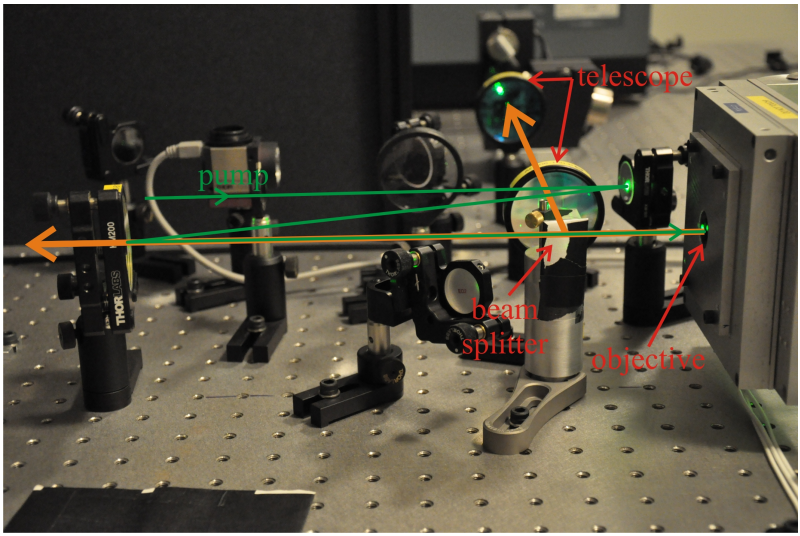

Figure E.3: Picture of the confocal microscope illustrating the beam path of the pump beam and the fluorescence photons, as well as a few optical components.

Bibliography

[1] R. H. Ritchie. Plasma losses by fast electrons in thin films. *Phys. Rev.*, 106(5):874–881, Jun 1957.

[2] Junichi Takahara, Suguru Yamagishi, Hiroaki Taki, Akihiro Morimoto, and Tetsuro Kobayashi. Guiding of a one-dimensional optical beam with nanometer diameter. *Opt. Lett.*, 22(7):475–477, 1997.

[3] Stefan A. Maier, Pieter G. Kik, Harry A. Atwater, Sheffer Meltzer, Elad Harel, Bruce E. Koel, and Ari A.G. Requicha. Local detection of electromagnetic energy transport below the diffraction limit in metal nanoparticle plasmon waveguides. *Nat Mater*, pages 229–232, 2003.

[4] Harald Ditlbacher, Andreas Hohenau, Dieter Wagner, Uwe Kreibig, Michael Rogers, Ferdinand Hofer, Franz R. Aussenegg, and Joachim R. Krenn. Silver nanowires as surface plasmon resonators. *Phys. Rev. Lett.*, 95(25):257403, Dec 2005.

[5] Sergey I. Bozhevolnyi, Valentyn S. Volkov, Eloise Devaux, Jean-Yves Laluet, and Thomas W. Ebbesen. Channel plasmon sub-

wavelength waveguide components including interferometers and ring resonators. *Nature*, 440:508–511, 2006.

[6] Katrin Kneipp, Yang Wang, Harald Kneipp, Lev T. Perelman, Irving Itzkan, Ramachandra R. Dasari, and Michael S. Feld. Single molecule detection using surface-enhanced raman scattering (sers). *Phys. Rev. Lett.*, 78(9):1667–1670, Mar 1997.

[7] Shuming Nie and Steven R. Emory. Probing Single Molecules and Single Nanoparticles by Surface-Enhanced Raman Scattering. *Science*, 275(5303):1102–1106, 1997.

[8] A. Bouhelier, M. Beversluis, A. Hartschuh, and L. Novotny. Near-field second-harmonic generation induced by local field enhancement. *Phys. Rev. Lett.*, 90(1):013903, Jan 2003.

[9] J. A. H. van Nieuwstadt, M. Sandtke, R. H. Harmsen, F. B. Segerink, J. C. Prangsma, S. Enoch, and L. Kuipers. Strong modification of the nonlinear optical response of metallic subwavelength hole arrays. *Phys. Rev. Lett.*, 97(14):146102, Oct 2006.

[10] Seungchul Kim, Jonghan Jin, Young-Jin Kim, In-Yong Park, Yunseok Kim, and Seung-Woo Kim. High-harmonic generation by resonant plasmon field enhancement. *Nature*, 453:757–760, 2008.

[11] Alexandra Boltasseva, Thomas Nikolajsen, Kristjan Leosson, Kasper Kjaer, Morten S. Larsen, and Sergey I. Bozhevolnyi. Integrated optical components utilizing long-range surface plasmon polaritons. *Journal of Lightwave Technology,*, 23:413–422, 2005.

[12] Thomas W. Ebbesen, Cyriaque Genet, and Sergey I. Bozhevolnyi. Surface-plasmon circuitry. *Physics Today*, 61(5):44–50, 2008.

[13] D. E. Chang, A. S. Sørensen, P. R. Hemmer, and M. D. Lukin. Quantum optics with surface plasmons. *Physical Review Letters*, 97(5):053002, 2006.

[14] D. E. Chang, A. S. Sørensen, P. R. Hemmer, and M. D. Lukin. Strong coupling of single emitters to surface plasmons. *Physical Review B (Condensed Matter and Materials Physics)*, 76(3):035420, 2007.

[15] A. V. Akimov, A. Mukherjee, C. L. Yu, D. E. Chang, A. S. Zibrov, P. R. Hemmer, H. Park, and M. D. Lukin. Generation of single optical plasmons in metallic nanowires coupled to quantum dots. *Nature*, 450(06230):402–406, 2007.

[16] Darrick E. Chang, Anders S. Sørensen, Eugene A. Demler, and Mikhail D. Lukin. A single-photon transistor using nanoscale surface plasmons. *Nature Physics*, 3:807–812, 2007.

[17] Y. Fedutik, V. V. Temnov, O. Schöps, U. Woggon, and M. V. Artemyev. Exciton-plasmon-photon conversion in plasmonic nanostructures. *Physical Review Letters*, 99(13):136802, 2007.

[18] David J. Bergman and Mark I. Stockman. Surface plasmon amplification by stimulated emission of radiation: Quantum generation of coherent surface plasmons in nanosystems. *Phys. Rev. Lett.*, 90(2):027402, Jan 2003.

[19] E. Altewischer, M. P. van Exter, and J. P. Woerdman. Plasmon-assisted transmission of entangled photons. *Nature*, 418(6895):304–306, 2002.

[20] Sylvain Fasel, Franck Robin, Esteban Moreno, Daniel Erni, Nicolas Gisin, and Hugo Zbinden. Energy-time entanglement preservation in plasmon-assisted light transmission. *Phys. Rev. Lett.*, 94(11):110501, Mar 2005.

[21] A. Sommerfeld. Üeber die fortpflanzung elektrodynamischer wellen längs eines drahtes. *Annalen der Physik und Chemie*, 303(2):233–290.

[22] Alexander Huck, Stephan Smolka, Peter Lodahl, Anders S. Sørensen, Alexandra Boltasseva, Jiri Janousek, and Ulrik L. Andersen. Demonstration of quadrature-squeezed surface plasmons in a gold waveguide. *Physical Review Letters*, 102(24):246802, 2009.

[23] Radim Filip, Petr Marek, and Ulrik L. Andersen. Measurement-induced continuous-variable quantum interactions. *Phys. Rev. A*, 71(4):042308, Apr 2005.

[24] J. Niset, U. L. Andersen, and N. J. Cerf. Experimentally feasible quantum erasure-correcting code for continuous variables. *Phys. Rev. Lett.*, 101(13):130503, Sep 2008.

[25] P. B. Johnson and R. W. Christy. Optical constants of the noble metals. *Phys. Rev. B*, 6(12):4370–4379, Dec 1972.

[26] Atsushi Ishikawa, Takuo Tanaka, and Satoshi Kawata. Negative magnetic permeability in the visible light region. *Phys. Rev. Lett.*, 95(23):237401, Dec 2005.

[27] E. Dulkeith, T. Niedereichholz, T. A. Klar, J. Feldmann, G. von Plessen, D. I. Gittins, K. S. Mayya, and F. Caruso. Plasmon emission in photoexcited gold nanoparticles. *Phys. Rev. B*, 70(20):205424, Nov 2004.

[28] Jie Zheng, Yong Ding, Bozhi Tian, Zhong Lin Wang, and Xiaowei Zhuang. Luminescent and raman active silver nanoparticles with polycrystalline structure. *J. Am. Chem. Soc.*, 130(32):10472–10473, July 2008.

[29] J. J. Burke, G. I. Stegeman, and T. Tamir. Surface-polariton-like waves guided by thin, lossy metal films. *Phys. Rev. B*, 33(8):5186–5201, Apr 1986.

[30] B.E.A. Saleh and M.C. Teich. *Fundamentals of Photonics*. John Wiley & Sons, 1991.

[31] John David Jackson. Classical electrodynamics, 1998.

[32] Kylee E. Korte, Sara E. Skrabalak, and Younan Xia. Rapid synthesis of silver nanowires through a cucl- or cucl2-mediated polyol process. *Journal of Materials Chemistry*, 18(4):437–441, 2008.

[33] Stefan Alexander Maier. *Plasmonics: Fundamentals and Applications*. Springer Science+Business Media LLC, 2007.

[34] G. I. Stegeman, R. F. Wallis, and A. A. Maradudin. Excitation of surface polaritons by end-fire coupling. *Opt. Lett.*, 8(7):386–388, 1983.

[35] Robert Charbonneau, Pierre Berini, Ezio Berolo, and Ewa Lisicka-Shrzek. Experimental observation of plasmon polariton waves supported by a thin metal film of finite width. *Opt. Lett.*, 25(11):844–846, 2000.

[36] Thierry Laroche and Christian Girard. Near-field optical properties of single plasmonic nanowires. *Applied Physics Letters*, 89(23):233119, 2006.

[37] Marco Allione, Vasily V. Temnov, Yuri Fedutik, Ulrike Woggon, and Mikhail V. Artemyev. Surface plasmon mediated interference phenomena in low-q silver nanowire cavities. *Nano Letters*, 8:31–35, 2008.

[38] Vasily V. Temnov, Ulrike Woggon, José Dintinger, Eloise Devaux, and Thomas W. Ebbesen. Surface plasmon interferometry: measuring group velocity of surface plasmons. *Opt. Lett.*, 32(10):1235–1237, 2007.

[39] The Dow Chemical Company. Processing procedures for cyclotene 3000 series resin. http://www.dow.com/cyclotene/prod/302257.htm.

[40] S. Guo, I. Lundström, and H. Arwin. Temperature sensitivity and thermal expansion coefficient of benzocyclobutene thin films studied with ellipsometry. *Applied Physics Letters*, 68(14):1910–1912, 1996.

[41] Yasumasa Okada and Yozo Tokumaru. Precise determination of lattice parameter and thermal expansion coefficient of silicon between 300 and 1500 k. *Journal of Applied Physics*, 56(2):314–320, 1984.

[42] F. C. Nix and D. MacNair. The thermal expansion of pure metals: Copper, gold, aluminum, nickel, and iron. *Phys. Rev.*, 60(8):597–605, Oct 1941.

[43] N. Bloembergen. Surface nonlinear optics: a historical overview. *Applied Physics B: Lasers and Optics*, 68(3):289–293, 1999.

[44] H. J. Simon, D. E. Mitchell, and J. G. Watson. Optical second-harmonic generation with surface plasmons in silver films. *Phys. Rev. Lett.*, 33(26):1531–1534, Dec 1974.

[45] C. Flytzanis, F. Hache, M.C. Klein, D. Ricard, and Ph. Roussignol. V nonlinear optics in composite materials: 1. semiconductor and metal crystallites in dielectrics: 1. semiconductor and metal crystallites in dielectrics. volume 29 of *Progress in Optics*, pages 321 – 411. Elsevier, 1991.

[46] Guang Yang, Dongyi Guan, Weitian Wang, Weidong Wu, and Zhenghao Chen. The inherent optical nonlinearities of thin silver films. *Optical Materials*, 25(4):439 – 443, 2004.

[47] W. T. Wang, D. Y. Guan, G. Yang, G. Z. Yang, Y. L. Zhou, H. B. Lu, and Z. H. Chen. Nonlinear optical properties of thin iron films grown on mgo (100) by pulsed laser deposition. *Thin Solid Films*, 471(1-2):86 – 90, 2005.

[48] E. Xenogiannopoulou, P. Aloukos, S. Couris, E. Kaminska, A. Piotrowska, and E. Dynowska. Third-order nonlinear optical properties of thin sputtered gold films. *Optics Communications*, 275(1):217 – 222, 2007.

[49] R.W. Boyd. *Nonlinear Optics*. Academic Press, 2008.

[50] F. Hache, D. Ricard, C. Flytzanis, and U. Kreibig. The optical kerr effect in small metal particles and metal colloids: The case of gold. *Applied Physics A: Materials Science & Processing*, 47(4):347–357, 1988.

[51] F. de Rougemont and R. Frey. Two-level approach to saturation properties in semiconductor materials. *Phys. Rev. B*, 37(3):1237–1244, Jan 1988.

[52] S. Schmitt, J. Ficker, M. Wolff, F. König, A. Sizmann, and G. Leuchs. Photon-number squeezed solitons from an asymmetric fiber-optic sagnac interferometer. *Phys. Rev. Lett.*, 81(12):2446–2449, Sep 1998.

[53] Wolfgang P. Schleich. *Quantum Optics in Phase Space*. Wiley-VCH, 2001.

[54] L. Mandel and E. Wolf. *Optical Coherence and Quantum Optics*. Camebridge University Press, 1995.

[55] G. D. Boyd and D. A. Kleinman. Parametric interaction of focused gaussian light beams. *Journal of Applied Physics*, 39(8):3597–3639, 1968.

[56] Ulf Leonhardt. *Measuring the quantum state of light*. Camebridge University Press, 2005.

[57] Richard Jozsa. Fidelity for mixed quantum states. *Journal of Moden Optics*, 41(12):2315–2323, 1994.

[58] Esteban Moreno, F. J. García-Vidal, Daniel Erni, J. Ignacio Cirac, and L. Martín-Moreno. Theory of plasmon-assisted transmission of entangled photons. *Phys. Rev. Lett.*, 92(23):236801, Jun 2004.

[59] S. H. Perlmutter, M. D. Levenson, R. M. Shelby, and M. B. Weissman. Inverse-power-law light scattering in fused-silica optical fiber. *Phys. Rev. Lett.*, 61(12):1388–1391, Sep 1988.

[60] J. I. Cirac, P. Zoller, H. J. Kimble, and H. Mabuchi. Quantum state transfer and entanglement distribution among distant nodes in a quantum network. *Phys. Rev. Lett.*, 78(16):3221–3224, Apr 1997.

[61] L.-M. Duan and H. J. Kimble. Scalable photonic quantum computation through cavity-assisted interactions. *Phys. Rev. Lett.*, 92(12):127902, Mar 2004.

[62] A. Wallraff, D. I. Schuster, A. Blais, L. Frunzio, R.-S. Huang, J. Majer, S. Kumar, S. M. Girvin, and R. J. Schoelkopf. Strong

coupling of a single photon to a superconducting qubit using circuit quantum electrodynamics. *Nature*, 431:162–167, 2004.

[63] J. McKeever, A. Boca, A. D. Boozer, J. R. Buck, and H. J. Kimble. Experimental realization of a one-atom laser in the regime of strong coupling. *Nature*, 425:268–271, 2003.

[64] Matthias Keller, Birgit Lange, Kazuhiro Hayasaka, Wolfgang Lange, and Herbert Walther. Continuous generation of single photons with controlled waveform in an ion-trap cavity system. *Nature*, 431:1075–1078, 2004.

[65] Takao Aoki, Barak Dayan, E. Wilcut, W. P. Bowen, A. S. Parkins, T. J. Kippenberg, K. J. Vahala, and H. J. Kimble. Observation of strong coupling between one atom and a monolithic microresonator. *Nature*, 443:671–674, 2006.

[66] Jasprit Singh. *Physics of Semiconductors and Their Heterostructures*. Mcgraw-Hill College, 1992.

[67] A. Gruber, A. Drbenstedt, C. Tietz, L. Fleury, J. Wrachtrup, and C. von Borczyskowski. Scanning confocal optical microscopy and magnetic resonance on single defect centers. *Science*, 276(5321):2012–2014, 1997.

[68] J. Wrachtrup, S. Ya. Kilin, and A. P. Nizovtsev. Quantum computation using the ^{13}C nuclear spins near the single nv defect center in diamond. *Optics and Spectroscopy*, 91(3):429–437, 2001.

[69] F. Jelezko, I. Popa, A. Gruber, C. Tietz, J. Wrachtrup, A. Nizovtsev, and S. Kilin. Single spin states in a defect center resolved by optical spectroscopy. *Applied Physics Letters*, 81(12):2160–2162, 2002.

[70] F. Jelezko, T. Gaebel, I. Popa, A. Gruber, and J. Wrachtrup. Observation of coherent oscillations in a single electron spin. *Phys. Rev. Lett.*, 92(7):076401, Feb 2004.

[71] F. Jelezko and J. Wrachtrup. Read-out of single spins by optical spectroscopy. *Journal of Physics: Condensed Matter*, 16(30):R1089–R1104, 2004.

[72] R. Hanson, O. Gywat, and D. D. Awschalom. Room-temperature manipulation and decoherence of a single spin in diamond. *Physical Review B (Condensed Matter and Materials Physics)*, 74(16):161203, 2006.

[73] Rosa Brouri, Alexios Beveratos, Jean-Philippe Poizat, and Philippe Grangier. Photon antibunching in the fluorescence of individual color centers in diamond. *Opt. Lett.*, 25(17):1294–1296, 2000.

[74] Christian Kurtsiefer, Sonja Mayer, Patrick Zarda, and Harald Weinfurter. Stable solid-state source of single photons. *Phys. Rev. Lett.*, 85(2):290–293, Jul 2000.

[75] R Alléaume, F Treussart, G Messin, Y Dumeige, J-F Roch, A Beveratos, R Brouri-Tualle, J-P Poizat, and P Grangier. Experimental open-air quantum key distribution with a single-photon source. *New Journal of Physics*, 6(1):92, 2004.

[76] Liang Jiang, Jacob M. Taylor, Anders S. Sørensen, and Mikhail D. Lukin. Distributed quantum computation based on small quantum registers. *Physical Review A (Atomic, Molecular, and Optical Physics)*, 76(6):062323, 2007.

[77] P. Neumann, N. Mizuochi, F. Rempp, P. Hemmer, H. Watanabe, S. Yamasaki, V. Jacques, T. Gaebel, F. Jelezko, and J. Wrachtrup. Multipartite entanglement among single spins in diamond. *Science*, 320(5881):1326–1329, 2008.

[78] M. V. Gurudev Dutt, L. Childress, L. Jiang, E. Togan, J. Maze, F. Jelezko, A. S. Zibrov, P. R. Hemmer, and M. D. Lukin. Quantum Register Based on Individual Electronic and Nuclear Spin Qubits in Diamond. *Science*, 316(5829):1312–1316, 2007.

[79] N. B. Manson, J. P. Harrison, and M. J. Sellars. Nitrogen-vacancy center in diamond: Model of the electronic structure and associated dynamics. *Physical Review B (Condensed Matter and Materials Physics)*, 74(10):104303, 2006.

[80] G. Davies and M. F. Hamer. Optical studies of the 1.945 ev vibronic band in diamond. *Proceedings of the Royal Society of London. Series A, Mathematical and Physical Sciences*, 348(1653):285–298, 1976.

[81] D. A. Redman, S. Brown, R. H. Sands, and S. C. Rand. Spin dynamics and electronic states of n-v centers in diamond by epr and four-wave-mixing spectroscopy. *Phys. Rev. Lett.*, 67(24):3420–3423, Dec 1991.

[82] N. R. S. Reddy, N. B. Manson, and E. R. Krausz. Two-laser spectral hole burning in a colour centre in diamond. *Journal of Luminescence*, 38(1-6):46 – 47, 1987.

[83] E. van Oort, N. B. Manson, and M. Glasbeek. Optically detected spin coherence of the diamond n-v centre in its triplet ground state. *Journal of Physics C: Solid State Physics*, 21(23):4385–4391, August 1988.

[84] N. B. Manson, P. T. H. Fisk, and X.-F. He. Application of the raman heterodyne technique for the detection of epr and endor. *Applied Magnetic Resonance*, 3(6):999–1019, Dec 1992.

[85] G. D. Fuchs, V. V. Dobrovitski, R. Hanson, A. Batra, C. D. Weis, T. Schenkel, and D. D. Awschalom. Excited-state spectroscopy using single spin manipulation in diamond. *Physical Review Letters*, 101(11):117601, 2008.

[86] A. Batalov, V. Jacques, F. Kaiser, P. Siyushev, P. Neumann, L. J. Rogers, R. L. McMurtrie, N. B. Manson, F. Jelezko, and J. Wrachtrup. Low temperature studies of the excited-state structure of negatively charged nitrogen-vacancy color centers in diamond. *Physical Review Letters*, 102(19):195506, 2009.

[87] J. Martin, R. Wannemacher, J. Teichert, L. Bischoff, and B. Köhler. Generation and detection of fluorescent color centers in diamond with submicron resolution. *Applied Physics Letters*, 75(20):3096–3098, 1999.

[88] J. R. Rabeau, P. Reichart, G. Tamanyan, D. N. Jamieson, S. Prawer, F. Jelezko, T. Gaebel, I. Popa, M. Domhan, and

J. Wrachtrup. Implantation of labelled single nitrogen vacancy centers in diamond using [sup 15]n. *Applied Physics Letters*, 88(2):023113, 2006.

[89] Gopalakrishnan Balasubramanian, Philipp Neumann, Daniel Twitchen, Matthew Markham, Roman Kolesov, Norikazu Mizuochi, Junichi Isoya, Jocelyn Achard, Johannes Beck, Julia Tissler, Vincent Jacques, Philip R. Hemmer, Fedor Jelezko, and Jörg Wrachtrup. Ultralong spin coherence time in isotopically engineered diamond. *Nature Materials*, 8:383–387, 2009.

[90] S. Schietinger, M. Barth, T. Aichele, and O. Benson. Plasmon-enhanced single photon emission from a nanoassembled metal-diamond hybrid structure at room temperature. *Nano Letters*, 9(4):1694–1698, 2009.

[91] I. Rech, I. Labanca, M. Ghioni, and S. Cova. Modified single photon counting modules for optimal timing performance. *Review of Scientific Instruments*, 77(3):033104, 2006.

[92] R. Hanbury Brown and R. Q. Twiss. A test of a new type of stellar interferometer on sirius. *Nature*, 178:1046–1048, 1956.

[93] Rodnay Loudon. *The Quantum Theory of Light*. 1983.

[94] G. Nienhuis and C.Th.J. Alkemade. Atomic radiative transition probabilities in a continuous medium. *Physica B+C*, 81(1):181 – 188, 1976.

[95] Alexios Beveratos, Rosa Brouri, Thierry Gacoin, Jean-Philippe Poizat, and Philippe Grangier. Nonclassical radiation from diamond nanocrystals. *Phys. Rev. A*, 64(6):061802, Nov 2001.

[96] A T Collins, M F Thomaz, and M I B Jorge. Luminescence decay time of the 1.945 ev centre in type ib diamond. *Journal of Physics C: Solid State Physics*, 16(11):2177, 1983.

[97] E.M. Purcell. Spontaneous emission probabilities of radio frequencies. *Phys. Rev.*, 69(11–12):681, 1946.

[98] X. Brokmann, L. Coolen, M. Dahan, and J. P. Hermier. Measurement of the radiative and nonradiative decay rates of single cdse nanocrystals through a controlled modification of their spontaneous emission. *Phys. Rev. Lett.*, 93(10):107403, Sep 2004.

[99] Charles Santori, David Fattal, Jelena Vuc(kovic', Glenn S. Solomon, and Yoshihisa Yamamoto. Indistinguishable photons from a single-photon device. *Nature*, 419(6907):594, 2002.

[100] Peter Lodahl, A. Floris van Driel, Ivan S. Nikolaev, Arie Irman, Karin Overgaag, Daniel Vanmaekelbergh, and Willem L. Vos. Controlling the dynamics of spontaneous emission from quantum dots by photonic crystals. *Nature*, 430(7000):654–657, 2004.

[101] Dirk Englund, David Fattal, Edo Waks, Glenn Solomon, Bingyang Zhang, Toshihiro Nakaoka, Yasuhiko Arakawa, Yoshihisa Yamamoto, and Jelena Vučković. Controlling the spontaneous emission rate of single quantum dots in a two-dimensional photonic crystal. *Phys. Rev. Lett.*, 95(1):013904, Jul 2005.

[102] J. N. Farahani, D. W. Pohl, H.-J. Eisler, and B. Hecht. Single quantum dot coupled to a scanning optical antenna: A tunable superemitter. *Phys. Rev. Lett.*, 95(1):017402, Jun 2005.

[103] Pascal Anger, Palash Bharadwaj, and Lukas Novotny. Enhancement and quenching of single-molecule fluorescence. *Physical Review Letters*, 96(11):113002, 2006.

[104] Sergei Kühn, Ulf Håkanson, Lavinia Rogobete, and Vahid Sandoghdar. Enhancement of single-molecule fluorescence using a gold nanoparticle as an optical nanoantenna. *Physical Review Letters*, 97(1):017402, 2006.

[105] T. H. Taminiau, F. D. Stefani, F. B. Segerink, and N. F. van Hulst. Optical antennas direct single-molecule emission. *Nature Photonics*, 2:234–237, 2008.

[106] O. L. Muskens, V. Giannini, J. A. Sánchez-Gil, and J. Gómez Rivas. Strong enhancement of the radiative decay rate of

emitters by single plasmonic nanoantennas. *Nano Letters*, 7(9):2871–2875, 2007.

[107] Jian Zhang, Yi Fu, Mustafa H. Chowdhury, and Joseph R. Lakowicz. Metal-enhanced single-molecule fluorescence on silver particle monomer and dimer: Coupling effect between metal particles. *Nano Letters*, 7(7):2101–2107, 2007.

[108] Roman Kolesov, Bernhard Grotz, Gopalakrishnan Balasubramanian, Rainer J. Stöhr, Aurélien A. L. Nicolet, Philip R. Hemmer, Fedor Jelezko, and Jörg Wrachtrup. Waveparticle duality of single surface plasmon polaritons. *Nature Physics*, 5:470–474, 2009.

[109] Reuven Gordon. Vectorial method for calculating the fresnel reflection of surface plasmon polaritons. *Phys. Rev. B*, 74(15):153417, Oct 2006.

[110] Michael Barth, Nils Nüsse, Bernd Löchel, and Oliver Benson. Controlled coupling of a single-diamond nanocrystal to a photonic crystal cavity. *Opt. Lett.*, 34(7):1108–1110, 2009.

[111] Julia Tisler, Gopalakrishnan Balasubramanian, Boris Naydenov, Roman Kolesov, Bernhard Grotz, Rolf Reuter, Jean-Paul Boudou, Patrick A. Curmi, Mohamed Sennour, Alain Thorel, Michael Börsch, Kurt Aulenbacher, Rainer Erdmann, Philip R. Hemmer, Fedor Jelezko, and Jörg Wrachtrup. Fluorescence and spin properties of defects in single digit nanodiamonds. *ACS Nano*, 3(7):1959–1965, Oct 2009.

[112] Ruiyuan Wan, Fang Liu, Xuan Tang, Yidong Huang, and Jiangde Peng. Vertical coupling between short range surface plasmon polariton mode and dielectric waveguide mode. *Applied Physics Letters*, 94(14):141104, 2009.

[113] Xue-Wen Chen, Vahid Sandoghdar, and Mario Agio. Highly efficient interfacing of guided plasmons and photons in nanowires. *Nano Letters*, 9(11):3756–3761, 2009.

[114] Ewold Verhagen, Albert Polman, and L. (Kobus) Kuipers. Nanofocusing in laterally tapered plasmonic waveguides. *Opt. Express*, 16(1):45–57, 2008.

[115] Ewold Verhagen, Marko Spasenović, Albert Polman, and L. (Kobus) Kuipers. Nanowire plasmon excitation by adiabatic mode transformation. *Phys. Rev. Lett.*, 102(20):203904, May 2009.

[116] Eva Rittweger, Kyu Young Han, Scott E. Irvine, Christian Eggeling, and Stefan W. Hell. Sted microscopy reveals crystal colour centres with nanometric resolution. *Nature Photonics*, 3:144–147, 2009.

[117] R. E. Slusher, L. W. Hollberg, B. Yurke, J. C. Mertz, and J. F. Valley. Observation of squeezed states generated by four-wave mixing in an optical cavity. *Phys. Rev. Lett.*, 55(22):2409–2412, Nov 1985.

[118] Ling-An Wu, H. J. Kimble, J. L. Hall, and Huifa Wu. Generation of squeezed states by parametric down conversion. *Phys. Rev. Lett.*, 57(20):2520–2523, Nov 1986.

[119] R. M. Shelby, M. D. Levenson, S. H. Perlmutter, R. G. DeVoe, and D. F. Walls. Broad-band parametric deamplification of quantum noise in an optical fiber. *Phys. Rev. Lett.*, 57(6):691–694, Aug 1986.

[120] Moritz Mehmet, Henning Vahlbruch, Nico Lastzka, Karsten Danzmann, and Roman Schnabel. Observation of squeezed states with strong photon number oscillations, 2009.

[121] Ruifang Dong, Joel Heersink, Joel F. Corney, Peter D. Drummond, Ulrik L. Andersen, and Gerd Leuchs. Experimental evidence for raman-induced limits to efficient squeezing in optical fibers. *Opt. Lett.*, 33(2):116–118, 2008.

[122] R. W. P. Drever, J. L. Hall, F. V. Kowalski, J. Hough, G. M. Ford, A. J. Munley, and H. Ward. Laser phase and frequency stabilization using an optical resonator. *Applied Physics B*, 31(2):97–105, 1983.

[123] Shigenari Suzuki, Hidehiro Yonezawa, Fumihiko Kannari, Masahide Sasaki, and Akira Furusawa. 7 db quadrature squeezing at 860 nm with periodically poled ktiopo[sub 4]. *Applied Physics Letters*, 89(6):061116, 2006.

[124] Yuishi Takeno, Mitsuyoshi Yukawa, Hidehiro Yonezawa, and Akira Furusawa. Observation of -9 db quadrature squeezing with improvement of phasestability in homodyne measurement. *Opt. Express*, 15(7):4321–4327, 2007.

[125] Y. Vardi and D. Lee. From image deblurring to optimal investments: Maximum likelihood solutions for positive linear inverse problems. *Journal of the Royal Statistical Society. Series B (Methodological)*, 55(3):569–612, 1993.

[126] Z. Hradil. Quantum-state estimation. *Phys. Rev. A*, 55(3):R1561–R1564, Mar 1997.

[127] J. Řeháček, Z. Hradil, and M. Ježek. Iterative algorithm for reconstruction of entangled states. *Phys. Rev. A*, 63(4):040303, Mar 2001.

[128] Jaromír Fiurášek. Maximum-likelihood estimation of quantum measurement. *Phys. Rev. A*, 64(2):024102, Jul 2001.

[129] A I Lvovsky. Iterative maximum-likelihood reconstruction in quantum homodyne tomography. *Journal of Optics B: Quantum and Semiclassical Optics*, 6(6):S556, 2004.

Acknowledgements

Without the support of my colleagues, friends, and family the work reported in this thesis would not have been achievable. My supervisor Ulrik L. Andersen made it possible for me to carry out this work in his newly established group. His, Peter Lodahl's, and Ander Sørensen's inspiration and guidance are highly appreciated.

With the present and past members of the optics group Mikael Østergaard Lassen, Preben Buchhave, Peter Tidemand-Lichtenberg, Metin Sabuncu, Abdul Shakoor, Shailesh Kumar, Miroslav Jezek, Jiri Janousek, Anders Tipsmark, Leonid Krivitsky, Lars Skovsgaard Madsen, Martin Thalbitzer Andersen, Mario A. Usaga, and Emanuele Distante I had many fruitful and stimulating conversations. Alexandra Boltasseva and Abdul Shakoor both supplied many of the samples studied in this work. Jørn Bindslev Hansen deserves many thanks for motivating discussions. Most of the experience with confocal microscopy and NV centers I received during my visit at the University of Stuttgart from Fedor Jelezko and Jörg Wrachtrup. The collaboration with Dirk Witthaut was very fruitful and opened otherwise unachievable opportunities.

I'm very grateful for Stephan Smolka and Metin Sabuncu with whom I had a great time inside and also outside the lab. Invaluable motivation and support came from Elaine Cristina Saraiva Barretto, Martin Schubert, and Kamau Prince.

Professional support by Karin Kyndesen, Dorte Glass, Søren Hjorth, and Anders Poulsen deserves thanks.

I'm very indebted to Елизавета Семенова and my family for cheering me up in sub-optimum situations and the continuous inestimable support.